Progressing Mechanobiology from a Simplified to a More Complex System: Development of Novel Platforms and Investigation of Actin Cytoskeletal Remodeling

by

Kenneth Kwun Yin Ho

A dissertation submitted in partial fulfillment
of the requirements for the degree of
Doctor of Philosophy
(Mechanical Engineering)
in the University of Michigan
2018

Doctoral Committee:

Assistant Professor Allen Liu, Chair
Assistant Professor Brendon Baker
Associate Professor Jianping Fu
Professor Katsuo Kurabayashi

Kenneth Ho

kennetho@umich.edu

ORCID iD: 0000-0001-5587-8302

Acknowledgements

It has been a blessed privilege to work with Allen Liu in his lab!! I am so grateful that he allowed me, coming in with a Mechanical Engineering background, to work on different biological projects. He was so patient with my slow learning progress in the beginning and taught me a lot about how to conduct scientific research. The new ideas that he came up are always mind-blowing. He is probably one of the most influential person for me throughout these five years. I would love to express my deepest gratitude to him for his continuous encouragement, support and advice during my entire PhD study. I would not be the person that I am without him.

I would also like to express my gratitude to my dissertation committee members, Prof. Katsuo Kurabayashi, Prof. Jianping Fu, and Prof. Brendon Baker. I really appreciate the time that they spent, their encouragements, and insightful and critical advice and suggestions. They have been very helpful for me in improving my scientific thinking and reasoning.

I want to thank all the current members and alumni of the Liu lab!! It has been such a good time together throughout these five years. They have made my experience here a lot more special and fun. Special thanks to Dr. Lap Man Lee, for his guidance, advice and mentorship in microfluidic technology. He is truly an engineer to be remembered. Special thanks also to Dr. Luciana Kauer Rosselli, for her patient guidance, advice and mentorship in biology. I especially enjoyed discussing and thinking about science with her. Thanks to

Dr. Tori Murray, Dr. Mingzhi Luo and Mr. Max Denies as well. They were very helpful to answer all my biology questions. It is my pleasure to work with them. I would also never forget the company, friendship and building up with my fellow PhD friends, Dr. Johanna Heureaux, Dr. Xinyu Tan, Dr. Zida Li, and Mr. Jin Woo Lee.

I would also like to thank the University of Michigan for cultivating a great research and learning environment, supporting top research facilities and professional staffs. They have been essential for my PhD study. I want to specially thank the University of Michigan Lurie Nanofabrication Facility and the University of Michigan DNA Sequencing Core for their assistance as well. I also want to thank the Department of Mechanical Engineering, the College of Engineering and the Rackham Graduate School for their supports. I want to thank the Rackham Research Grant, the Rackham Travel Grant and the I.K. McIvor Award for supporting my PhD study.

I want to express my gratitude to my life mentor and my undergraduate advisor, Anderson Shum! Really thank him for giving me different opportunities to conduct research in my undergraduate study. He has been supportive and encouraging both in research and life aspects.

I also want to express my utmost gratitude to my parents for their supports. From them, I experience the most unconditional love that I can experience from any human. They have been very supportive in all aspects and respect my decisions to do what I want to do. All their guidance and love throughout my life are what made me who I am now.

Most importantly, I want to thank Christ Jesus, my Lord and my Savior, for His grace. He not only died for me on the cross so that I am no longer bound to sin but am truly alive in God, but also blesses me with all my experience and all the above people that I met in this five years of time. Researching on living cells, biomolecules and technologies that He creates really opens my eyes in giving thanks to what I am given every day. He also provides me with a spiritual family of lovely brothers and sisters in Ann Arbor Chinese Christian Church (AACCC) so that I can grow with my time here. They will be dearly missed.

Table of Contents

List of Figures

Abstract

Compression is a common mechanical stimulus in our body that results from gravity and tissue growth. Inability for cells to maintain force homeostasis can lead to various diseases, and cells may experience an increase in compressive stress in diseases such as hypertension and cancer. Actin cytoskeleton provides structural and mechanical strength for cells to withstand external mechanical forces. It is also very sensitive to deformation and plays an important role in mechanosensing, due to the tensegrity nature of the cytoskeleton. Despite being an important component, actin remodeling and molecular signaling in response to compression have not been very well studied. From a molecular perspective, the actin network is regulated by actin accessory proteins into different structures and functions. At a cellular level, different actin networks are organized and regulated by various signaling pathways. At an intercellular level, cells are mechanically coupled that enable the transmission of force via actin networks between cells. In this dissertation, I investigated the sensing and transduction of compression stimulus in cells from molecular to intercellular scales, I developed new emerging platforms for the compression studies in *in vitro* reconstitution and single-cell system, and investigated actin remodeling and its related mechanisms under compression in 2D cell population.

First, I developed an approach that combines purified actin cytoskeletal proteins or mammalian cell-free expression and ultra-thin double emulsion template for constructing a simplified model of a cell through *in vitro* reconstitution. This was used to study the

mechanical properties of a specific and isolated cytoskeleton structure. We demonstrated the formation of bundled actin filaments inside the lipid vesicles. By using the mammalian cell-free expression system, we found that actin structures inside the system were precipitating with the droplet stabilizing surfactant polyvinyl alcohol, leading to a compensation of protein production and vesicle stability. Nevertheless, this approach provides a simplified yet insightful cell-like model for future cell mechanics investigation.

I also developed a pneumatic-controlled, two-layered microfluidic platform for applying compression and aspiration to double emulsion droplets as a model cell. I further improved the microfluidic device to apply controlled compression to single cells that can be used to study the heterogeneity of mechanical properties and responses of cells. The device was designed through optimization by simulation and was characterized experimentally. Static and cyclic compressions were applied to single cells seeded inside the device.

Finally, I investigated actin cytoskeletal remodeling, mechanosensing and mechanotransduction of epithelial cells under compression, in a 2D cell population context. I discovered the formation of actin protrusions at the apical surface of the cells under 1200 Pa compression. The actin protrusions were structurally similar to invadopodia but not functionally. Src signaling was found to be an important signaling pathway in these actin protrusions. This discovery opens up new direction of research and may explain why cells become more invasive under compression. This work could also shed light on the heterogeneity of cancer tissues and may inspire a new treatment paradigm.

In this dissertation, I developed experimental platforms and studied the remodeling of actin networks under compression using *in vitro* reconstitution, single-cell and cell population systems, taking advantages of each experimental system. The platforms

developed in this dissertation provide novel techniques for investigating actin cytoskeleton response of cell under compression, and the discovery of actin protrusions reported in this dissertation reveals a new cellular response under high compression.

Chapter 1: Introduction

1.1 Mechanobiology

1.1.1 Biological cell and mechanical force: When the two strangers meet

Mechanobiology is a combination of two words. “Mechano” is a prefix that refers to the involvement of mechanical forces or the use of machines or mechanisms. “Biology” is a field of natural science that studies life and living organisms. The combination of these two words refers to an emerging field at the interface of biology and engineering that investigates how mechanical forces contribute to the responses of living organisms.

Cells are the building blocks of life. A cell provides the basic structural, functional and biological unit of living organisms. It is highly responsive and adaptive to the surroundings and can replicate independently. Cells were discovered by Robert Hooke in 1665 [1] and the theory of cell was later formulated by Theodor Schwann and Matthias Schleiden in 1839 [2]. The understanding of how cells behave, respond and adapt to the environment is still under intense research at this moment.

Force, on the other hand, describes the rule that govern the entire physical world. It is an interaction that when unopposed will change the motion of an object. It was described by Sir Isaac Newton in 1687 [3], and later was known as the Newton’s Laws. The Newton’s second law states that the net force acting upon an object is equal to the rate at which its momentum changes over time. Pressure, defined as the distribution of forces applied over an area of a body, is a stress that if unbalanced can causes deformation in solid materials or flow in fluids.

If we consider cells as a complex material with viscoelastic properties, then there is no doubt that when a force is applied, the cell will undergo partial deformation and partial flow, just like what a partially solid and fluid material will behave. However, cell is more than a complex material. Many early biologists recognized the importance of physical forces and shapes in the development and function of organisms. Later, biologists realized that cellular behaviors do not purely depend on the encoded DNA information inside the cell. The behaviors of cells also depend on the mechanical properties of the extracellular environment and the physical forces that the cell experiences [4].

Indeed, cells interact with the surrounding microenvironment and respond accordingly, including not only chemical stimulation such as hormones, but also physical stimulation such as another neighboring cell or the extracellular matrix. The elasticity and stiffness of the extracellular matrix are critical for normal cell function [5, 6]. The same chemical stimulation will result in different responses when the mechanical properties of the extracellular matrix are altered. The matrix elasticity was shown to be very important for stem cell differentiation [7]. Any deregulation of the extracellular matrix properties could result in diseases like cancer or fibrosis [8, 9]. Apart from the extracellular matrix, other forms of physical stimulation are mechanical forces that act directly on cells, for example solid compressive and tensile stress during muscle contraction or lung expiration and inspiration [10], and fluid shear stress during air breathing and blood flow [11]. Both extracellular matrix properties and forces are crucial in tissue homeostasis and development especially during embryonic development [12, 13]. With the different kinds of physical stimulations that cells sense and respond to, more research has focused on studying how physical forces and change in mechanical properties of cells and tissues contribute to development, cell differentiation, physiology and disease.

1.1.2 Mechanosensing and modes of mechanotransduction: To pull or be pulled

The study of mechanotransduction in cells is an essential focus in mechanobiology. Mechanotransduction converts mechanical stimuli into biochemical signals that alters cellular behaviors. Typically, mechanotransduction involves mechanosensing of the external stimuli by focal adhesions, mechanosensitive ion channels, cell-cell contacts, actin cytoskeleton, or receptors on the plasma membrane. Subsequently, these mechanosensors convert the mechanical stimuli into biochemical signals that change protein-protein interactions and eventually alter gene expression profiles, resulting in different cellular behaviors and functions.

Cells sense different kinds of mechanical stimuli, for example extracellular matrix stiffness, compressive and tensile stress, and shear stress. While we start to understand the cellular responses to different mechanical stimuli, researchers find that cellular responses to different mechanical stimuli appear to be similar at times but different at other times. Some of the mechanotransduction pathways are shared and some are distinct. Recently, a new framework was developed to describe the multiple modes of mechanotransduction and provide a useful starting point for identifying overlaps in molecular players and sensing modalities [14]. Mechanical stimuli can be described as either ‘active’ or ‘passive’, where active input refers to the direct force acting on cells that leads to deformation while passive input refers to physical properties of the environment that the cell pulls against. On the other hand, cellular responses can be described as either ‘material’ or ‘biological’ responses, where material response refers to non-living material response like stress stiffening or viscoelastic creep while biological response refers to behavioral outputs that involve energy consumption or the conversion of mechanical signals into biochemical signals like the assembly of cytoskeleton, signal transduction or gene expression.

1.1.3 in vitro reconstitution, single-cell and cell population mechanobiology study: From simplicity to complexity

Different biological systems can be used for mechanobiology studies such as *in vitro* reconstitution, single cell, cell population, tissue or even animal model. The more simplified the system is, the better we can understand the specific roles and functions of the individual components within a simplified system. In contrast, the more similar the system is to our body, the more physiologically relevant it is, but the biology becomes increasingly complex. Each of these systems has their own advantages and provides unique insight to our understanding.

The cytoskeleton network is compartmentalized and heterogeneous within a cell [15]. The network is also highly dynamic, so that mechanical perturbation could change the cytoskeleton structure and mechanical properties of the cell. One approach to study the mechanical properties of different types of cytoskeleton networks is through *in vitro* reconstitution [16]. Studying *in vitro* reconstituted cytoskeleton networks may yield understanding of the mechanical properties, functions and behaviors of the simplified and isolated network.

For single cell study, individual cell with different actin structures is investigated. Signaling pathway, transcription and translation are also involved in determining the response of the actin cytoskeleton (*e.g.* by expressing a particular actin binding protein) inside the cell. Recently, single cell study is gaining more attention, since it allows us to investigate cell to cell variability. Each cell in a tissue may be different and has heterogeneous mechanical properties [17]. Mechanobiology study of single cells allows one gain insights on the heterogeneous responses of single cells to mechanical signals.

For cell population study, a group of cells is investigated. Since cells interact with their surroundings and pull against them, the microenvironment context that the cells are in becomes the passive mechanical input and affects cellular functions and behaviors. It has been shown that petri dish cell culture cannot recapitulate the functions found in live tissues [18]. Different engineering tools have been developed to manipulate cell populations and investigate their mechanical response [19]. By considering the interactions and force transmission between cells, cell population study of mechanobiology allows the understanding of how intercellular forces affect cellular responses.

in vitro reconstitution, single-cell and cell population methods all have merits for understanding the mechanical responses of cells from different angles. Together, they offer tremendous insights in mechanobiology.

1.1.4 Discovery of mechanotransduction and development of tools: The inseparable unity

To understand how cell transduces the mechanical inputs into material or biological outputs, new engineering tools are necessary to help apply physical forces to cells and alter the mechanical properties of the extracellular matrix. Throughout the history of mechanobiology research, the discovery of mechanotransduction and the development of engineering tools are closely related. New engineering tools developed have enabled many new mechanotransduction discoveries.

After the discovery of focal adhesions and actomyosin contraction [20-23], a new tool was needed to measure the contractile force that a cell pulls on the extracellular matrix. Silicone rubber substrata was developed to visualize the traction force that the cells exert to the substrate [24] and the technique was improved by incorporating fluorescent beads to determine quantitative maps of traction forces [25]. This allows the measurement of traction forces in migrating cells [25] and the tension at cell-cell contacts [26].

As we knew that cells exert traction forces on the extracellular matrix and tension on neighboring cells, new engineering techniques were developed to study whether the change in passive inputs, like the properties of the substrate that cells pull against, would alter the cellular behaviors and functions. By changing the crosslinking properties of acrylamide gels, the stiffness of the extracellular matrix changes. It was found that cell locomotion and focal adhesions are regulated by substrate stiffness [27]. By using an elastomeric stamp of defined features, defined shape and size of extracellular matrix can be created to dictate cell spreading [28]. It was found using this technique that cell shape governs whether individual cells grow or die [29]. A micropillar array technique was developed to manipulate and measure the mechanical interaction between cells and their underlying substrates [30]. This technique allows the modulation of substrate rigidity while keeping other substrate properties constant. It was demonstrated that micropillar rigidity impacts cell morphology, focal adhesion, cytoskeletal contractility and stem cell differentiation [31].

Other than the development of new tools to manipulate passive inputs, researchers developed new tools for the application of active inputs to molecules and cell, such as externally applied forces and displacement, fluid shear, osmotic pressure and acoustic waves. For instance, magnetic tweezer uses magnetic field to apply local forces to magnetic beads bound to a cell [32]. By attaching the magnetic beads to integrin receptors and applying stress to the integrin molecules, it was found that the mechanical signals were transmitted to the cytoskeleton and the cytoskeletal stiffness increased [32]. Recently, magnetic tweezers was used to reveal mechanical plasticity of cells [33]. Atomic force microscopy was developed to manipulate and measure forces and displacements on biomolecules or cells [34, 35]. By measuring the deflection of a cantilever that is in contact with a cell, the displacement or force can be calculated. This technique allows the understanding of domain folding and refolding, and the elastic properties of different proteins [36-38]. Optical tweezer was developed to apply forces to biomolecules by providing attractive or repulsive force to move microscopic dielectric objects [39, 40]. It was used to apply restraining force on cells. As a result, the integrin-cytoskeleton linkages were found to strengthen locally [41]. Microfluidics, a more recent technology that manipulates fluids at the submillimeter scale [42], has provided a suitable platform for studying mechanotransduction. It allows the application of shear stress, interstitial flow, stretching and confinement to the cells [43] and opens numerous opportunities for different mechanotransduction studies [44-46].

Overall, the development of new engineering tools provided platforms for applying passive and active mechanical inputs to cells in a well-controlled manner [47, 48]. This has opened more opportunities for mechanotransduction studies and enables more in-depth understanding of how cells respond to different mechanical stimuli.

1.2 Compression

1.2.1 Active mechanical signal: The physiological pushing

Cells and tissues in our body experience all kinds of chemical and active mechanical signals in physiological and pathological conditions. Due to the complex environment and multiple interactions with neighboring cells, cells experience different combinations of compressive, tensile and shear stresses in different directions. Cells have been isolated from the complex tissue environment and a specific type of stress was applied to the cells to determine how each of these stresses is sensed by the cells and how the specific mechanical signal is transduced inside the cells.

The study of biological responses to compression, tension and shear have a long history, particularly in musculoskeletal [49] and vascular [50, 51] tissue. However, there is a growing interest in studying mechanotransduction from compressive stress in other physiological environments, for example during development [52] and in cancer [53].

1.2.2 Compression in physiological and pathological conditions: When force goes wrong

Compression is a very common type of mechanical signal in our body. Due to our body weight, cells and tissues support our body weight, like bone, experience different extent of compression. Compression and other mode of mechanical loading affect the behavior of bone cells, which in turn may alter the homeostasis of bone [54, 55]. However, when cells and tissues are subjected to sustained compression, it can cause cell deformation, tissue breakdown and inflammation [56]. Pressure ulcers are developed in tissues that are subjected to sustained mechanical loading [57]. Other diseases, such as hypertension, embolism and acute angle-closure glaucoma, are other examples of the development of compression in our body [58, 59]. Compression is also developed in the tumor microenvironment. Due to the confined microenvironment and the uncontrolled division of cancer cells, compression builds up in the tumor and the surrounding normal tissue [60]. Since an increase in compression is common in many different diseases, it is important to study the response and mechanism of cells under compression, so that we can have a holistic understanding of the diseases.

1.2.3 Material response of actin cytoskeleton: Complex elastic solid and viscous fluid property

Material response is the non-living response of the cell, like stress stiffening and viscoelastic creep. Under compressive load, any solid elastic material will deform. The ratio between the applied compressive stress and the deformed strain is the elastic modulus of the solid material. For a Newtonian fluid, compression results in constant deformation. The ratio between the applied compressive stress and the deformation rate is the viscosity of the fluid. Cell has a mechanical property that is in between that of an elastic solid and a pure Newtonian fluid, and thus is viscoelastic. The viscoelasticity of a cell is mainly due to the properties of actin cytoskeleton. Actin cytoskeleton is a network of actin filaments and crosslinking proteins that provides structure and mechanical strength of a cell. Through spatiotemporal coordination with a variety of actin binding proteins, actin assembly drives movement of a cell. Due to the complex structure of the actin cytoskeleton, the mechanical properties and material behavior of the actin networks are still under intense research in order to fully understand how cells regulate cell shape and generate mechanical forces [61].

The viscous effect of the actin network is due to the dynamic and finite binding affinity of crosslinker to actin filaments [62-64]. The easier or more frequent the crosslinkers dissociate from the actin filaments, the more viscous the actin network will be. The time scale at which the mechanical stress is applied to the cell will determine whether the elastic or viscous effects dominate. For short loading time scale, the crosslinkers remain bound to the actin filaments and therefore, elastic effect dominates. On the contrary, for long loading time scale, the unbinding and rearrangement of crosslinkers can lead to stress relaxation and the accommodation of cell shape change, and therefore displaying a viscous effect [33]. Apart from the time scale at which the mechanical loading was applied, the mechanical response of the actin cytoskeleton network will become nonlinear at large stress or strain. Therefore, the stiffness of the actin network depends on the magnitude of the applied stress or strain. In general, low actin density network will soften at large strain, while high actin density network will stiffen at intermediate strains and dramatically soften at larger strains [65-67].

The above studies were mostly carried out in a reconstituted environment without confinement. Therefore, they may not reflect the response of cells, in which actin cytoskeleton is confined inside the plasma membrane. However, similarly, the material response of cells under compression will be determined by the stress and strain level, the time scale at which compression was applied, and the dissociation property of crosslinkers in the actin cytoskeleton. The study of how actin cytoskeleton responds to mechanical compression can provide insight into how cells withstand mechanical compression and how they regulate their shape under compressive loading.

1.2.4 Biological response of actin cytoskeleton: To overcome the force

The actin network inside living cells are not at equilibrium [68]. It constantly changes due to the biological signals that control the assembly, architecture and mechanical properties of actin networks in different parts of the cells through the regulation of cross-linking protein affinity, activity of myosin-II and actin filament assembly [61]. For example, the stiffness of an actin network can be altered by myosin activity, through phosphorylation of its regulatory light chain [69, 70]. These biological signals can be a response to mechanical stimulations, so that the assembly, architecture and mechanical properties of actin networks change in response to mechanical deformation. Cyclic stretching can lead to the reinforcement and fluidization of actin cytoskeleton [71]. It was later found that the reinforcement of actin networks under cyclic stretching was due to the phosphorylation of a small heat shock protein HspB1 through a p38 MAPK-dependent pathway [72]. Fluid shear stress also changes cell shape and alignment through actin network remodeling in the direction of flow [73]. Apart from cyclic stretching and fluid shear stress, cyclic compression of human mesenchymal stem cells embedded in collagen also leads to the change in assembly and architecture of the actin networks [74]. Mechanoresponsive, omni-directional and local matrix-degrading actin protrusions were formed at the membrane of human mesenchymal stem cells under cyclic compression. The actin protrusions were found to be similar to filopodia and invadopodia in morphology and composition, but different in stability, abundance, signaling and function. Altogether, these studies showed that actin cytoskeleton plays an important role in eliciting biological signaling when mechanical forces were exerted.

1.3 Emerging experimental platforms for studying mechanobiology of compression

1.3.1 Membrane-confined bottom-up reconstitution: A simplified yet insightful approach for mechanobiology

The structure of a cell is complicated, and there are a lot of biological pathways involved inside cells that change the ways cells respond constantly. When we measure the mechanical properties of the cell, a measurable force is applied to the cell and the deformation of the cell is observed under the applied force. However, cell is a living entity that responds to the force that it experiences. It is difficult to uncouple the material response and the biological response of a cell under a mechanical loading. Therefore, *in vitro* reconstitution has been used as a platform for understanding how different cytoskeletal structures respond to forces separately [16]. For example, actin networks have been reconstituted and an atomic force microscope has been used to apply a force and measure the network deformation. It was found that the growth velocity of an actin network depends on the force that was applied to the network while it was growing [75]. The structure and mechanical properties of the actin network also changed with the mechanical loading [76]. However, the networks were reconstituted in a biochemically opened environment that failed to capture the compartmentalized nature of cellular actin networks.

Membrane-confined bottom-up reconstitution is an engineering approach to encapsulate reconstituted cellular structures inside lipid vesicles. The reconstituted cellular structures are confined inside a lipid membrane, in which biophysical and biochemical conditions will be different from bulk structures. For example, there will be limited nutrients for the biological activity. Diffusion is confined within the lipid vesicle. Interactions can also be engineered between the cellular structure and the lipid membrane to reconstitute interactions inside living cells. Besides, with the advancement of cell-free expression systems, encapsulation of cell-free expression system within lipid vesicles allow the construction of cell-like model that recapitulate the structure, mechanical properties and potentially the response of living cells under mechanical loading. Membrane-confined bottom-up reconstitution is a simplified yet insightful approach for studying the mechanics of cell.

1.3.2 Microfluidics: Promising microtechnology for the study of mechanobiology

The development of novel microtechnology techniques and tools had been essential for the study of mechanobiology. For example, the use of elastic silicone surfaces as a substrate for cell spreading [24] and the further development into traction force microscopy [25] revealed that cells produce force to the substrates that they attach to. Additional tools were introduced for the application of active forces to cells. The development of atomic force microscopy [36], optical trap [41] and magnetic tweezers [77] have provided detailed understanding of mechanosensing at the molecular level. While the above novel microtechnology techniques apply active forces to cells through specific proteins or lipids, recently, different studies used modified atomic force microscopy probes for the application of compressive forces to single cell [78, 79]. While atomic force microscopy is a powerful approach to apply compressive forces and measure deformation of cells, the method has a low throughput and requires specialized skills.

Microfluidics is a promising microtechnology that utilizes microchannels with dimensions of tens of micrometers to manipulate small amounts of fluid [80]. It allows the use of small sample and reagent quantities, relatively lower cost and higher throughput. A small channel also enables small Reynolds number laminar flow, which is more controllable. The material used for building microfluidic devices (i.e. PDMS) is also biocompatible, making microfluidics a good platform for biological studies [42].

Microfluidics has been used for the study of mechanobiology [43] by providing a means to apply shear stress, interstitial flow, stretching and confinement to the cells [44-46]. For compression of cells, the development of switching valves in microfluidic devices [81] led to several high throughput platforms to study lysis of cells [82], injury of axons [83] and growth of *E. coli* [84] under compression. However, the microvalves microfluidic platform has not been developed for the application of compression to single cells, which could provide a more precise understanding of the heterogeneous responses of each cell under compression.

1.4 Dissertation outline

Mechanical compression is a common and important type of mechanical signal in our body. However, unlike fluid shear stress and stretching, the material responses and molecular responses of cells under compression are still not very well understood. This is in part due to the fact that the experimental platform for studying mechanotransduction of compression in single cells is still underdeveloped. From past history, we know that both the discovery in mechanotransduction and development of engineering tools come hand-in-hand. Moreover, the study of mechanobiology in *in vitro* reconstitution, single cell and cell population each uniquely contributes to our understanding of mechanobiology and as a whole bridge together to form a more complete picture. Considering these aspects, the goal of this dissertation is to further study the actin cytoskeleton response of cell under compression through the development of emerging platforms. I will first develop tools and study the mechanotransduction of compression in *in vitro* reconstitution system, and then from there I will move to single-cell and cell monolayer systems. Each of these systems provide insights into the effect of compression on actin network alone, in a single cell and in a cell monolayer.

Specifically, I will first demonstrate a membrane-confined bottom-up reconstitution platform for constructing a simplified model of a cell in Chapter 2. The simplified model of a cell has a lipid membrane encapsulating actin networks or cell-free expression system for cell mechanics study. In Chapter 3, I will develop a valve-based microfluidic platform for applying mechanical forces to a simplified model of a cell and mechanically activating it. Chapter 4 will describe my effort to improve the microfluidic compression device for single-cell compression study. The device offers the potential for studying the heterogeneity of single-cell mechanics. In Chapter 5, I will describe my discovery of actin protrusions under static compression in a cell monolayer system. The compression of cell monolayer provides us insight into the responses of a population of cells that experience normal compression. Finally, Chapter 6 will summarize the contributions of this dissertation and suggest potential future research directions.

Chapter 2: Constructing a simplified model of a cell for cell mechanics study

** Part of this chapter has been published in Ho et al., Methods in Cell Biology, 2015 and Ho et al., PLoS One, 2017.*

2.1 Introduction

2.1.1 Bottom-up reconstitution

Biological processes can be studied in the context of a whole cell or in biochemical reconstitution *in vitro*. Both methodologies have advantages and disadvantages. By using whole cells, the biological process can be studied and understood in a physiologically relevant context. Often, this involves genetic manipulation or drug perturbation to the cells and monitoring cellular responses. Even without manipulation, the inherent complexity of intracellular subsystems and signaling pathways gives rise to possible unknown factors influencing the components under study as proteins rarely play a single role in a single process.

To simplify the study of intracellular events, researchers have been able to reconstitute many major subcellular functions *in vitro* through a bottom-up approach, and this has led to deeper understanding of many processes. However, *in vitro* reconstitution of spatially organized processes has been more challenging as many of these processes are membrane-based and require an enclosed environment. Bottom-up reconstitution of protein encapsulated lipid bilayer vesicles provide an enclosed, defined environment and a robust platform to study desired biological functions and properties. Lipid bilayer vesicles encapsulating reconstituted proteins are similar to cells that are also enclosed by a lipid membrane.

2.1.2 Simplified model of a cell for cell mechanics study

To advance our understanding in cell mechanics, different cellular components have been reconstituted separately *in vitro* using a bottom-up approach for deeper understanding of their mechanical properties [85-87]. Among them, the study of the material properties of actin networks and their responses under force benefited from a bottom-up approach. Actin cytoskeleton is a network of actin filaments organized by actin-binding proteins. It was found that with different cross-linking or bundling actin-binding proteins, the actin networks formed had different elastic behaviors [65, 88, 89]. With the help of atomic force microscopy, the force loading history plays an important role in the material properties of the actin networks [75, 76, 90]. While the reconstitution of different actin networks provides a controllable platform for the study of actin network mechanics, such as those that employed with atomic force microscopy, the networks are in a biochemically opened environment that fails to capture the compartmentalized nature of cellular actin networks.

Cell-free expression (CFE) system is a biomolecular *in vitro* transcription and translation system using translation machinery extracted from cells. It holds tremendous promise as the cytosol of artificial cells. Development of CFE has been driven by a growing demand for an efficient and simple protein production method [91]. As a cell-free system where cell viability and survival does not need to be considered, CFE only produces protein(s) of interest. With the advances made in cell-free protein expression over the years [91], several groups have been able to encapsulate a bacterial CFE system inside liposomes and demonstrated expression of proteins within the liposome [92-95]. As the development of CFE matures and its use becomes more widespread, there is more interest in the use of mammalian CFE. For the production of proteins of eukaryotic origins with proper post-translational modifications, mammalian CFE is more advantageous over bacterial CFE. HeLa cell-derived in vitro coupled transcription/translation system with supplemented transcription and translation factors has been developed [96, 97]. The mammalian CFE system offers a more powerful system to synthesize more complex proteins, such as mechanosensitive membrane proteins.

Toward reconstituting an artificial cell that is comparable to the membrane-bound and compartmentalized properties of a cell, I propose the construction of a simplified model of cell, which can also be used for cell mechanics study. The simplified model of cell is comprised of a lipid bilayer membrane, providing an enclosed and defined environment and encapsulating a complex protein solution (**Figure 2-1**). The goal of this chapter is to develop and construct a simplified model of a cell that could be used for cell mechanics

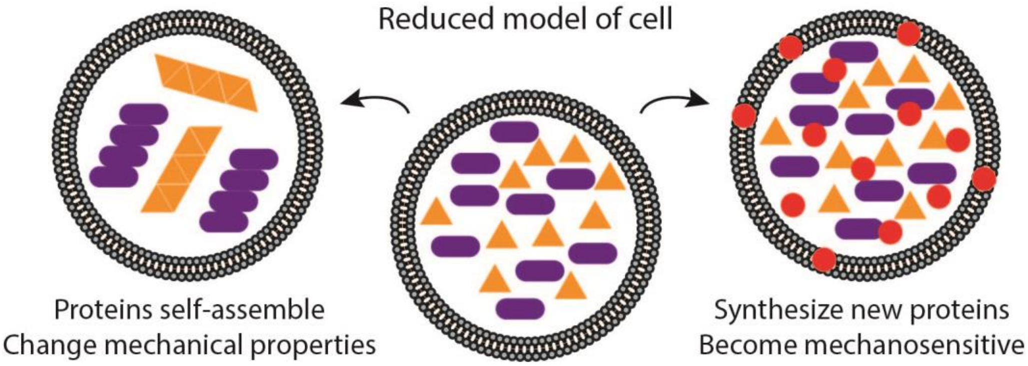

Figure 2-1: Schematic of a simplified model of a cell
(Left) Proteins self-assemble inside the simplified model of a cell to form a network of proteins. This changes the overall mechanical properties. (Right) New proteins (e.g. mechanosensitive channels) are synthesized inside the simplified model of a cell, to confer mechanosensitive functions.

study. I will first describe the development of double emulsion template for the generation of lipid vesicles. Then, I will describe the encapsulation of actin networks and mammalian CFE system inside the double emulsion templated lipid vesicles.

2.2 Materials and methods

2.2.1 Ultra-thin double emulsion templated lipid vesicles

Ultra-thin aqueous-in-oil-in-aqueous double emulsions were used as a template for the formation of lipid vesicles. The middle oil phase consists of a volatile oil separating the inner encapsulated aqueous phase and the outer aqueous phase. Phospholipids dissolved in the middle oil phase tend to self-assemble and form monolayers on the aqueous-oil and oil-aqueous interfaces, which stabilize the emulsions. When oil begins to evaporate, it will de-wet the lipid interface. A vesicle will form when all the oil evaporates (**Figure 2-2**). Ultra-thin oil phase was used to reduce the oil evaporation time. The evaporation of middle oil phase cannot be too fast because the double emulsions could burst and this would reduce the yield. The double emulsions were kept in a closed environment with slow evaporation to form lipid vesicles.

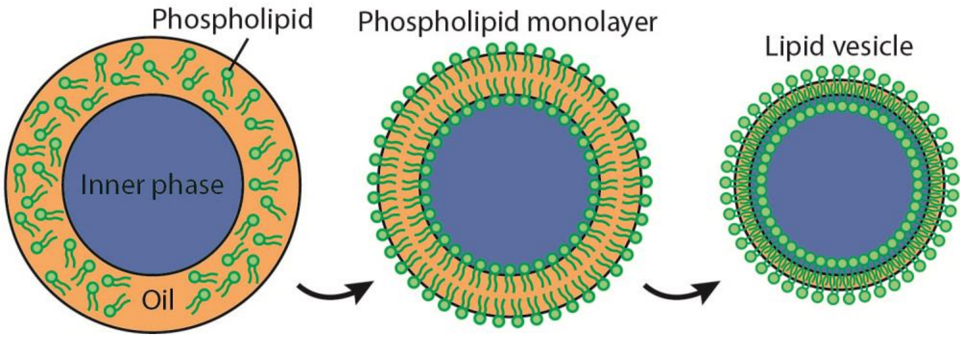

Figure 2-2: Schematic of double emulsion templated lipid vesicle formation. The evaporation of volatile oil drives the formation of lipid vesicles from double emulsions.

2.2.1.1 Fabrication of ultra-thin double emulsion device

Double emulsions can be generated in a glass microcapillary device [98]. The glass microcapillary device was modified so that double emulsions with ultra-thin shell can be generated [99]. The schematic of the ultra-thin double emulsion device is shown in **Figure 2-3A**.

The device was fabricated by assembling tapered round capillary, square capillary and syringe needles together using 5 minutes epoxy [99, 100]. First, a round capillary (Sutter Instrument B100-58-10) was pulled using a pipette puller (Sutter Instruments P-87) into a tapered shape. The inner diameter of two tapered capillaries were modified using 1200 grade sandpaper to obtain inner diameters of 50 and 80 μm for the injection tube and collection tube respectively. The inside surface of the injection tube was treated with trichloro(1H,1H,2H,2H-perfluorooctyl)silane to render the surface hydrophobic. Then, the injection tube and collection tube were inserted into a square capillary (AIT, 810-9917) placed on a glass slide and were aligned using an optical microscope. Another round capillary was pulled above a fire flame to form two long and thin pipettes to obtain an outer diameter of around 200 μm. One pulled pipette was inserted into the back of the injection tube and aligned using the optical microscope. Syringe needles (McMaster Carr, 75165A677) were cut and glued to the glass slide using 5 minutes epoxy (Devcon, 14250). At last, microtubings (Scientific Commodities, BB31695-PE/5) were connected to the syringe needles. The step-by-step instructions for building the microfluidic device is shown in **Figure 2-3B**. The tapered capillaries have to be coaxially aligned inside the square capillary, and the inner surface of the injection tube has to be treated such that it is

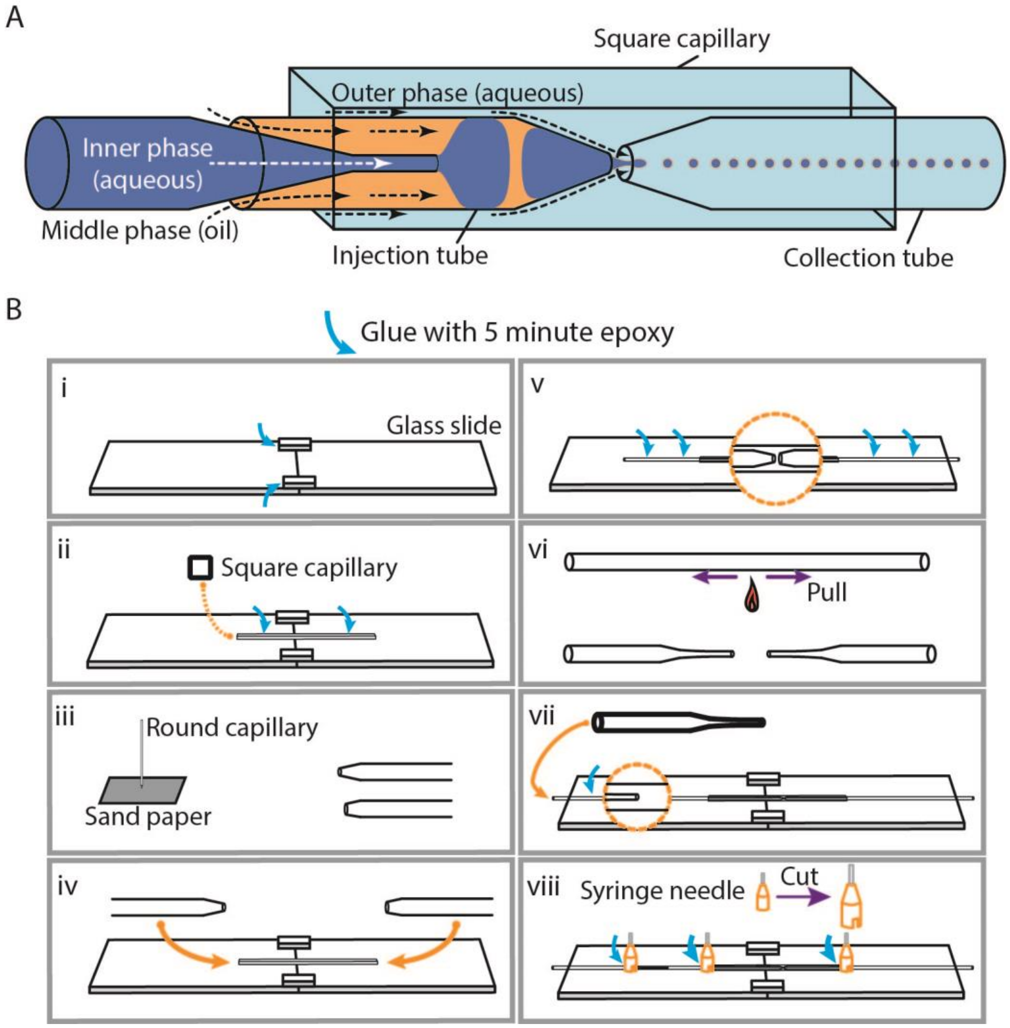

Figure 2-3: Schematic and fabrication of glass capillary microfluidic device. (A) Schematic of ultra-thin double emulsion device. (B) Step-by-step instructions on building double emulsion device. (i, ii) Square glass capillary is glued to the device platform made of two glass slides. (iii) Two tapered round capillaries are sanded to modify the diameter of the openings. (iv, v) The two round capillaries are inserted inside the square capillary and glued to the glass slide. (vi, vii) Another round capillary is pulled under frame and inserted into one of the round capillary. (viii) Syringe needles are cut and glued onto the device and serve as the inlets of the device.

sufficiently hydrophobic to prevent wetting of the capillaries by the aqueous phase and disturbing the fluid flow. A well fabricated double emulsion device can be used to generate ultra-thin double emulsions for over two months.

2.2.1.2 Formation of ultra-thin double emulsions

Three syringe pumps (New Era Pump Systems, NE-500) were used to pump inner, middle and outer solutions into the glass capillary droplet microfluidic device for the formation of double emulsions (**Figure 2-4A**). When the flow was adjusted correctly, the fluid will break and form aqueous-in-oil-in-aqueous double emulsions in the dripping regime [101, 102]. Ultra-thin double emulsion generation was imaged using a high-speed camera (Phantom Miro eX2) at 3000 fps on an Olympus inverted microscope. The optimal flow rates of the inner, middle and outer solutions for successful formation of aqueous-in-oil-in-aqueous double emulsions depend on various factors, including the glass capillary geometry, viscosities and densities of the three solutions. Typical initial flow rates of 200 μL/h, 200 μL/h and 2400 μL/h were used for the inner, middle and outer phases respectively, while the flow rates were adjusted based on the emulsions formed. Ultra-thin double emulsions were formed successfully as shown in **Figure 2-4B**.

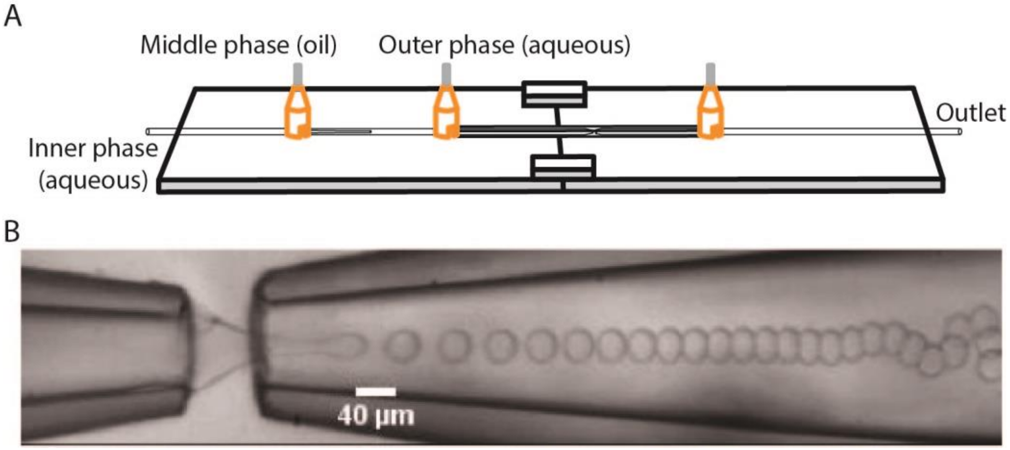

Figure 2-4: Schematic for the formation of ultra-thin double emulsions.
(A) The microtubings connect the three syringes containing inner, middle and outer phases are to the glass capillary and syringe needles in the way shown. (B) Image of ultra-thin double emulsion formation using the glass capillary microfluidic device.

2.2.2 Encapsulation of reconstituted actin networks in double emulsion templated vesicles

Actin filaments can organize into different actin networks by binding and copolymerizing with different actin-binding proteins. For example, to form branched actin networks or parallel actin bundles, actin monomers are copolymerized with Arp2/3 complex, nucleation promotion factor and capping proteins, or α-actinin and fascin respectively in the presence of ATP. The polymerization of actin filaments occurs within minutes and the polymerized actin filament network would alter the formation of double emulsions inside the microfluidic device. Therefore, a glass capillary microfluidic device that allows two different solutions to be mixed together just before being encapsulated inside the double emulsions was designed (**Figure 2-5A**). The two different solutions composed of the reaction components, including actin monomers, actin-binding proteins and polymerization buffer, where the actin monomers are separated from the actin-binding proteins and polymerizing buffer. The concentration of different regulatory proteins and actin monomers can be changed easily by changing the inner phase solution, and this provides us a platform to form different actin networks inside the vesicles (**Figure 2-5B**).

The inner solution consisted of actin solution and polymerizing buffer solution. The actin solution was composed of 4 μM Rhodamine-labelled actin, 1X G-buffer, 2% polyvinyl alcohol (PVA), 8% polyethylene glycol (PEG), 15 mM creatine phosphate, 125 nM fascin and 138 μM sucrose. The polymerizing buffer solution was composed of 1X G-buffer, 2X F-buffer, 2% PVA, 8% PEG and 182 μM sucrose. The middle phase was a mixture of chloroform/hexane at a ratio of 36:64 (vol/vol). 7 mM of lipids with compositions of 65.8% DOPC, 30% cholesterol, 0.2% 16:0 Liss Rhod PE or 34.8% DOPC, 34.7% DPPC, 30% cholesterol, 0.5% 16:0 NBD-PE and 4% PEG2000 were dissolved in the solvents. The outer

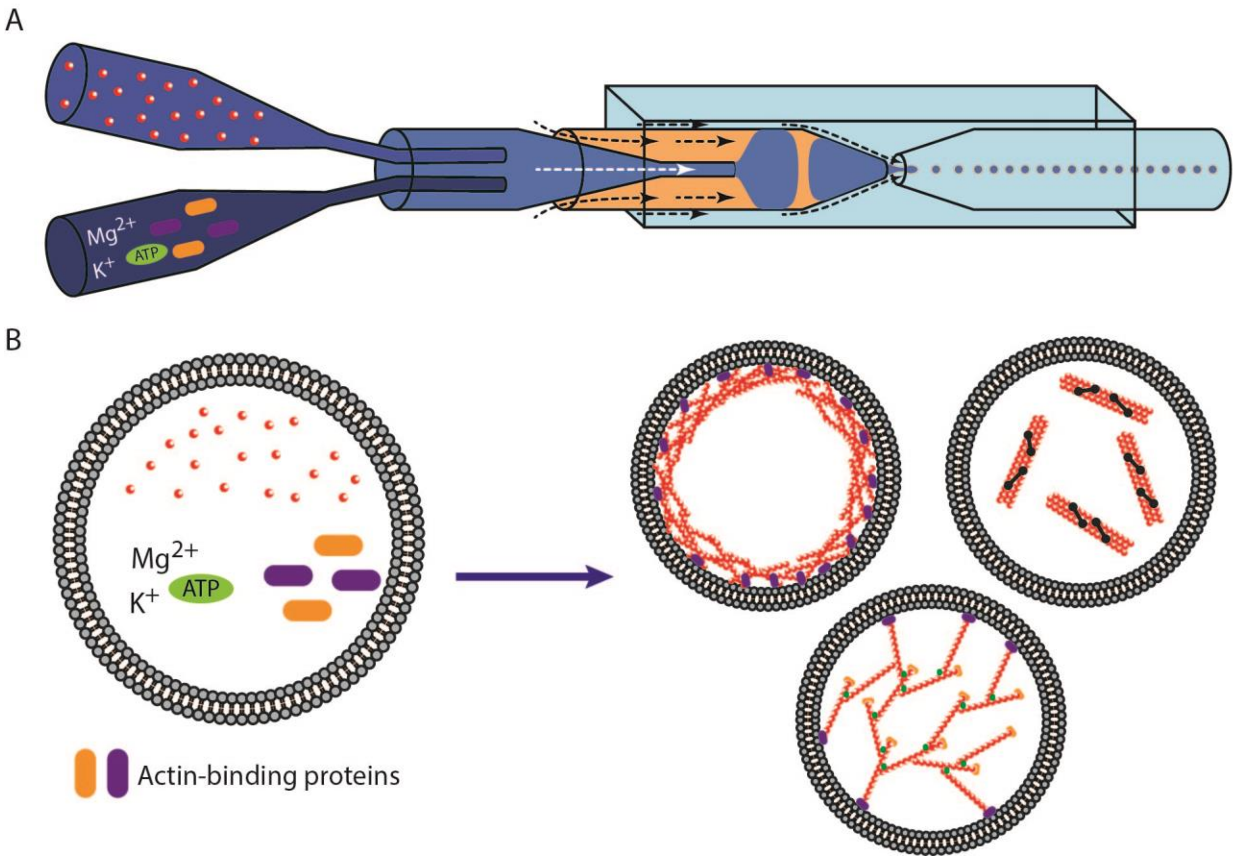

Figure 2-5: Schematic for the encapsulation of reconstituted actin networks in double emulsion templated vesicles.
(A) Modified glass capillary microfluidic device that allows the mixing of two components just before being encapsulated inside the double emulsions for the formation of lipid vesicles. (B) With different actin-binding proteins copolymerized with actin monomers, actin cortex, actin bundles or branched actin network can be formed.

solution composed of 10% PVA with 300 mM of glucose. The osmolarities of the inner and outer solutions were measured by using 5600 Vapro Vapor Pressure Osmometer (ELITechGroup) and were balanced. Flow rates of 150 µL/h, 150 µL/h, 400 µL/h and 2600 µL/h were used for the actin solution, polymerizing buffer solution, middle and outer phases respectively.

2.2.3 Encapsulation of mammalian cell free expression system in double emulsion templated vesicles

The mammalian cell-free expression system is a mixture of six different solutions (**Figure 2-6**), each described below. HeLa lysate was prepared according to previously published procedures [100]. DNA constructs encoding GADD34 and T7 RNA polymerase were obtained from H. Imataka (University of Hyogo, Japan) and purified following previously established protocols [96, 97]. Mix 1 has a composition of 27.6 mM Mg(OAc)2 and 168 mM K-Hepes (pH 7.5). Mix 2 has a composition of 12.5 mM ATP, 8.36 mM GTP, 8.36 mM CTP, 8.36 mM UTP, 200 mM creatine phosphate, 7.8 mM K-Hepes (pH 7.5), 0.6 mg/mL creatine kinase, 0.3 mM amino acid mixture, 5 mM spermidine and 44.4 mM DTT. MscL-eGFP was cloned into pT7CFE vector (ThermoFisher). Mammalian CFE reactions were prepared by first mixing 9 µL lysate, 2.25 µL Mix 1 and 2.7 µL GADD34 (to give a final concentration of 310 nM) and incubated at 32oC for 10 min. Then, 2.25 µL Mix 2, 1.8 µL T7 RNA polymerase (to give a final concentration of 450 nM) and 1.5 µL DNA (500 ng) were added to form the complete CFE reaction and incubated at 32oC for 5 hr. Larger total

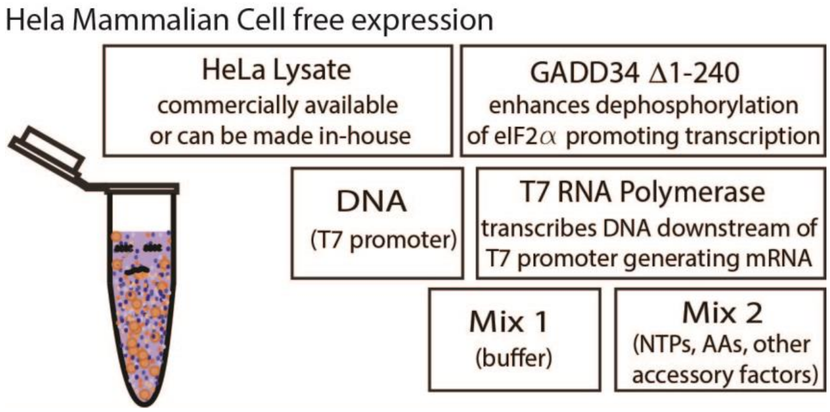

Figure 2-6: Schematic of mammalian cell-free expression system
HeLa mammalian CFE system is a combination of HeLa lysate, Mix 1 buffer, GADD34, T7 RNA polymerase, Mix 2 accessory factors and DNA plasmid containing T7 promoter.

volume was also used for the encapsulation in lipid vesicles while all the volume ratios remained the same.

The inner solution consisted of the mammalian CFE with 2% surfactant (PVA or Pluronic surfactant) and 2 mM of fluorinated surfactant F6-TAC. The middle phase was a mixture of chloroform/toluene or chloroform/hexane at a ratio of 36:64 or 40:60 (vol/vol). Lipid compositions of 69.5% DOPC, 30% cholesterol and 0.5% 16:0 Liss Rhod PE or 34.8% DOPC, 34.7% DPPC, 30% cholesterol and 0.5% 16:0 Liss Rhod PE were dissolved in the solvents. The outer solution composed of 10% PVA with 20 mM K-Hepes (pH 7.5), 150 mM KCl and glucose. The osmolarities of the inner and outer solutions were measured by using 5600 Vapro Vapor Pressure Osmometer (ELITechGroup) and were balanced. Flow rates of 200 µL/h, 200 µL/h and 2400 µL/h were used for the inner, middle and outer phases respectively.

2.2.4 Microscopy and imaging

Brightfield or fluorescence images were obtained on a Nikon inverted microscope (TiE) or on an Olympus spinning disk confocal microscope (IX73 with Yokogawa CSU X1).

2.2.5 Protein identification by LC-tandem mass spectrometry

HeLa CFE were incubated at 32^{o}C for 5 hours with different PVA concentrations. The samples were then centrifuged at 16,100 g for 10 minutes at 32^{o}C to separate the supernatant and the pellet. The supernatant was mixed with 4x SDS sample buffer while the pellet was mixed with 1X SDS sample buffer (same final SDS concentration) and both samples were denatured for 5 min at 95^{o}C. Samples were run on SDS-PAGE and stained with SimplyBlue SafeStain (Thermo Fisher Scientific). The protein bands of interest were excised and submitted to the Proteomics Resource Facility at the University of Michigan for protein identification using LC-MS based approach according to established protocol. Briefly, gel slices were destained with 30% methanol for 4 h. Upon reduction (10 mM DTT) and alklylation (65 mM 2-chloroacetamide) of the cysteines, proteins were digested overnight with 250 ng of sequencing grade, modified trypsin (Promega). Resulting peptides were resolved on a nano-capillary reverse phase column (Acclaim PepMap C18, 2 micron, 50 cm, ThermoScientific) using 0.1% formic acid/acetonitrile gradient at 300 nl/min (2-30% acetonitrile in 60 min followed by a 90% acetonitrile wash for 5 min and a further 25 min re-equilibration with 2% acetonitrile) and directly introduced in to Q Exactive HF mass spectrometer (Thermo Scientific, San Jose CA). MS1 scans were acquired at 120K resolution. Data-dependent high-energy C-trap dissociation MS/MS spectra were acquired with top speed option (3 sec) following each MS1 scan (relative CE ~28%). Proteins were identified by searching the data against Homo sapiens database (UniProtKB) using Proteome Discoverer (v2.1, Thermo Scientific). Search parameters included MS1 mass tolerance of 10 ppm and fragment tolerance of 0.1 Da; two missed cleavages were allowed; carbamidimethylation of cysteine was considered fixed modification and oxidation of methionine, deamidation of asparagine and glutamine were considered as potential modifications. False discovery rate (FDR) was determined using target-decoy strategy and proteins/peptides with a FDR of ≤1% were retained.

2.2.6 Protein identification by Western blot

Sample preparation for Western blot was identical as described in the previous section. Samples were separated by SDS-PAGE and transferred to a nitrocellulose membrane. The membrane was washed, blocked by 5% milk, and probed using anti-actin antibody (Santa Cruz Biotechnology sc-8432). Three independent experiments were performed to confirm the obtained result. Intensity of gel bands was quantified using Image Studio Lite software.

2.3 Results and discussion

2.3.1 Generation of unilamellar lipid vesicles

Double emulsion templated lipid vesicles were generated using the ultra-thin double emulsion device and were tested with their unilamellarity. A membrane-damaging protein toxin from streptococci, streptolysin O (SLO) can only insert into a unilamellar lipid bilayer. If the double emulsion templated lipid vesicles were unilamellar, the amount of fluorescence dye influx will be different when streptolysin-O was added to the lipid vesicles (**Figure 2-7A**) [103]. In a dye influx assay, as expected, the normalized fluorescence intensity inside the lipid vesicle compared to the outside was significantly higher when 0.05 mg/ml streptolysin-O was introduced (**Figure 2-7B**), demonstrating the unilamellarity of the lipid vesicles generated using the double emulsion template method.

The generation of unilamellar lipid vesicles with the capability of encapsulating proteins provides an important platform for constructing a simplified model of a cell for cell mechanics study. The properties of lipid membrane depend on the lipid compositions and unilamellarity of the membrane, which have been shown to affect cell stiffness. For

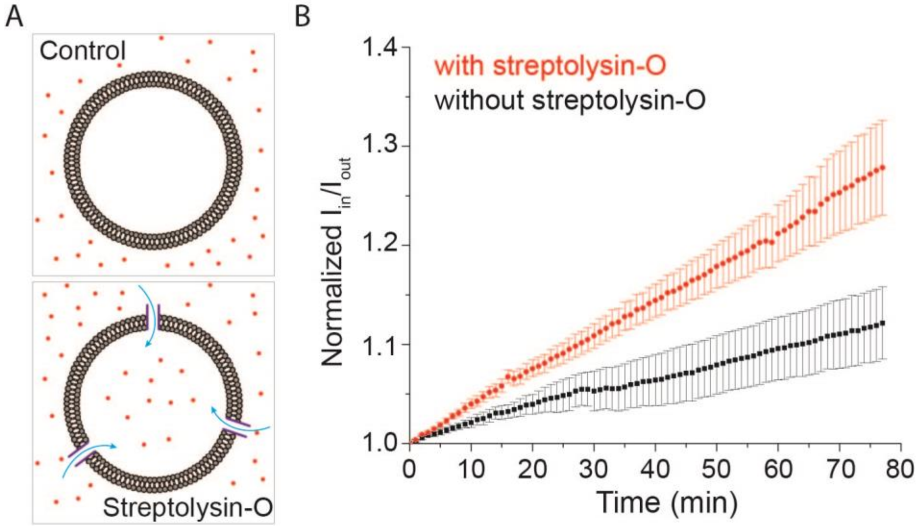

Figure 2-7: Permeability test shows the unilamellarity of the lipid vesicles Permeability test of double emulsion templated vesicles containing 69.5% DOPC, 30% cholesterol, and 0.5% NBD-PE formed from 36/64 chloroform/hexane in the middle phase. 0.05 mg/ml of SLO was incubated with the vesicles for 1 hr at room temperature before TMR-rhodamine was added to a final concentration of ~0.12 mM. $p < 0.05$ using unpaired t test.

example, cholesterol depletion was shown to increase membrane stiffness of endothelial cells [104]. Furthermore, a lipid bilayer membrane allows the insertion of membrane proteins, which provides a platform to study mechanosensitive membrane channels. The ultra-thin double emulsion template method provides a strong foundation for further synthesizing a model of cell for cell mechanics study.

2.3.2 Encapsulation of actin networks inside lipid vesicles

Intracellular actin cytoskeleton is one of the major components in a cell that contributes to cell stiffness and mechanical properties [86]. In our simplified model of a cell, actin cytoskeletal components were encapsulated inside the double emulsion templated lipid vesicles. Actin bundles increase the bending rigidity of the actin filaments, and affect the elastic behaviors and deformability of the cells [65].

When fascin was added to the actin filaments, fascin binds and forms actin bundles (**Figure 2-8A**) [105]. This was shown experimentally in bulk solution before encapsulation inside the lipid vesicle (**Figure 2-8B, C**). When the actin monomers, fascin and actin polymerizing buffer were encapsulated inside the double emulsion templated lipid vesicles as described in Section 2.2.2 , actin bundles self-assembled inside the lipid vesicles (**Figure 2-8D**).

The intracellular actin cytoskeleton is more complicated than the actin bundles formed inside the lipid vesicles above. Different types of actin networks serve different purposes in living cells and are spatially regulated. Actin networks attach to the plasma membrane which together contribute to the stiffness of the cell. The encapsulation of actin

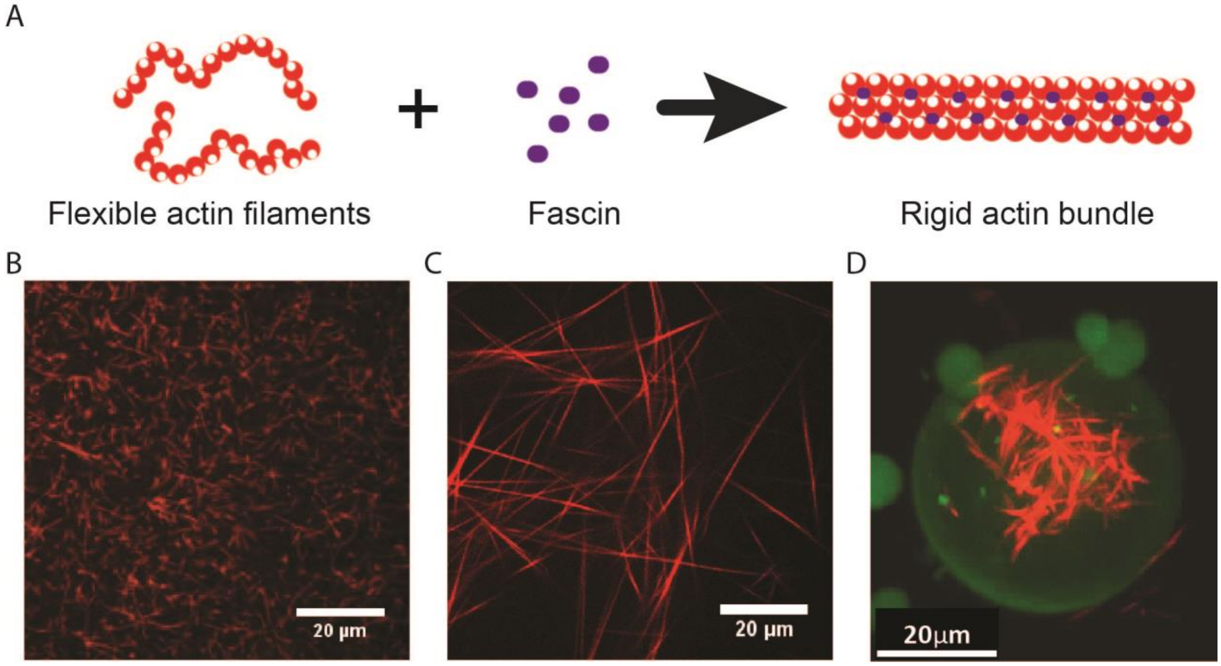

Figure 2-8: Encapsulation of actin bundles in lipid vesicles
(A) Schematic showing the formation of actin bundles by adding fascin to flexible actin filaments. (B) Actin filaments were polymerized in bulk solution. (C) Actin filaments and fascin were co-polymerized in bulk solution. (D) Actin and fascin were encapsulated inside a lipid vesicle using double emulsion template. Red color indicates the actin and green color indicates the lipid membrane.

bundles inside lipid vesicles is among one of the first few attempts to form actin networks inside lipid vesicles [106-110]. This represents a step towards building a simplified model of a cell for cell mechanics study.

2.3.3 Encapsulation of mammalian cell-free expression system inside lipid vesicles

2.3.3.1 Aggregate formed in cell-free expression encapsulated vesicles

Besides directly reconstituting cytoskeleton networks in vesicles using biochemically purified proteins, we also investigated the use of cell-free expression (CFE) for producing proteins of interest *in situ*. The goal of developing mammalian CFE is to express a variety of proteins (including membrane proteins) in a simplified cell model. Since HeLa cell lysate is a highly complex and highly concentrated solution, it is essential to define experimental conditions within a vast parameter space where mammalian CFE is compatible with microfluidic double emulsion generation. As a starting point, using

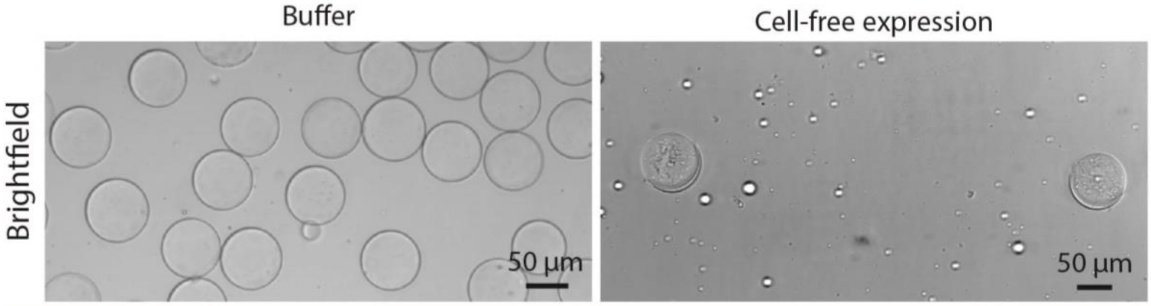

Figure 2-9: Aggregate formed in cell-free expression encapsulated vesicles
(Left) Buffer solution (20 mM HEPES pH 7.5, 400 mM sucrose, 2% PVA, 8% PEG) was encapsulated as the inner phase using capillary droplet microfluidics with DOPC/cholesterol dissolved in chloroform/hexane as the middle phase. (Right) HeLa CFE (18 µl HeLa lysate, 4.5 µl Mix 1 buffer, 5.4 µl GADD34, 4.5 µl T7 RNA polymerase, 3.6 µl Mix 2 accessory factors and 3 µl MscL DNA plasmid containing T7 promoter) with 2% PVA was encapsulated with DOPC/cholesterol dissolved in chloroform/hexane as the middle phase and incubated at 32 degrees in a closed environment.

capillary droplet microfluidics, I first produced double emulsion templated vesicles at a high yield encapsulating 2% PVA surfactant solution (**Figure 2-9, left**). Recognizing that CFE of membrane proteins can be more facile and efficient than conventional biochemical purification [111, 112], I use mechanosensitive channel of large conductance (MscL) as a test case for membrane protein incorporation in double emulsion templated vesicles. Interestingly, I observed large aggregation inside double emulsion templated vesicles that were visible under brightfield microscopy when mammalian CFE was encapsulated (**Figure 2-9, right**).

2.3.3.2 Aggregate formation was not due to insoluble membrane protein or organic solvent

I first suspected that MscL was aggregating since membrane proteins usually require detergent at a concentration above critical micelle concentration (CMC) to be solubilized in an aqueous solution. During biochemical purification of MscL, a nonionic detergent Triton X-100 is typically used to solubilize MscL. Using a centrifugation assay (**Figure 2-10A**), I found that MscL produced by CFE aggregated in the absence of detergent, but was solubilized in the presence of 0.2% Triton X-100 (**Figure 2-10B**). However, using Triton X-100 above CMC will also solubilize lipid bilayer if it were to be used during the encapsulation of CFE solutions.

To examine the possibility that the aggregate inside the vesicle was due to the aggregation of MscL, I examined the use of another class of surfactants made of a perfluorinated chain in its ability to solubilize MscL made by CFE. Fluorinated surfactants (FS) are amphiphilic compounds whose hydrophobic moiety consists of a perfluoroalkyl chain, usually linked to a polar head via a short hydrogenated spacer [113, 114]. In addition

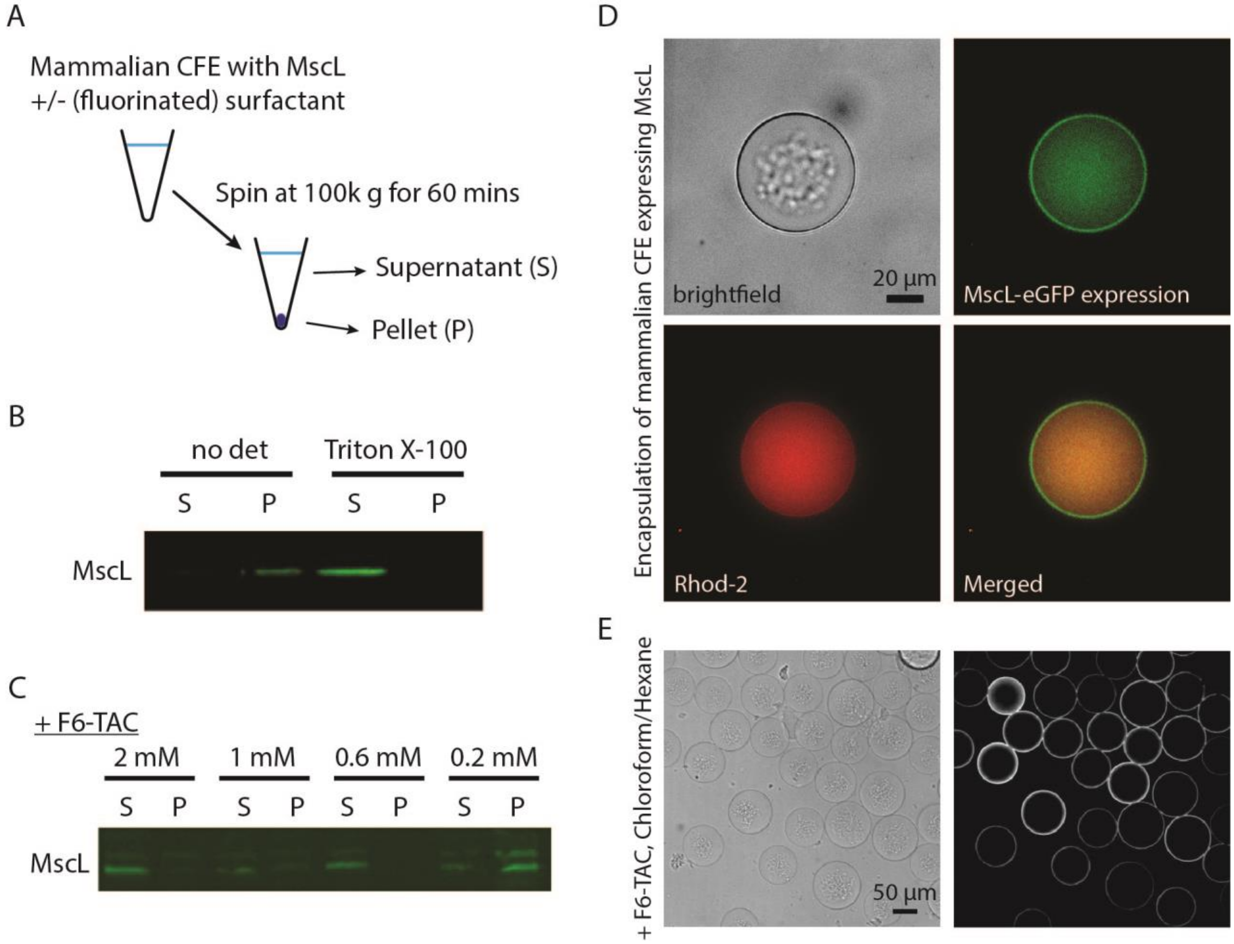

Figure 2-10: Cell-free expression of MscL is solubilized in fluorinated surfactants (A) Schematic illustration of the solubility assay for CFE of MscL. (B) Solubility of CFE of MscL after 5 hr in the presence or absence of 0.2 % of Triton X-100. (C) Solubility of CFE of MscL after 5 hr at different concentrations of fluorinated surfactant F6-TAC. (D) Formation of vesicles encapsulating mammalian CFE expressing MscL in the presence of 2% PVA and 0.6 mM F8-TAC. The vesicles were formed from 36/64 chloroform/hexane as the middle phase, and imaged in brightfield (top left) and in green fluorescence (top right). 5 µM of calcium indicator Rhod-5N and 1 mM of calcium was also encapsulated inside the vesicle (bottom left). Merged image of green and red fluorescence is shown in the bottom right. (E) Formation of HeLa lysate encapsulated vesicles formed from 40/60 chloroform/hexane in the presence of 2% PVA and 2 mM F6-TAC, imaged in brightfield (left) and in fluorescence (right).

to being chemically and thermally stable, perfluorinated chains are both hydrophobic and lipophobic, which confers peculiar properties to FS. The strong hydrophobic interactions among fluorinated chains of FS result in very stable self-assemblies in aqueous solutions.

F6-TAC is one of the fluorinated surfactants that has been used for membrane protein cell-free synthesis [115] or in membrane protein folding [116]. Solubility of MscL increased with F6-TAC concentration with almost no MscL found in the pellet at 2 mM F6-TAC (**Figure 2-10C**). 0.6 mM F6-TAC was the lowest concentration to yield soluble MscL. F8-TAC, the same type of fluorinated surfactants as F6-TAC but with longer fluorinated chain, also solubilized MscL at concentration higher than 0.6 mM (data not shown). Since the chaperone-like activity of F8-TAC was found to be reduced at high concentration [116], likely due to its lower CMC value compared to F6-TAC, 2 mM F6-TAC or 0.6 mM F8-TAC were used in subsequent experiments without noticeable differences.

Despite inclusion of FS in CFE when expressing MscL, aggregation was still observed inside the double emulsion template vesicle (**Figure 2-10D**). Nonetheless, MscL-eGFP was found to associate with the vesicle membrane and the calcium indicator dye occupied exclusively the lumen of the vesicle. I next wondered if the aggregates could be due to other CFE proteins not related to MscL expression. After overnight incubation at 32 degrees in a closed environment, I still found aggregates inside CFE and FS encapsulated vesicles without MscL, as clearly evident from the brightfield images (**Figure 2-10E**). These results suggest that components other than MscL are causing aggregations in my experimental system.

I next examined the effect of middle phase solvents on the formation of aggregate inside CFE-containing double emulsion templated vesicle. Toluene and hexane mixtures with chloroform are commonly used as the middle phase solvents in the generation of double emulsion droplets containing diblock copolymers or phospholipids [103, 117, 118]. 36-40% volume percent of chloroform has been shown previously to yield favorable adhesion energy between the two stabilized monolayers, thus supporting dewetting and the formation of vesicles [118]. At higher chloroform concentrations (above 43%), double emulsion droplets become unstable. Since chloroform has higher water solubility than hexane or toluene, it will diffuse into the outer phase and evaporate. The resultant hexane/toluene-rich solvent is poor for phospholipid and help drive the attraction of two lipid monolayers in a dewetting transition [103].

All the double emulsion droplets generated above used chloroform/hexane as the middle phase to dissolve the lipid mixture. Thin double emulsion droplets encapsulating mammalian HeLa CFE were generated using chloroform/toluene as the middle phase solvent. After overnight incubation at 32 degrees in a closed environment, I found aggregates on or inside the vesicles with a dark ring around many vesicles (**Figure 2-11**). Interestingly, some vesicles appeared to have dewetted ('yellow' arrows). Occasionally, I found vesicles extruded from the aggregates, suggesting a more solid or gel-like property of this aggregates. From these experiments, I concluded that the formation of aggregate was

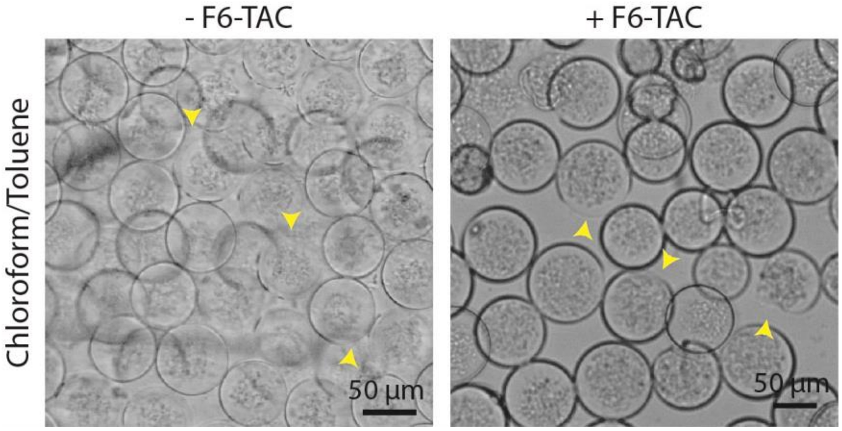

Figure 2-11: Aggregate was observed in the vesicle regardless of organic solvents Formation of HeLa lysate encapsulated vesicles formed from 40/60 chloroform/toluene in the presence (right) or absence (left) of 2 mM F6-TAC. Yellow arrowheads denote the appearance of dewetted interface.

likely not due to the insolubility of MscL or the type of organic solvents used as the middle phase.

2.3.3.3 Aggregate formed in the presence of 2% PVA

I speculated the aggregates could be precipitation of proteins in cell lysates over the course of the experiment due to some unknown chemical reactions between the lysate and the surfactant used in double emulsion generation. Formation of thin shell double emulsion droplets consists the use of poly(vinyl alcohol) (MW: 13,000-23,000; 87-89% hydrolyzed) (PVA) at 2 wt% in the inner phase and 10 wt% in the outer phase [100, 103]. PVA of this type has been widely used as a polymeric surfactant in enhancing the stability of double emulsion droplets. To test whether the aggregates were a result of the PVA surfactant, I mixed mammalian CFE with different concentrations of PVA surfactant under bulk condition, which is a simple and facile approach for testing different conditions without the influence of middle phase organic solvents. Consistent with the findings in double emulsion templated vesicles, I observed macroscopic aggregates at 2% PVA (**Figure 2-12A**). However, these macroscopic aggregates did not appear when PVA concentration was lower than 2% (smaller aggregates were visible for 1% PVA). I further performed CFE of enhanced green fluorescence protein (eGFP), under bulk conditions, at different concentrations of PVA. Interestingly, I also observed a concentration dependent decrease of eGFP expression with PVA concentration. At 2% PVA concentration, I found the eGFP expression was reduced to ~40% compared to that without surfactant (**Figure 2-12B**). This result points to the possibility that the use of droplet stabilizing surfactant PVA plays a role in generating the macroscopic aggregates and reduces cell-free protein expression.

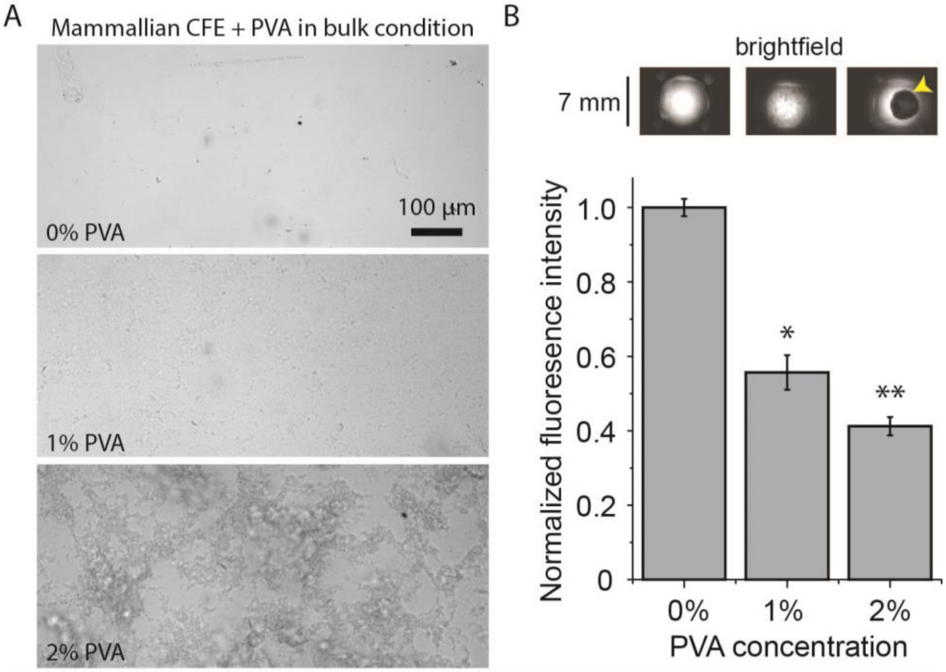

Figure 2-12: PVA surfactant caused the formation of aggregate and reduced CFE activity
(A) Brightfield images of mammalian CFE at 0, 1, or 2% of PVA surfactant. (B) eGFP expression in HeLa CFE as a function of PVA concentration measured in microwell plates (n = 3, ±S.E.), unpaired t test comparing with 0%; *: $p < 0.01$; **: $p < 0.001$. Brightfield images of microwell corresponding to the different PVA concentration are shown on top. Yellow arrowhead points to the large aggregate in the microwell.

2.3.3.4 Pluronic surfactant also generated aggregates

Since the surfactant PVA causes aggregation in the experimental system, I next examined the propensity for aggregate formation with other biocompatible surfactants. Another common surfactant used in emulsification process and in cell culturing is block copolymers of polyoxyethylene-polyoxypropylene-polyoxyethylene (PEO-PPO-PEO, also known as Pluronic). The hydrophilicity of Pluronic is determined by the different numbers of the repeating units of PEO (relatively hydrophilic) and PPO (relatively hydrophobic). When I used Pluronic F-68 instead of PVA as the surfactant without encapsulating HeLa lysate, I could immediately observe dewetting, as indicated by the formation of a small lipid reservoir, evident in both brightfield and fluorescence images (**Figure 2-13A**). At 2% surfactant concentration, the formation of aggregates was observed with three different Pluronic surfactants, F68, F88, and F127 (**Figure 2-13B inset**). Pluronic F68, F88, F127 are widely used in cell culture and are compatible with biological components. Pluronic F88 and F127 had significant reduction in protein expression compared to Pluronic F68 (**Figure 2-13B**). The absence of middle phase solvents in these experiments again supports the idea that the interaction between surfactant and mammalian CFE alone is sufficient for the formation of these macroscopic aggregates over time. Nonetheless, CFE could still

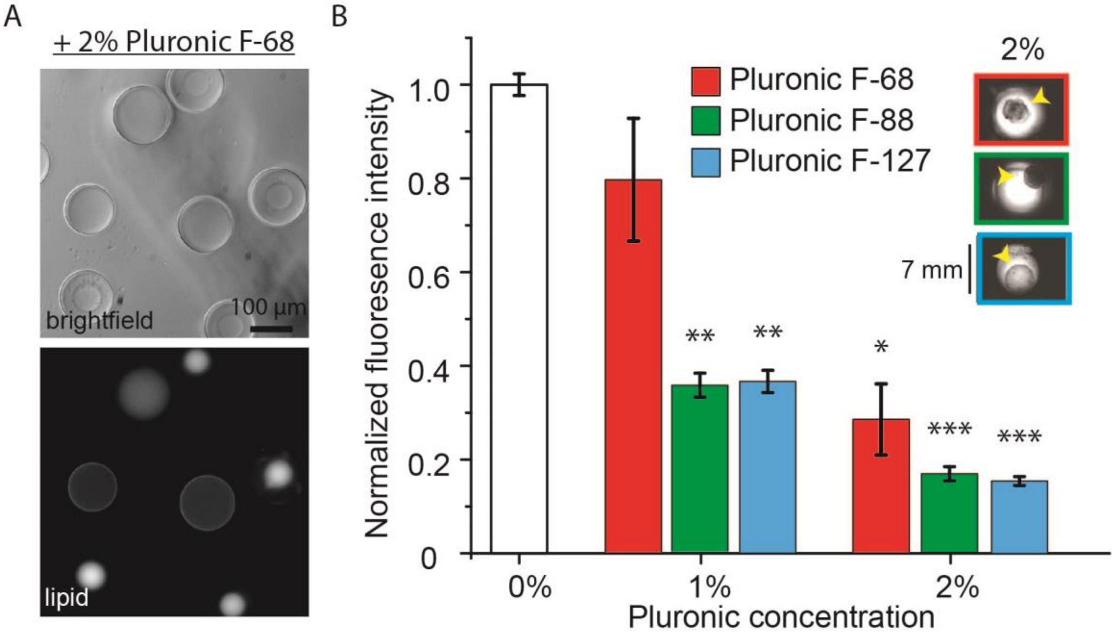

Figure 2-13: Pluronic surfactant also caused the formation of aggregate and reduced CFE activity
(A) Brightfield (top) and fluorescence (bottom) images of double emulsion templated vesicles (without HeLa lysate) with 2% Pluronic F-68. (B) eGFP expression in HeLa CFE at different concentrations of surfactants for Pluronic F-68 (red), F-88 (green), and F-127 (blue), unpaired t test comparing with 0%; *: $p < 0.01$; **: $p < 0.001$; ***: $p < 0.0001$. Inset shows brightfield microwell images at 2% of surfactant concentration with yellow arrowhead pointing to the aggregates.

occurred at some capacity. Although I could not observe large aggregates at 1% surfactants, double emulsion droplets would fail to be produced at 1% surfactant.

2.3.3.5 Aggregate formed under high concentration of mammalian CFE

Since having surfactants is important for stabilizing double emulsion droplet generation, I wondered if the lysate concentration could play a role in the formation of the aggregates. I tested this under bulk condition and used a single emulsion setup containing 2% PVA at different HeLa lysate dilutions to simulate the encapsulated environment. Single emulsion setup is a quick and easy way of creating an encapsulated environment without the presence of volatile organic solvents. At 100% mammalian CFE concentration (11.2 ± 1.0 mg/mL), I could find aggregates under bulk condition and in single emulsion with 2% PVA across different droplet sizes. Interestingly, I no longer observed aggregates when the CFE concentration was diluted to 40% under bulk condition or 60% in single emulsion (**Figure 2-14A**). While this result seems encouraging, I find rapidly diminishing eGFP expression with dilution of the entire CFE system (**Figure 2-14B, left**) or dilution of the HeLa lysate alone by varying the volume ratio between lysate and Mix 1 (**Figure 2-14B, right**).

In support of the discovery that the high concentration of mammalian HeLa lysate in conjunction with surfactant led to the formation of aggregates, I find no aggregates when I mixed bacterial CFE system with 2% PVA (**Figure 2-15A**) or encapsulated bacterial CFE system (6.4 ± 0.9 mg/mL) using double emulsion templated vesicles (**Figure 2-15B, top**). In particular, 2% PVA has no impact on the expression of eGFP by bacterial CFE (**Figure 2-15B, bottom**). This result agrees with two recent publications, in which no aggregates

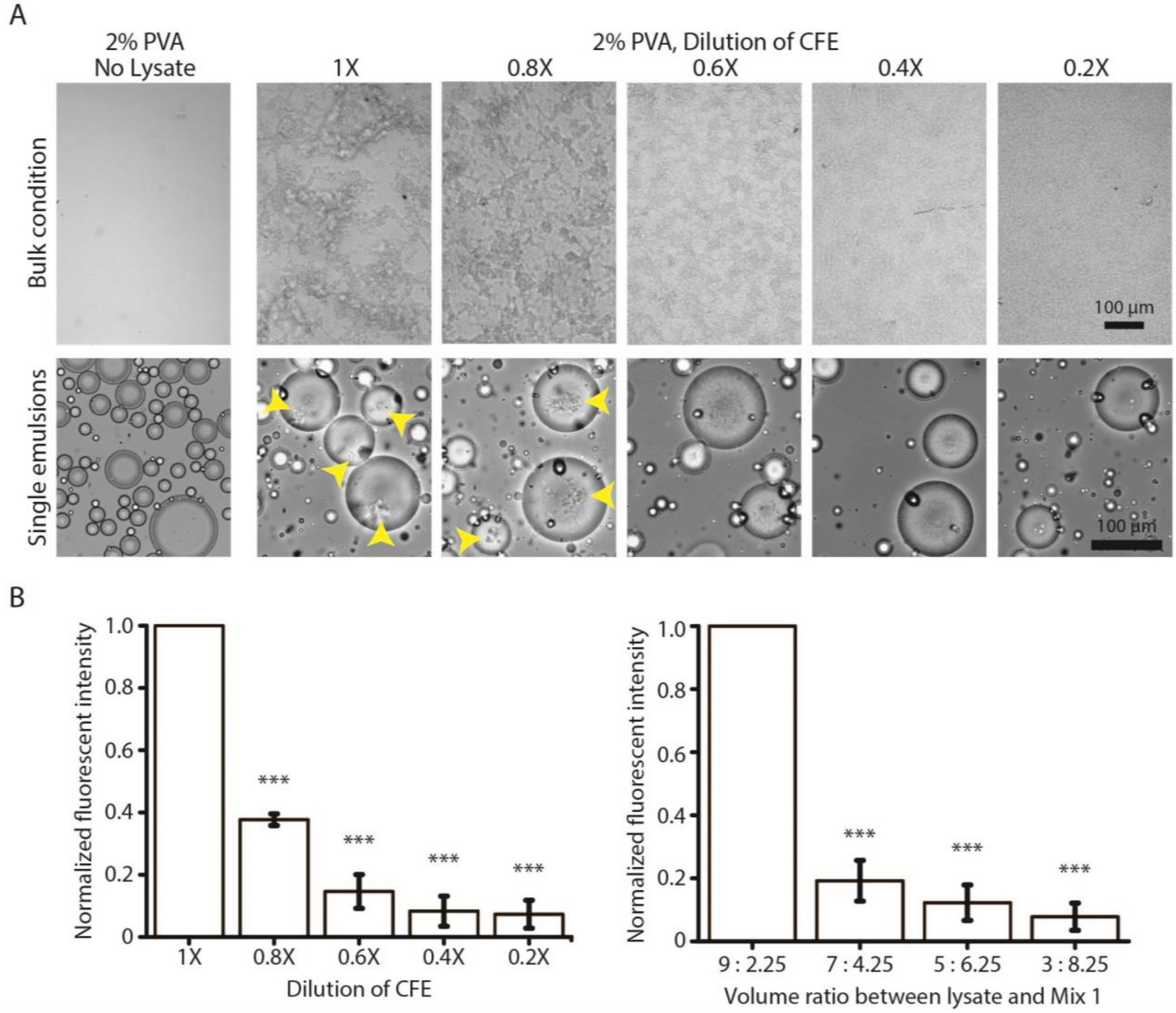

Figure 2-14: High concentration of mammalian Hela lysate is prone to aggregation when exposed to surfactant
(A) (Top) Representative brightfield images of different dilution of CFE reaction with 2% PVA under bulk condition. (Bottom) Representative brightfield images of single emulsions encapsulating 2% PVA at different CFE dilutions. Yellow arrowheads denote the appearance of aggregates. (B) (Left) eGFP expression in HeLa CFE as a function of CFE dilution measured in microwell plates (n = 4, ±S.E.), unpaired t test comparing with 1X; ***: $p < 0.0001$. (Right) eGFP expression in HeLa CFE at different volume ratios between lysate and Mix 1 measured in microwell plates (n = 4, ±S.E.), unpaired t test comparing with 9:2.25 volume ratio; ***: $p < 0.0001$.

were found when bacterial CFE system were encapsulated with 2% PVA using double emulsion templated vesicles [94, 95].

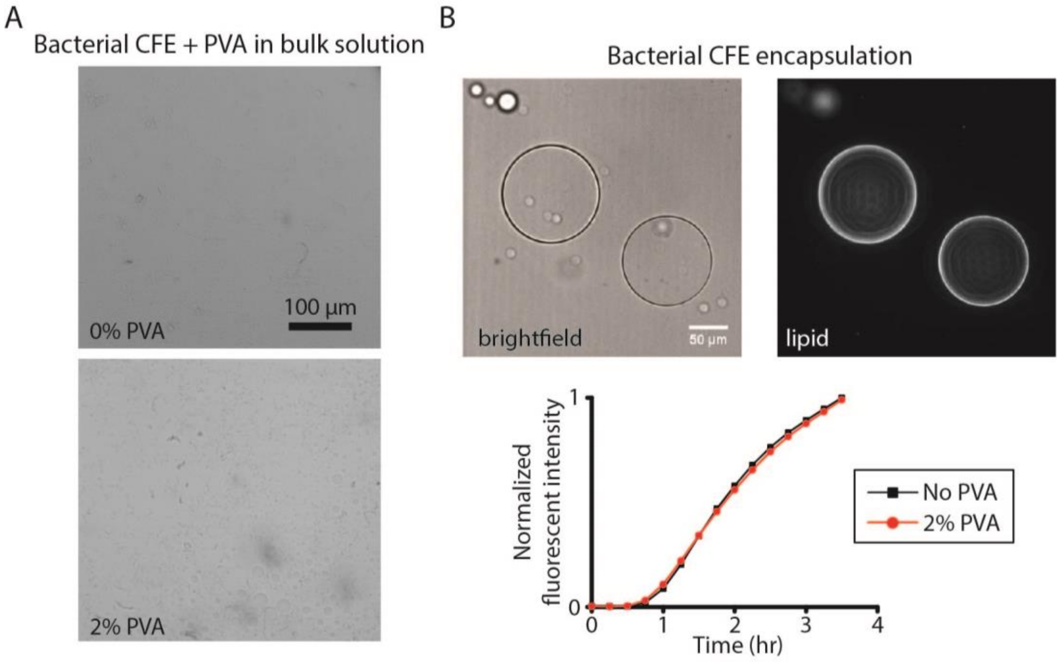

Figure 2-15: No aggregate formed in bacterial CFE
(A) Brightfield images of bacterial CFE without (top) and with (bottom) 2% of PVA surfactant (B) Bacterial CFE encapsulation in double emulsion templated vesicles, imaged in brightfield (top left) and in lipid fluorescence (top right). (Bottom) eGFP expression in bacterial CFE over time with and without 2% PVA measured in microwell plates.

2.3.3.6 Actin aggregated with PVA

Thus far, I found that high concentration of mammalian HeLa lysate in conjunction with PVA surfactant led to the formation of aggregates. However, I have not identified component(s) that formed these aggregates. To further investigate this, the mixtures of mammalian CFE with different concentrations of PVA surfactant were centrifuged to separate the aggregate/pellet and the supernatant. While the overall amount of proteins in the supernatant and pellet fractions at different concentrations of PVA did not appear to change significantly (**Figure 2-16A**), I saw more protein of molecular weight around 40-45 kDa in the pellet fraction at 1% PVA. To identify the specific protein aggregating with PVA, the protein band was cut out and LC-tandem mass spectrometry was performed. Actin was identified as the major protein in the sample (mass spectrometry; 17.8% and 21.5% of peptides were actin at 1% and 2% PVA respectively for peptide count > 1). The aggregation of actin with PVA surfactant was also verified using Western blot (**Figure 2-16B**). The percentage of actin in the pellet fraction increased significantly when the mammalian CFE was incubated with 1% or 2% of PVA surfactant (**Figure 2-16C**). Interestingly, the percentage of actin in pellet at 2% PVA is lower than that at 1% PVA. I speculated that this is due to the inability of detergent to fully solubilize the proteins in the aggregate. This can

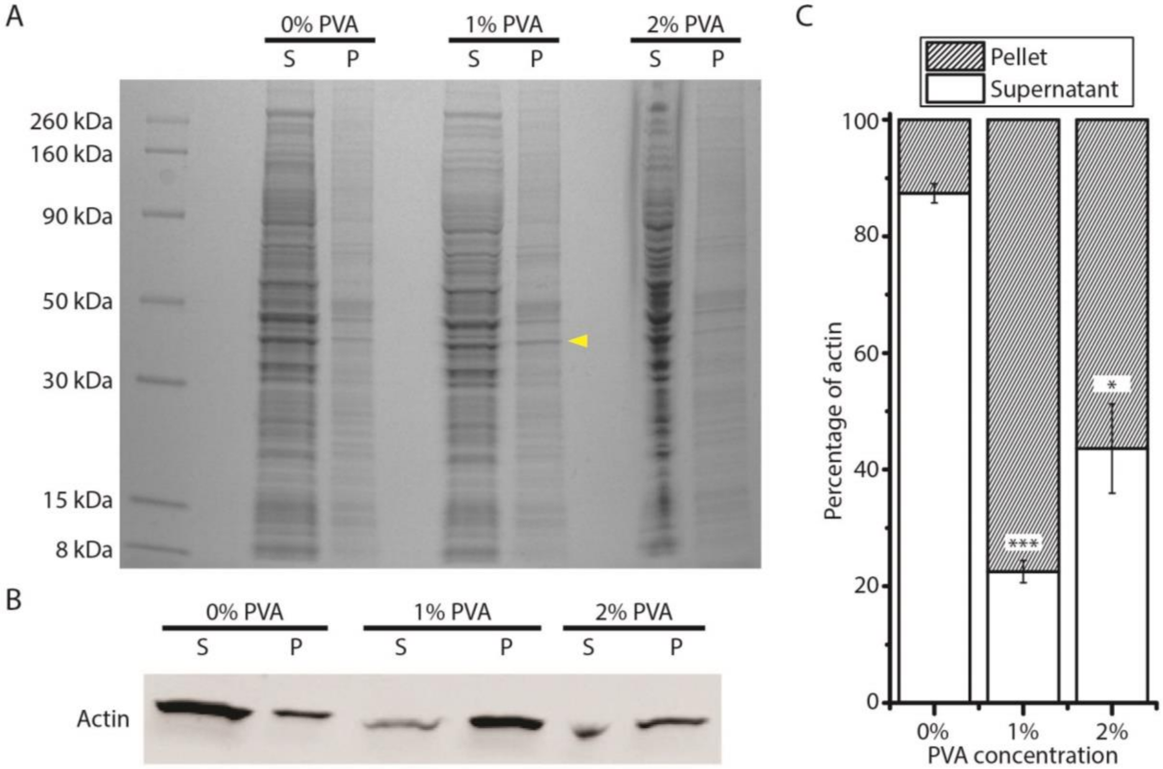

Figure 2-16: Actin aggregates with PVA surfactant
(A) Coomassie blue stained gel showing proteins in the supernatant or pellet after 10 min centrifugation at 16,100 g, in the presence of PVA surfactant at different concentrations. (B) Western blot showing the actin in the supernatant or pellet fractions at different PVA concentrations. (C) Percentage of actin measured in the supernatant and pellet fractions at different PVA concentrations (n = 3, ±S.E.), unpaired t test comparing with 0% PVA; *: $p < 0.01$; ***: $p < 0.0001$.

also explain why I did not see a significant amount of proteins in the pellet fraction. Nevertheless, the results indicate that actin was one of the proteins that aggregated with PVA in the mammalian CFE reaction and I believe the concentrations of other proteins that are important for transcription and/or translation could also be reduced due to a similar mechanism.

2.4 Conclusions

This chapter reports the development of a simplified model of a cell for potential cell mechanics study. The double emulsion template was developed for the generation of lipid vesicles, allowing the encapsulation of actin networks or mammalian CFE system. The encapsulated actin bundled network was confined inside the lipid vesicles, but not interacting with or binding to the lipid membrane. To further create a better model of cell, actin binding proteins that interact with lipids can be introduced in the vesicles.

As a yet untapped area of encapsulating mammalian CFE system as the 'cytosol' of lipid membrane-enclosed artificial cells, I reported a systematic study to examine the effect of PVA surfactant on mammalian CFE-containing double emulsion templated vesicles. Although I found 2% PVA surfactant reduces protein expression and led to the formation of macroscopic aggregates in mammalian HeLa CFE, 2% PVA surfactant is critical for stable microfluidic double emulsion generation. I showed that the high protein concentration in HeLa CFE and PVA surfactant present a condition for these aggregates to form. I further discovered that even when the macroscopic aggregates only appeared when the concentration of PVA surfactant reached 2%, actin is one of the proteins in the mammalian CFE that aggregated with PVA. With the hydrophobic and hydrophilic parts of the PVA surfactant, it is not surprising to see that proteins important for cell-free synthesis could also be aggregating with PVA. My work thus provides a baseline description of the current state-of-the-art in encapsulation of mammalian CFE system in double emulsion templated vesicles and offer directions for further improvement and optimization for the building of a simplified model of a cell.

Overall, our simplified model of a cell with actin bundled network or mammalian CFE is a step towards building artificial cell with the functions and properties of cells, so that it can be used for cell mechanics study in the future.

Chapter 3: Prototyping a microfluidic compression device for mechanically activating artificial cell

** This chapter has been published in Ho et al., Scientific Reports, 2016.*

3.1 Introduction

3.1.1 Engineering artificial cell

Engineering artificial cell to mimic one or multiple functions of a cell is an emerging area of synthetic biology. Engineering artificial cells is a high-risk, high-reward path towards the advancement of both basic and applied science. Venter and coworkers have spent more than 15 years until they finally succeeded in designing and chemically synthesizing a minimal bacterial genome for transplantation into a host bacterium, thereby producing a minimal autonomously replicating cell [119]. The synthesis of minimal self-replicating cells helps to answer many basic scientific questions about the minimum genome to support life and also opens up new applications, such as novel vaccine development and sustainable bio-fuels.

Bottom-up *in vitro* reconstitution is an alternative approach in engineering artificial cells by which cellular functions are reconstituted by component macromolecules to study cellular assembly and organization [16]. While cell biology has generated a wealth of knowledge about cellular pathways and processes, a purely top-down approach cannot provide complete understanding into how mixtures of macromolecules assemble and organize dynamically into spatially complex structures or generate emergent behaviors.

Bottom-up reconstitution offers a way to peel away cellular complexity through building from cellular components [120], and building bio-inspired artificial cells where inherent complexities of living cells are stripped away holds tremendous promise in a broad range of applications [121]. Kurihara *et al.* built a protocell that responds to external environmental stimuli and demonstrated self-proliferation over multiple generations [122]. This work illustrates how assembly of well-defined lipids and macromolecules could emerge into a collaborative and dynamic system. Engineering artificial cells can also advance applied science in other creative ways. For example, Lentini *et al.* engineered an artificial cell to translate unrecognized signals into chemical language that *E. coli* can recognize to expand the sensory capacities of *E. coli* without changing their genetic content [123].

3.1.2 Challenges in synthesizing cell-like artificial cells

Bottom-up synthesis of cell-like artificial cells faces two general challenges – encapsulation and stability. With advances in droplet microfluidics, artificial cells can now be generated in a high-throughput manner with high encapsulation efficiency. As a chassis of artificial cells, droplet microfluidics has been used to aid the synthesis of liposomes by double emulsion template [103], layer-by-layer assembly [124, 125] and microfluidic jetting [126, 127]. As a promising approach towards building artificial cells, cell-free expression components were encapsulated within a lipid bilayer platform by droplet microfluidics [94, 100, 128]. However, building artificial cell systems directly with lipid bilayer has challenged many research groups, mainly due to low stability of artificial cells. Encapsulation of complex solutions (e.g. cell free expression system) poses unique challenges that could stem from the chemistry of current droplet microfluidics approaches for making lipid bilayer vesicles [129]. Furthermore, without cytoskeleton networks that exist in all natural cells to provide mechanical support and adaptation to surrounding environment, liposomes with sizes comparable to natural cells (~10 μm) are vulnerable to environment challenges, for example, osmotic shock. These difficulties have motivated me to use double emulsion droplets (aqueous/oil/aqueous) as an alternative model system to prototype artificial cells. Indeed, numerous studies have used single or double emulsions or other compartmentalized schemes as artificial cells [130, 131].

3.1.3 Microfluidics: tool for mechanically activating artificial cells

Current engineered artificial cells have been limited to sensing chemical inputs or physicochemical properties of membrane [123, 132, 133], while the idea of engineering a mechanosensing artificial cell has never been conceived. Mechanical forces are arguably the most primitive signal and mechanosensation is universal to all living organisms [134]. In principle, a mechanosensing artificial cell could be engineered to sense and respond to mechanical forces, such as shear, tensile, or compression forces. To demonstrate the construction of mechanosensing artificial cell, a precisely controlled platform is required to physically apply mechanical forces to artificial cells. Microfluidics provides a platform with precise microenvironment control and it has been utilized in numerous applications in synthetic biology, ranging from automated DNA assembly [135, 136], automated genetic engineering [137], to precise control of bacterial culture [138]. Microfluidic technology and synthetic biology have also been combined together for studying different genetic circuit systems, such as metabolic gene network [139], synchronizing genetic oscillations [140, 141] and molecular clocks [142]. Recently, microfluidics was used to engineer on-chip artificial cells [131, 143]. The growth of microfluidics in synthetic biology applications is clearly evident. In the context of the present study, microfluidics can provide precise mechanical input to artificial cells. Microfluidics technology has been widely adopted in single cell mechanobiology studies where the effect of different modes of mechanical forces on cellular functions have been investigated [43-46, 83, 84]. Thus, the capability and controllability of microfluidics offer a versatile platform for engineering and studying mechanically activated artificial cells.

As a first step, I developed a multilayer microfluidic platform to trap and apply mechanical forces to single artificial cells. I used double emulsions generated from droplet microfluidics as a model of artificial cell similar to what was described in Chapter 2. The novel microfluidic device could compress or aspirate on double emulsion droplets to increase or decrease the thickness of oil in the middle phase, respectively. By thinning the oil phase, I demonstrated the influx of calcium ions as a biological response of the mechanically activated artificial cell. The influx of extracellular calcium ions is one of the most important signaling pathways found in living cells, where calcium ions serve as secondary signaling messengers and exert regulatory effects on different enzymes and proteins. The study here combining microfluidics and artificial cells opens up new possibilities in the development of force-activated synthetic biology.

3.2 Model of mechanosensing artificial cell

In biological systems, selectively permeable membrane is composed of a thin single bilayer of lipid molecules with a thickness of ~5 nm. Membrane proteins such as transporters and ion channels are important in controlling transport of chemicals and ions across the membrane. Mechanosensitive channels that are responsive to membrane tension are found from bacteria (e.g. MscL) to mammalian cells (e.g. Piezo 1) [144, 145]. Reconstituting mechanosensitive channel activity as a path towards constructing mechanosensitive artificial cell is a challenging, yet promising approach. As an alternative model to lipid bilayer vesicles, double emulsion droplets can be used to prototype artificial cells (**Figure 3-1A**). As water and oil are immiscible with each other, the middle oil phase separates the inner and outer aqueous phase to form double emulsion. The thickness of the oil dictates the transport of hydrophobic solute via diffusion [146] or by reverse micelles in the presence of osmotic mismatch [147]. To prototype mechanosensing artificial cells, I

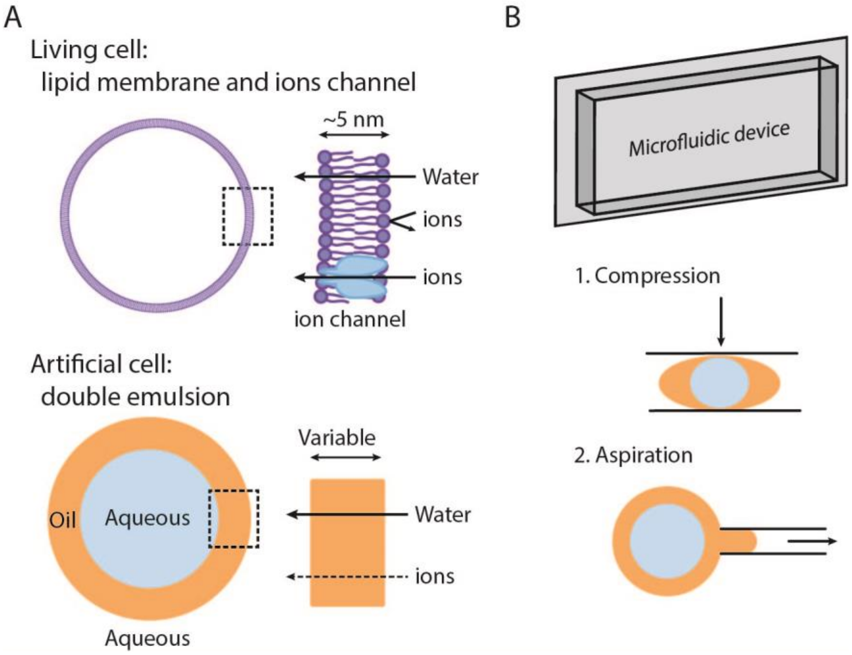

Figure 3-1: Prototyping mechanosensing artificial cells
(A) Lipid bilayer partitions the internal environment of a cell where ions do not cross. Double emulsion can serve as a model of an artificial cell where the oil middle phase can vary in thickness and acts as a semipermeable barrier for ions to pass through. (B) A microfluidic device can be utilized to compress or aspirate on double emulsions as a way to alter oil thickness and mechanically activate artificial cells.

investigated the possibility of using compression and aspiration to alter oil thickness in double emulsion as a mechanism to mechanically activate artificial cells (**Figure 3-1B**).

3.3 Microfluidic device overview and design

To demonstrate the construction of mechanosensing artificial cells, a microfluidic device is designed to trap double emulsions into trapping chambers, and apply compression and aspiration to them in a parallel manner. The device, made out of polydimethylsiloxane (PDMS), has two layers, the flow layer and the control layer (**Figure 3-2**). The flow layer (blue) has a similar design as the previously reported microfluidic pipette array (μFPA) device in the lab [46] where fluid and double emulsions flow from one inlet through the microfluidic channel to one outlet. The microfluidic channel first splits into two channels, each containing 7 trapping chambers. Each trapping chamber is connected to the opposing end of the main microfluidic channel through a small microchannel, akin to a micropipette that can perform aspiration. The flow layer is designed such that the flow resistance of the small microchannel is 20 times larger than that of the main microfluidic channel. Thus, flow is directed primarily through the main microfluidic channel and not through the trapping chambers. A thin PDMS membrane separates the microfluidic channel and the control layers (pink and orange) that serve two different functions and are independently controlled (**Figure 3-2B**). To direct flow to the trapping chambers, a pneumatically controlled valve set located above the microfluidic channel blocks the flow in the main microfluidic channel when the valve set (Control valve set 1, pink) is actuated. A second control valve set (Control valve set 2, orange) directly above the trapping chambers exerts compression to trapped double emulsion when the

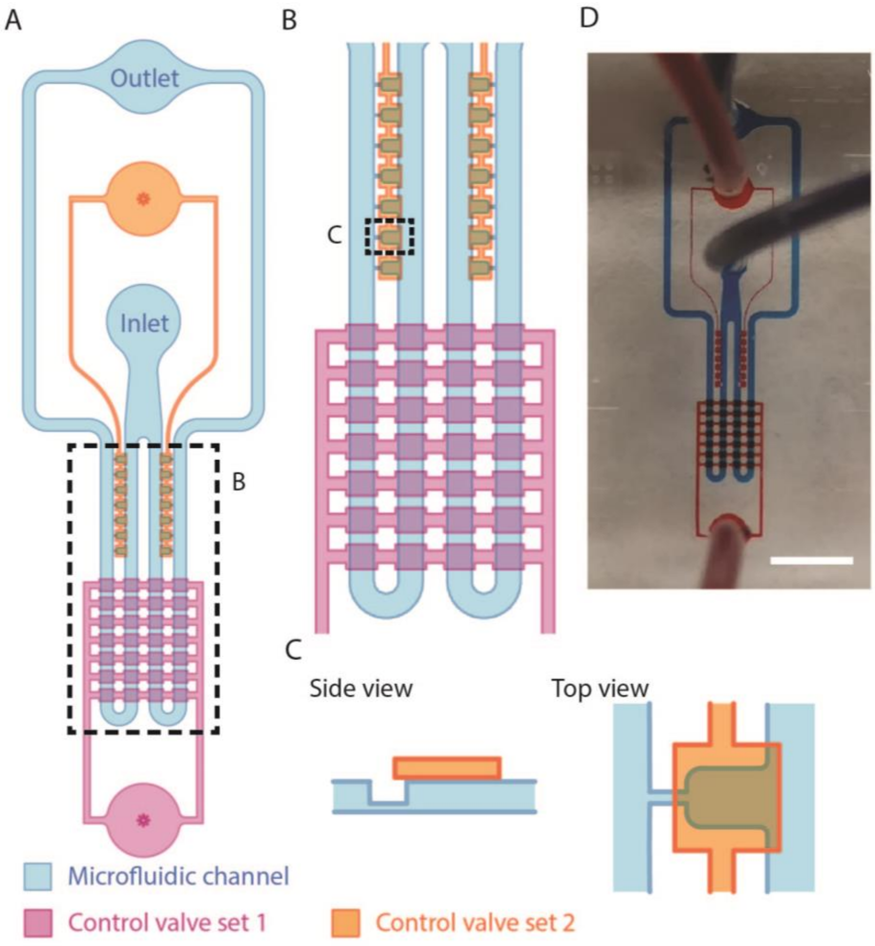

Figure 3-2: Overview and design of the microfluidic device
(A) The design of the microfluidic device is shown. The device has two PDMS layers that consist of a deformable microfluidic channel and two independent control valve sets. (B) Close-up view of the control valve sets from the dotted box in (A). Control valve set 1 facilitates the trapping of droplets inside the trapping chambers and Control valve set 2 provides in-plane compression of the trapped droplets. (C) Top view (top) and side view (bottom) of a trapping chamber. The microfluidic channel is beneath the control layer and is separated by a thin, deformable PDMS membrane. The pipette structure adjacent to the trapping chamber locates at the bottom of the microfluidic channel. (D) A picture of the actual device connected with micro-tubings: blue and red color dyes label the microfluidic channel and control valve sets respectively, scale bar = 3 mm.

valve set is actuated. Since the two control valve sets can be independently controlled, trapping is decoupled from compression.

3.4 Materials and methods

3.4.1 Glass capillary microfluidic device

Glass capillary microfluidic device used in this chapter has a different design comparing to the one described in Chapter 2 to generate double emulsions with thicker middle phase. The device was fabricated by assembling tapered round capillary, square capillary and syringe needles together using 5 minutes epoxy (**Figure 3-3**) [98]. First, the round glass capillary (Sutter Instrument B100-58-10) was pulled using a pipette puller (Sutter Instruments P-87). The tapered capillary was then sanded using 1200 grade sandpaper to obtain a 100 μm opening for the collection tube. The outside surface of a clean 15 μm opening injection tube, pulled and similarly sanded, was treated with trichloro(1H,1H,2H,2H-perfluorooctyl)silane to render the surface hydrophobic. Then, the injection tube and collection tube were inserted into a square capillary (AIT, 810-9917) placed on a glass slide and they were aligned under an optical microscope. Syringe needles (McMaster Carr, 75165A677) were cut and glued to the glass slide using 5 minutes epoxy (Devcon, 14250). Lastly, micro-tubings (Scientific Commodities, BB31695-PE/5) were connected to the syringe needles.

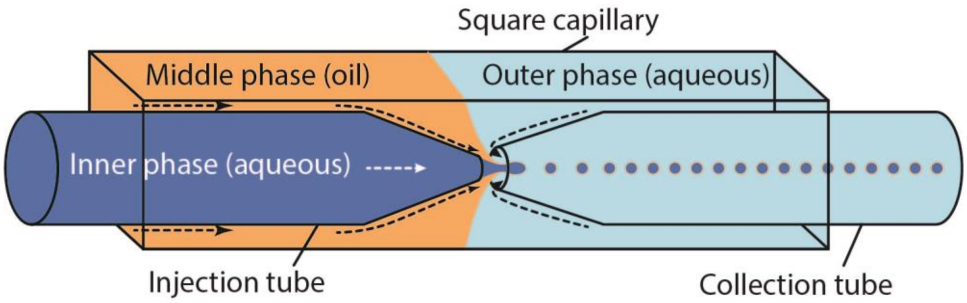

Figure 3-3: Glass capillary microfluidic device for formation of double emulsions
The glass capillary microfluidic device is fabricated by aligning two tapered round capillaries inside a square capillary. Monodisperse double emulsion droplets form when the inner aqueous phase, middle oil phase and outer aqueous phase are pumped into the device in the corresponding compartments.

3.4.2 Double emulsions generation

For a stable double emulsion system, I used fluorinated oil (HFE-7500, RAN Biotechnologies) with fluorosurfactants, which was synthesized by coupling oligomeric perfluorinated polyethers (PFPE) with polyethyleneglycol (PEG) [148], as the middle phase. Monodisperse double emulsions were generated using the glass capillary microfluidic device described in the previous section. The inner aqueous phase contained 20 µM rhodamine succinimidyl dye (Fisher scientific, 50-851-056) or 100 µM Rhod-2 (Thermo Fisher Scientific, R-14220), 800 mM glucose, 20 mM HEPES pH7.5, 250 µM EGTA. The middle oil phase contained 2 wt% 008-FluoroSurfactant in HFE7500. The outer aqueous phase contained 10 wt% Poly(vinyl alcohol) (PVA) (Sigma, MW 13,000-23,000, 87-89% hydrolyzed) or 8 wt% PVA, 300 mM $CaCl_2$, 20mM HEPES pH7.5, 250 µM EGTA. The three phases were pumped into the glass capillary microfluidic device using three OEM syringe pumps (New Era Pump Systems, NE-500). For the 65 µm double emulsion that had an oil thickness of 11 µm, the flow rate used for the inner, middle and outer phases were 450, 700, 6000 µl/hr respectively. The flow rate of the middle phase and outer phase were set at 400 and 8000 µl/hr for a thinner and smaller double emulsion; and at 900 and 5000 µl/hr for a thicker and larger double emulsion.

3.4.3 Device fabrication

The microfluidic device was fabricated using multilayer polydimethylsiloxane (PDMS) soft-lithography technique [149]. The microfluidic device is composed of a PDMS control layer and a PDMS flow layer, which were aligned and bonded permanently onto a PDMS coated microscope glass slide.

Three photomasks were produced by high resolution inkjet printing on transparency film (CAD/Art Services) for SU-8 patterning of two silicon molds by standard photolithography. The first silicon mold is composed of one layer of SU-8 pattern for PDMS casting of the control layer. The SU-8 pattern of the control layer defined two sets of integrated microfluidic control valves for closing of the main microfluidic channel (Control valve set 1) and deflections of the flow layer in the trapping chambers for planer compression of double emulsions (Control valve set 2) respectively. These two sets of microfluidic control valves contained two independent inlets. The other silicon mold is composed of two layers of SU-8 patterns to be used for PDMS spin-coating of the flow layer. The first SU-8 patterning layer defined the side microfluidic pipette channel for aspiration. The second SU-8 patterning defined the main microfluidic channel, the trapping chambers, and a single pair of inlet and outlet.

The SU-8 patterning procedures of the two silicon molds followed the standard protocol developed by Microchem, Inc. for SU-8 2000 [150]. First, two silicon wafers were dehydrated on a hotplate at 200^{o}C for 15 min to promote photoresist adhesion. In SU-8 patterning the silicon mold for the control layer, SU-8 2025 was spin-coated at 1500 rpm onto the wafer for 30 s, which gave a thickness of 45 μm. The photoresist was then exposed to UV light for 20 s under a contact aligner (Karl Suss, MJB45). In the first SU-8 patterning of the flow layer, SU-8 2010 was spin-coated at 1500 rpm onto the silicon wafer for 30 s, which gave a thickness of 16 μm. The photoresist was then exposed to UV light for 15 s with the first flow channel photomask, which defined the side pipette arrays. After development of first SU-8 layer, the silicon wafer was hard-baked at 200^{o}C for 20-30 minutes to consolidate the developed SU-8 patterns before the application of the second

SU-8 layer. Subsequently, for the second layer SU-8 patterning of the flow layer, SU-8 2025 was spin-coated at 1500 rpm onto the silicon wafer for 30 s, which gave a combined thickness of 60 μm. The photoresist was then aligned with the second flow channel photomask, which mainly defined the main microfluidic channel, and exposed to UV light for 20 s. After development of SU-8, both silicon molds were hard-baked at 200°C for 20-30 minutes again to cure any surface cracks. The thicknesses of both the control layer and flow channel SU-8 pattern were measured using a stylus profilometer (Dektak 6M).

Before PDMS casting or spin-coating on the silicon molds, both wafers were first silanized with trichloro(1H,1H,2H,2H-perfluorooctyl)silane (Sigma-Aldrich) in a desiccator for 1 hour. The silicon mold for the control layer was casted with PDMS (Sylgard-184) with a mixing ratio of 7:1 (base:curing agent). After degassing in a desiccator, the control layer PDMS substrate was then cured at 60°C overnight before demolding from the wafer. The PDMS substrate was then diced and holes were punched with 1 mm diameter at the inlets of the microfluidic control valves. The flow channel membrane was generated by spin-coating PDMS with a mixing ratio of 20:1 (base:curing agent) on the flow layer silicon mold at rotational speeds between 1000 to 1600 rpm for 30 s. After this, the PDMS flow layer membrane was cured at 60°C for 2 hours. Both the diced PDMS control substrate and the PDMS flow layer membrane on the silicon mold were placed in an oxygen plasma etcher (Femto, Covance) to render the PDMS surfaces hydrophilic for the preparation of bonding procedure described as follows. The flow layer silicon mold containing the PDMS membrane was mounted on a customized alignment platform on an optical microscope. The diced PDMS control layer substrate was then careful aligned and bonded with the PDMS flow layer membrane. The permanent bonding between the control layer substrate and PDMS flow layer membrane was established by heating in the furnace at 60°C overnight with the aid of gentle pressing between two substrates. The day after, the bonded control layer substrate with the flow layer membrane was then cut out and peeled off from the flow layer silicon wafer. Inlet and outlet holes (1 mm diameter) for the main microfluidic flow channel were punched through the layer PDMS control/flow substrate. Finally, the PDMS substrate was bonded to a PDMS-coated microscope glass slide following the procedures of two-hour PDMS curing and oxygen plasma treatment as described previously. Schematic of the fabrication process flow of the microfluidic device can be found in **Figure 3-4**.

3.4.4 Imaging membrane deflection and 3D image reconstruction

The microfluidic device was mounted on a spinning disk confocal microscope (Olympus IX73 with Yokogawa CSU-X1) for image acquisition using a 20X objective. Four different micro-tubings were connected to the microfluidic device. The control layer inlets of the microfluidic device were connected through 4-way stopcock switches (Nordson, FC series) to a compressed air source with a pressure regulator (Norgren). Rhodamine succinimidyl dye (Fisher scientific, 50-851-056) was flowed into the device through the inlet of the flow channel using a syringe pump. By setting the position of the stopcock switches, compressed air of pressure ranging from 0 psi to 30 psi was applied to deflect the PDMS membrane above the trapping chambers. A z-series of fluorescence images, excited at 561 nm, was captured at a step size of 1 μm and was reconstructed in ImageJ to generate 3D and side view images.

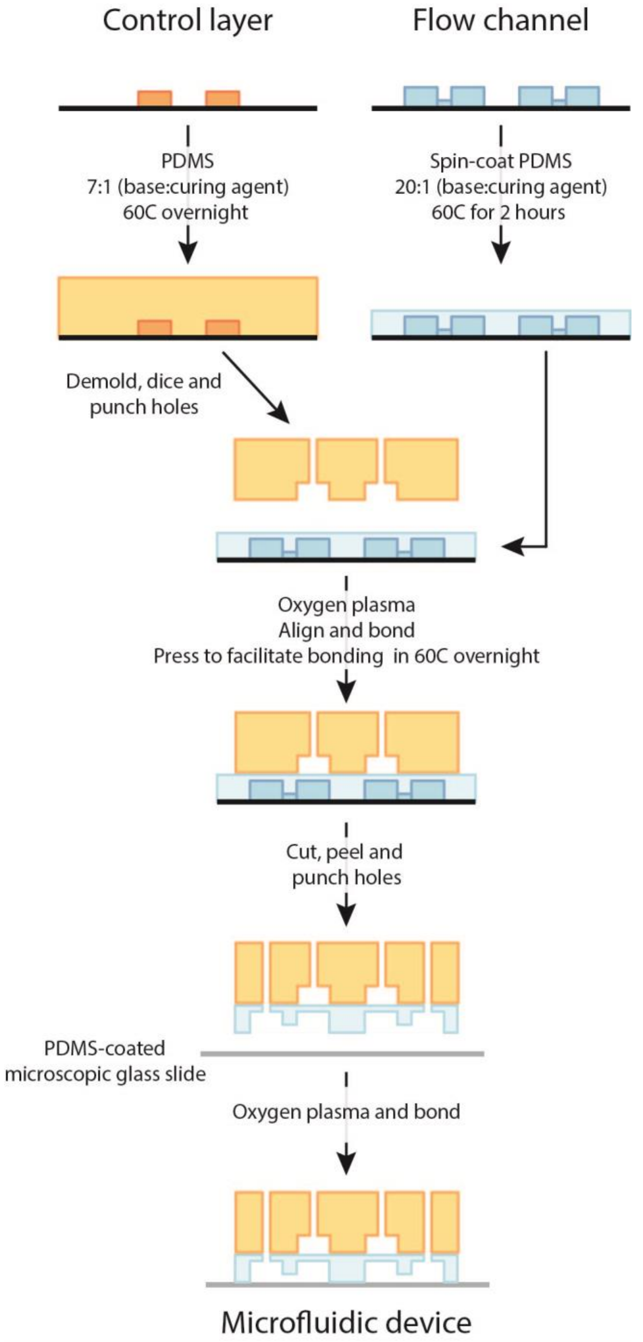

Figure 3-4: Fabrication process of microfluidic device
The silicon mold for control layer and flow channel were casted with PDMS of different mixing ratio. The PDMS substrate of the control layer was aligned with the flow channel membrane and bonded together. Finally, the PDMS control/flow substrate was peeled off from the flow layer silicon wafer and bonded to a PDMS-coated microscope glass slide to form the final microfluidic device.

3.4.5 Imaging double emulsions trapping, compression and aspiration

The microfluidic device was mounted on an optical fluorescent microscope (Nikon, Ti Eclipse) for image acquisition using a 10X objective. The control layer inlets were connected to a compressed air source. Double emulsions were first formed as described in the glass capillary microfluidic device, encapsulating 20 μM rhodamine succinimidyl dye, and then flowed into the microfluidic device using a syringe pump at 10X dilution at 10 μl/min. For trapping double emulsions, once they reached the flow channel, the flow rate was reduced to 0.2-0.5 μl/min and 10-15 psi pressure was applied to Control valve set 1, which blocks the flow through the main microfluidic channel. Control valve set 1 was decompressed after the double emulsions were trapped in the trapping chambers, typically in under a minute. For double emulsion compression, the stopcock switches were then configured to apply compressed air to Control valve set 2. The applied air pressure varied from 0 to 30 psi. For double emulsion aspiration, no air pressure was applied to neither of the control valve sets. The pressure difference across the double emulsions were controlled by varying the flow rate in the flow channel.

3.4.6 Flow simulation

The fluid flow in the flow channel of the microfluidic device was simulated using COMSOL 4.4 (COMSOL Multiphysics). The three dimensional model of the device was constructed in Solidworks with the height of the micropipettes and main microfluidic channel as measured from the flow channel SU-8 pattern. The pressure differences across trapping chambers were simulated using the laminar flow module. The problem is computed as incompressible flow. Water was chosen as the fluid material of the entire domain. No-slip boundary conditions were used on all the walls except the inlet and outlet. The inlet was set as normal inflow velocity, which was calculated from the flow rates and cross-sectional area of the inlet. A zero constant pressure with backflow suppression was used at the outlet.

3.4.7 Hypo-osmotic shock experiment for calcium transport

Double emulsions were generated as described in the glass capillary microfluidic device, with 100 μM calcium indicator Rhod-2, 800 mM glucose, 20 mM HEPES pH7.5, 250 μM EGTA as the inner phase and 8 wt% PVA, 300 mM CaCl2, 20mM HEPES pH7.5, 250 μM EGTA as the outer phase. The osmolarity of the inner and outer phase were measured using a Vapor Pressure Osmometer (ELITechGroup, 5600) and were balanced. The microfluidic device was mounted on an optical fluorescent microscope with a 10X objective and the control layer was connected to the pressure regulator as described before. The flow channel inlet was connected to two syringe pumps using a T-junction connector. Two syringes with double emulsion solution and a hypo-osmotic solution (8 wt% PVA, 200 mM CaCl2, 20mM HEPES pH7.5, 250 μM EGTA) were connected to the two syringe pumps respectively. First, the double emulsions were pumped into the device and trapped inside the trapping chambers. Then, the outer phase was changed to the hypo-osmotic solution. The trapped double emulsions were aspirated and thinned out by increasing the flow rate of the hypo-osmotic solution. The fluorescence of the inner phase was monitored at a time interval of 5 s, and images were analyzed in ImageJ.

3.5 Results and discussion

3.5.1 Membrane deflection and compression by pneumatic control.

One of the features that the microfluidic device has is to compress trapped double emulsions in the trapping chambers. Control valve set 2 features rectangular patterns above each trapping chamber. When Control valve set 2 is pressurized, the PDMS membrane above the trapping chambers deflects and compresses the double emulsions trapped in the trapping chambers. The rectangular patterns of Control valve set 2 needs to be aligned with the trapping chambers of the microfluidic channel (**Figure 3-5A**) such that deflection of the PDMS membrane is directly over the trapping chambers. Without actuation, the membrane remains flat. When air pressure in Control valve set 2 increases and is higher than the liquid pressure in the microfluidic channel, the PDMS membrane deflects towards the flow channel (**Figure 3-5B**). The deflection of the membrane is dependent on the material property of the PDMS membrane, the thickness of the membrane and the applied pressure in Control valve set 2. To fabricate PDMS membrane with a higher elasticity for better deflection compared to PDMS with 10:1 (base:curing agent) mixing ratio [152], I chose a higher mixing ratio of 20:1 to make the PDMS membrane. By varying the PDMS spin-coating speed on the flow layer silicon mold (1000 - 1600 rpm), I can generate PDMS membrane with thicknesses ranging from 20 μm to 44 μm. To examine the deflections of membrane with different thicknesses as a function of different applied pressures, I labeled the microfluidic channel volume with rhodamine succinimidyl dye since I cannot directly label the PDMS membrane. When Control valve set 2 is pressurized, the membrane deflects and displaces the fluid in the microfluidic channel so that I can indirectly visualize membrane deflection. The reconstructed 3D and side view images of the compressed trapping chamber showed the increase in membrane deflection with increasing applied pressure (**Figure 3-5C**). Importantly, the PDMS membrane contacts the bottom of the flow channel at 30, 25 and 20 psi for devices with PDMS spin-coating speeds of 1000, 1200 and 1600 rpm respectively. By quantifying the deflection of the membrane, I found that the deflection percentage is linear with the applied pressure for a given PDMS membrane thickness (**Figure 3-5D**). When the PDMS membrane thickness is reduced by increasing spin-coating speed, I found a larger deflection at the same applied pressure. Both of these results agree with a mechanical intuition of plate deflection.

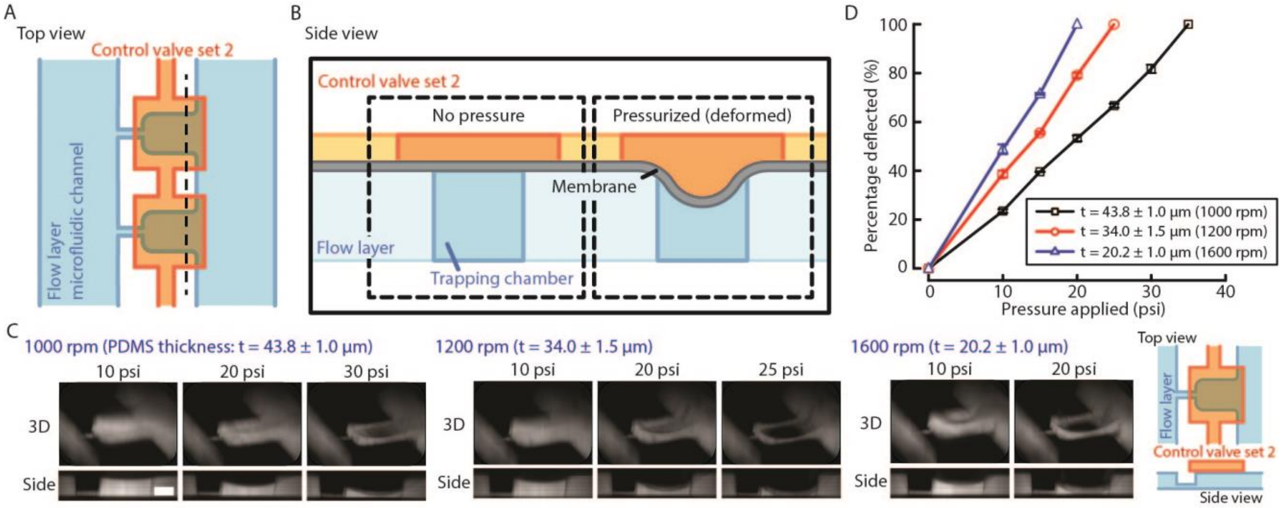

Figure 3-5: Deflection characterization of PDMS membrane by pressurizing control layer 2
(A) Top view: Control valve set 2 is aligned with the trapping chambers in microfluidic channel. (B) Side view: Air pressure in Control valve set 2 is regulated by a pressure regulator. At zero pressure, the membrane between Control valve set 2 and microfluidic channel is flat. When Control valve set 2 is pressurized, the membrane deflects. (C) Images from confocal microscopy of fluorescent dye perfused in the microfluidic channel. Z-stack images were reconstructed in ImageJ to generate 3D and side view images. The deflections of PDMS membrane with different spin-coating speed under different applied pressure are shown, scale bar = 50 μm. (D) The percent deflection of the PDMS membrane as a function of different PDMS spin-coating speed and applied pressure (n = 4). The PDMS membrane thickness t (mean ± SEM) was measured for each spin-coating speed.

To identify the ideal spinning speed and membrane thickness for the microfluidic device, I considered two criteria, which were the strength of PDMS bonding and the strength of the membrane from rupturing. Although the PDMS substrates were oxygen-plasma treated before being bonded together, a high enough air pressure could break the PDMS bonding, leading to a blockage of the microfluidic channel. Therefore, a thinner membrane was preferable under this consideration because thinner PDMS membrane completely blocked the microfluidic channel at a lower applied pressure. However, when the PDMS membrane was too thin, the device fabrication process became more challenging due to bonding issues. Based on these considerations, I fabricated and worked with microfluidic devices with a 1200 rpm PDMS spinning speed on the flow layer silicon mold, from which the membrane deflects and completely blocks the flow channel at 25 psi.

3.5.2 Trapping of double emulsions

Double emulsions were trapped inside the microfluidic device for the application of mechanical forces. Double emulsions with a diameter between 40 μm and 90 μm were first generated in a glass capillary microfluidic device (**Figure 3-3**) and then reinjected into the microfluidic device at 10x dilution. To trap double emulsions in the trapping chambers, Control valve set 1 was then pressurized at 10-15 psi to block the main microfluidic channel, which increased the flow resistance in the main microfluidic channel. As a result, the flow resistance ratio between the microchannels and the main microfluidic channel will reduce and more fluid streamline will go through the microchannels. This greatly increases the trapping efficiency of the double emulsions and I typically find all 14 trapping chambers filled up within a minute. A double emulsion will be trapped if the radius of the double emulsion is smaller than the instantaneous critical stream width, which is dictated by flow resistance ratio between the micropipettes and main microfluidic channel [153]. Therefore, a double emulsion with larger diameter is usually more difficult to trap; however, with actuation of Control valve set 1, the microfluidic device successfully trapped double emulsions of 46, 68 and 90 μm in diameter, as shown in **Figure 3-6A**.

3.5.3 Reversible compression of double emulsions

After demonstrated successful trapping of double emulsions, I next evaluated the effect of compression on double emulsions. Control valve set 2 was designed to compress double emulsions inside the trapping chambers. Due to the fluid properties of the inner aqueous and middle oil phases, double emulsions deform easily when they experience different external flow fields [154, 155]. But when the external load is removed, double emulsions return to their original spherical shapes due to interfacial tension. When I increased the applied pressure in Control valve set 2 and compressed the trapped double emulsions, the middle oil phase in-plane thickness increased. Double emulsions of 50 and 80 μm in diameter were compressed using an air pressure up to 20 and 15 psi respectively (**Figure 3-6B**). At 20 psi air pressure, the 80 μm double emulsions escaped from the trapping chambers due to the confined space inside the trapping chambers and their larger sizes. For both sized double emulsions, compression changed their shape and oil thickness. **Figure 3-6C** shows the increase in average in-plane thickness of the middle oil phase with increasing applied pressure. The double emulsions with outer diameter of 50 μm had a 3.8 fold increase in middle phase thickness, while a 2.3 fold increase was observed for 80 μm double emulsions. The change in average in-plane thickness of the middle oil phase was

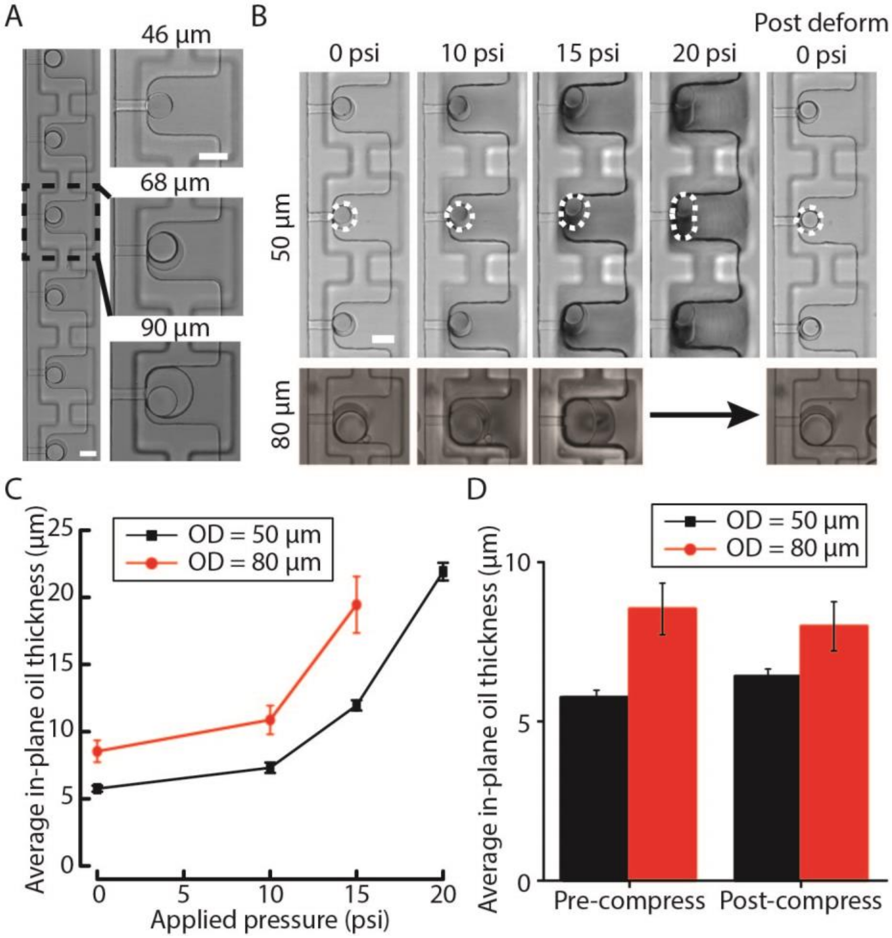

Figure 3-6: Trapping and compression of double emulsions inside trapping chambers

(A) Double emulsions of different sizes were trapped in the trapping chambers, scale bar = 50 µm. (B) Double emulsions trapped inside trapping chambers were deformed at different applied air pressures on Control valve set 2. The double emulsion droplets were squashed upon compression and returned back to spherical shape after compression. (C) The changes in average in-plane thickness of the middle oil phase as a function of applied pressure for two different sized droplets (n = 3, mean ± SEM). Average in-plane thickness is calculated by averaging the largest thickness and the smallest thickness of the double emulsion. (D) The average in-plane thickness of the middle oil phase for two different sized droplets before and after compression (n = 3, mean ± SEM).

completely reversible when pressure was reduced back to 0 psi after compression (**Figure 3-6D**). Together these results showed the capability of the microfluidic device to compress double emulsions to increase their middle oil phase thickness.

3.5.4 Oil removal by aspiration of double emulsions

Double emulsions are very stable and oil must be removed in order to thin out the oil phase. I postulated that aspiration of the middle oil phase could result in permanent thinning of the oil phase. Aspiration is achieved with the same mechanism used in μFPA device previously [46]. The pressure difference across the microchannel comes from the pressure drop through the main microfluidic channel due to fluid flow (**Figure 3-7A**), which is the product of the volume flow rate and flow resistance of the main microfluidic channel. To determine the relationship between flow rate and pressure difference for each trapping chamber for the relatively complex microfluidic channel design, I performed flow simulation of the flow channel using COMSOL. As shown in **Figure 3-7B**, the pressure difference is linear with the flow rate for each trapping chamber, with the largest pressure difference for the most upstream trapping chamber.

To test the effect of aspiration on double emulsions, I encapsulated rhodamine succinimidyl dye in 80 μm double emulsions that had an average in-plane oil thickness of 8.2 μm. By increasing the flow rate, I aspirated on double emulsions and observed several behaviors through dynamic changes of aspiration pressure, as shown in **Figure 3-7C**. At low aspiration pressures of 8.5 or 21.3 Pa, oil was aspirated into the micropipette. Interestingly, when the pressure difference increased from 34.6 to 69.3 Pa, oil began to pinch off and the middle phase thinned out over several seconds. The transition of oil aspiration to pinching off occurs when the protrusion length of the double emulsion is larger than the hydraulic radius of the aspiration micropipette. After applying a high pressure difference to the double emulsions for several seconds (69.3 Pa, >5.8 s), the oil in the double emulsion became nearly invisible by bright field imaging. However, there is

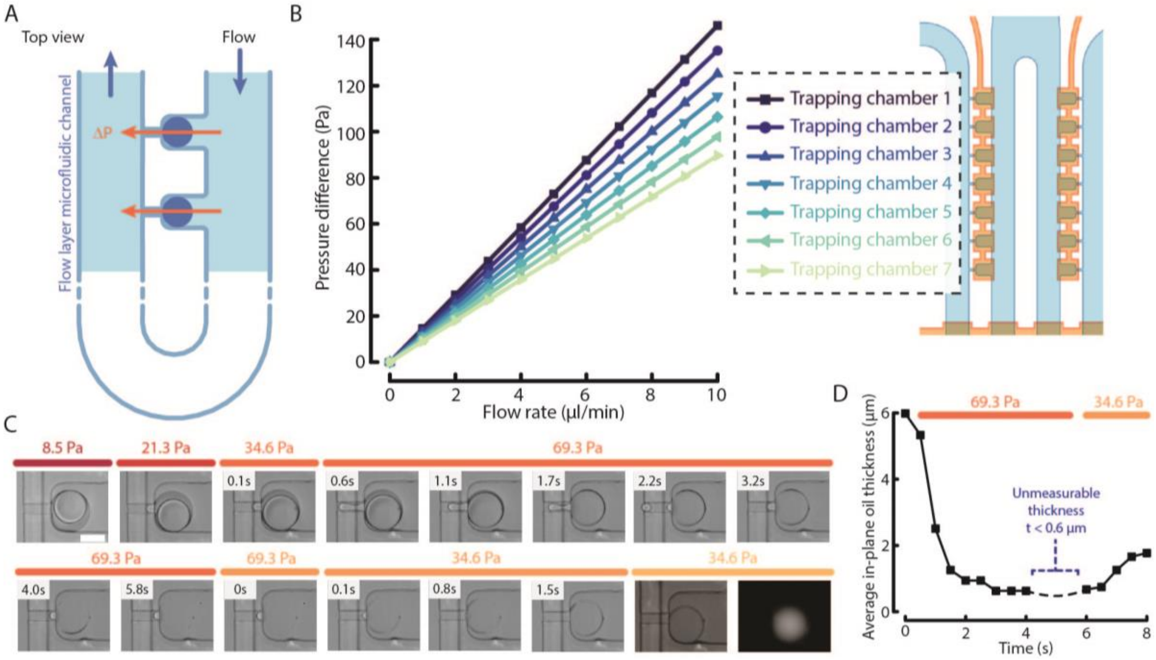

Figure 3-7: Thinning of the middle phase in double emulsion droplets by aspiration (A) The flow layer microfluidic channel is designed such that trapped droplets in the trapping chambers experience a pressure difference induced by fluid flow in the microfluidic channel. (B) The relationship between flow rate and pressure difference at different trapping chamber position was obtained from COMSOL simulation. (C) A double emulsion droplet trapped in the trapping chamber was aspirated by changing the pressure difference. As the pressure difference increased, the oil changed from being aspirated to pinching off and thinning out. When the pressure difference was reduced, the oil retracted. After the thinning of oil, the double emulsion remained inside the trapping cup and the initially encapsulated fluorescent dye remained in the double emulsion. (D) The change in average in-plane thickness of the middle oil phase with respect to time for the same double emulsion shown in (C) at a pressure difference of 69.3 and 34.3 Pa.

some residual oil remained inside the micropipette channel. When the pressure difference was reduced back to 34.6 Pa, the oil retracted from the micropipette channel and refilled the double emulsion middle phase (34.6 Pa, 1.5 s). The double emulsion remained stably trapped after thinning of the oil phase, as evident by the intact encapsulated fluorescent dye in the aqueous inner phase. The average in-plane thickness of the middle oil phase of this single double emulsion was measured at aspiration pressure differences of 69.3 and

34.6 Pa (**Figure 3-7D**). This experiment demonstrated that the middle oil phase can be thinned out permanently by aspiration in the microfluidic device.

3.5.5 Mechanically activated double emulsion through aspiration and osmotic shock facilitates calcium transport through oil

Through compression and aspiration, the microfluidic device enables temporary thickening and permanent thinning of the middle oil phase in double emulsions. The middle oil phase in a double emulsion behaves like a semi-permeable membrane through which solute molecules can diffuse into and out of the inner aqueous phase. This is especially relevant in drug delivery application, where non-ionized hydrophobic drug diffuses through the oil obeying Fick's law of diffusion. Since ions are hydrophilic, they cannot diffuse through oil easily. However, in the presence of an osmotic pressure difference during hypo-osmotic shock, it has been observed that ions can also transport along with water through Span80 stabilized oil phase of double emulsions via two different mechanisms [156]. When there is no contact between the two interfaces, reverse micelles form by lipophilic surfactant molecules and diffuse through the oil, while transport of water is carried by single hydrated surfactant molecules when there is contact between the two interfaces [156-158]. The ion transport was also found to be dependent on the oil-soluble surfactant [156]. Fluorinated oil (HFE-7500) with fluorosurfactants (PFPE-PEG) used to generate double emulsions in this study has been shown to provide permeability to oxygen and other non-ionized small molecules [159, 160]. However, the transport of ions through this oil is not known. Thus, I investigated ion transport through the middle oil phase as a biological response that involves mechanically perturbing double emulsions.

In order to detect transport of calcium ions during osmotic downshock, I encapsulated Rhod-2 calcium indicator in double emulsions (**Figure 3-8A**). I did not find a significant change in fluorescence when I subject thick double emulsions with hypo-

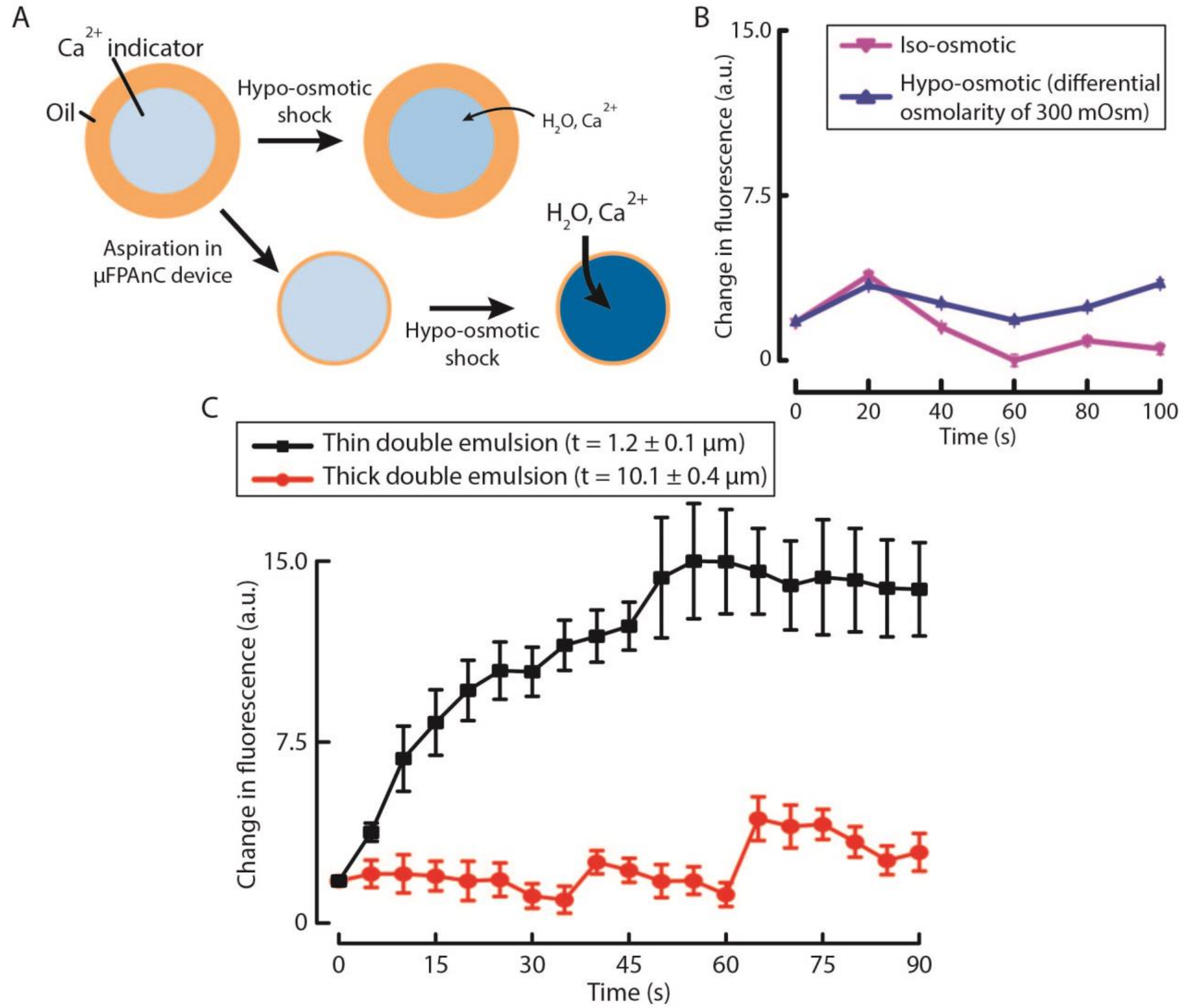

Figure 3-8: Mechanically activated artificial cell through aspiration and osmotic shock facilitates calcium ion transport through oil
(A) Thick double emulsions are aspirated in the microfluidic pipette array and compression (µFPAnC) device to form thinner double emulsions. Both thick and thin double emulsions are hypo-osmotically shocked, such that calcium ions diffuse through the oil and enter the double emulsions. (B) The changes in fluorescence level as a function of time for thick double emulsions (Thickness = mean ± S.E.: t = 10.7 ± 0.1 µm) in iso- and hypo-osmotic solution. (n = 10). (C) The changes in fluorescence as a function of time for thick and thin double emulsions (n = 12, mean ± SEM).

osmotic shock (**Figure 3-8B**). However, when I aspirated the double emulsions to permanently thin out the oil, calcium ions entered the double emulsions rapidly as indicated by the increase in fluorescence for the calcium indicator (**Figure 3-8C**). By comparison, unaspirated double emulsions that had a thicker middle phase did not have increased fluorescence during osmotic downshock over the same period. This indicates that by aspirating double emulsions using the microfluidic device, calcium ions in the outer phase entered the double emulsions faster. The transport of ions through the fluorinated oil of this emulsion system behaved differently when compared to that through hexadecane with Span80 [156]. Nevertheless, I demonstrated mechanical activation of double emulsion artificial cell with influx of calcium ions.

3.6 Conclusions

In this work, I have developed a microfluidic device, which combines microvalves with the previously developed μFPA device in the lab to uncouple trapping from aspiration and to exert compression. The device contains a flow channel for aspiration and a control layer for trapping and compression. By connecting a syringe pump to the flow channel and a regulated pressurized air to the control layer, the device is able to trap artificial cells in designated compression and aspiration chambers with high trapping efficiency and exert compression and aspiration.

I successfully demonstrated mechanically activated artificial cell using this newly designed microfluidic device. The prototype of artificial cell is a double emulsion with oil separating the inner and outer aqueous phases. I showed that I can regulate oil thickness by compression and aspiration as a way to mechanically regulate transport process in artificial cells. This represents the first demonstration to couple a mechanical input to a biochemical output in double emulsion as an artificial cell. I envision testing the possibility of mechanically regulating gene expression in artificial cells encapsulating cell free system as a future direction. This work also highlights the power and utility of microfluidic devices in synthetic biology research. Although the mechanosensitive artificial cell is quite primitive at this point, it is a starting point for further engineering. All life forms are mechanosensitive, as mechanical force influences biochemistry [161], and this work opens up exciting opportunities in force-activated synthetic biology.

Chapter 4: Improvement of a microfluidic compression device for cell mechanics study

4.1 Introduction

4.1.1 Mechanobiology and microfluidics

Cells in our body experience a myriad of mechanical stimuli over their lifetime. Mechanotransduction underlies cellular responses to different mechanical stimuli. The proper responses of the cells to any mechanical stimuli are important in maintaining the survival of a multicellular organism. Mechanical stimuli can be classified into either passive or active mechanical input [14]. Passive inputs are physical properties of the environment, while active inputs are mechanical forces that act directly on cells. With the development of microsystem engineering tools, controlled and repeatable application of passive or active mechanical input to single cells is becoming more available [162]. Several microfluidic platforms have been developed for mechanotransduction research over the last decade,[43, 162] which includes the application of shear stress [44, 163, 164], stretching [45, 165], and compression[82-84] to a population of cells or a single cell. In recent years, mechanotransduction by compression is gaining more interest, with recognition that cells in our body such as fibroblasts, osteocytes, and cancer cells experience compression [166-168].

4.1.2 Microengineering tools for compression

The study of mechanobiology in cell population and single-cell contexts offer different insights in mechanical responses from being physiologically relevant to single-cell heterogeneity. Different experimental techniques were developed for these studies [19]. To understand the heterogeneous mechanical responses of single cells to compression, modified atomic force microscopy (AFM) probes was developed to apply compressive forces to single cells [78, 79, 169, 170]. Lulevich *et al.* developed an atomic force microscopy based single-cell compression technique to measure the force and deformation of living cells in 2006 [78]. They also extended the technique to investigate the rigidity of neuronal cells under Aβ42 protein treatment [169] and the stiffness of keratinocyte cells [170]. Weafer *et al.* also used a modified AFM system to perform whole cell compression of osteoblasts to study the role of cytoskeleton in compression resistance of cells [79]. While AFM is a powerful approach to apply compressive forces and measure deformation of cells, this sophisticated method has a low throughput and requires an expensive equipment and technical expertise. Development of new microengineered tools that combine dynamic compression and other modes of deformation in a higher throughput manner would be very desirable for mechanotransduction research.

Microfluidic devices have been extensively used in high throughput single cell analysis applications to precisely manipulate cells and their surrounding microenvironment. In the early 2000s, Quake's lab developed multilayer soft lithography to build active microfluidic systems containing on-off valves and switching valves [81]. They further developed the system to fit thousands of micromechanical valves and hundreds of individually addressable chambers inside a microfluidic chip [171]. With the integration of microsized and fast-operating valves in the microfluidic system, several platforms have been developed for studying the biological response of cells under a compressive stress [82-84]. Kim *et al.* used a microfluidic biomechanical device formed by multilayer soft lithography for compressive stimulation and lysis of cells [82]. Hosmane *et al.* developed a new platform that compressed locally and induced injury to micron-scale segments of single axons [83]. Si *et al.* used a similar multilayer soft lithography device and found that compressed *E. coli* grow and divide with a flat pancake-like geometry [84]. These studies took advantage of the high throughput nature of multilayer microfluidic devices. However, microfluidic platforms integrated with microvalves have not been developed for single cell compression.

4.1.3 Improvement of the microfluidic compression device

Previously, a microfluidic aspiration and compression device was developed to apply compression to single artificial cells for mechanical activation [172]. However, the device had several limitations in compressing cells, which spread on the surface and are smaller in size. The concave deflection profile of the PDMS membrane limited the ability to have a controlled contact area between the membrane and the cells (**Figure 4-1A**), affecting the forces applied to each cell. Moreover, cells randomly spread inside the microfluidic device and were rarely directly underneath the deflection membrane for compression (**Figure 4-1B**). These limitations motivated me to further improve the microfluidic device in order to achieve single cell compression.

The goal of this chapter is to engineer a more versatile microfluidic platform for mechanobiology research. I modified the design of the previous microfluidic device to

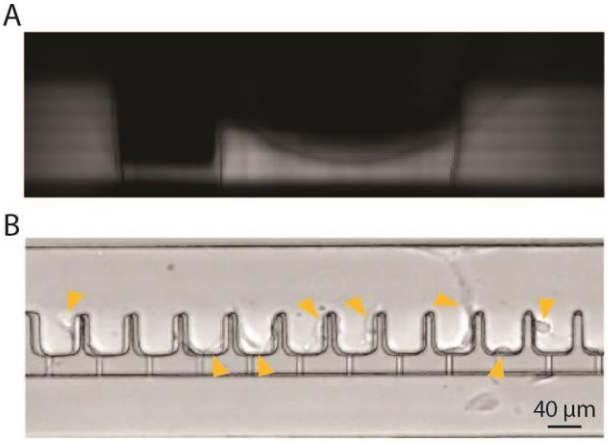

Figure 4-1: Limitations in previous microfluidic compression device for compression of cells
(A) Image from confocal microscopy of fluorescent dye perfused in the microfluidic channel. Z-stack images were reconstructed in ImageJ to generate side view images.
(B) Brightfield image showed the random spreading of cells inside the microfluidic device, as pointed out by the arrowhead.

apply more a uniform compressive force to single cells. I will first describe the modification of design, followed by the characterization of the device. Finally, I will describe cellular relaxation to static and cyclic compression. Overall, the newly designed microfluidic device provides a platform for applying static or cyclic compression on single cells.

4.2 Microfluidic device overview and design

To eliminate the concave deflection profile of the membrane, I spatially varied the thickness of the membrane to create a difference in bending rigidity across the membrane, since bending rigidity depends on the elastic modulus of the membrane and the membrane thickness. While it is not easy to fabricate a device with different elastic modulus in the membrane, I decided to include a block of PDMS to change the thickness of the membrane in the middle of the membrane (**Figure 4-2**). In this case, the membrane in the middle will have a higher resistance to deform comparing to the membrane on the side. This, then,

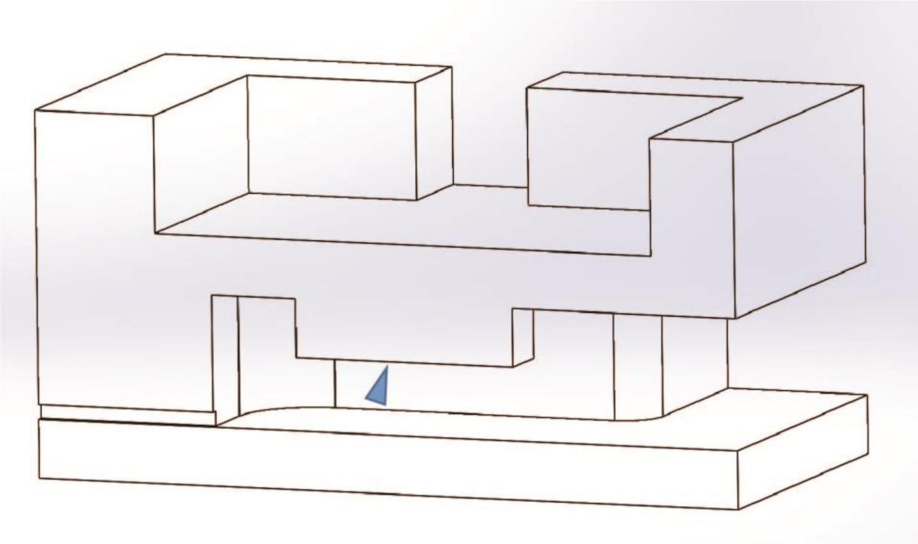

Figure 4-2: Modification of the thickness in the middle of the membrane
The thickness of the membrane was designed to be larger in the middle comparing to the side. This creates a difference in bending rigidity throughout the membrane.

could create a flat deflection profile in the middle of the membrane, while having a concave deflection profile on the side.

To avoid random spreading of cells inside the microfluidic device, I modified the device fabrication procedures so that multiple fibronectin islands could be printed underneath the deflection membrane, where cells will only be able to spread on the fibronectin islands.

The modified microfluidic device, made out of polydimethylsiloxane (PDMS), has two layers, the flow layer (blue) and the control layer (orange) (**Figure 4-3A**), similar to the previously designed microfluidic device [172]. The flow layer has a similar design, where fluid and cells flow from two inlets through the microfluidic channel to one outlet. An extra inlet was added to allow quicker and easier fluid exchange for different biological assays. The microfluidic channel first splits into two channels, each containing 18 compression chambers. Each compression chamber is connected to the opposing end of the

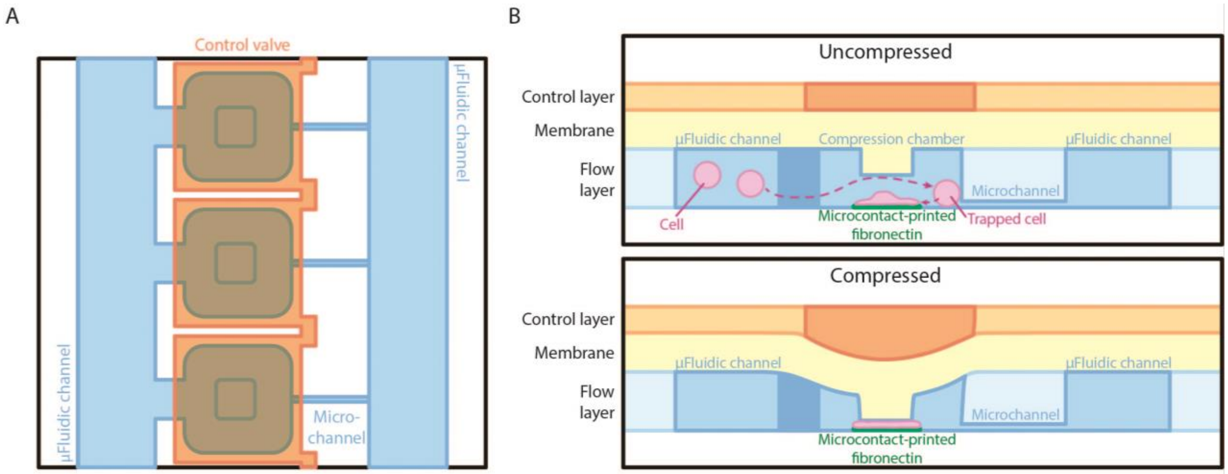

Figure 4-3: Schematic showing the design of the microfluidic device
(A) Top view of the flow layer and control layer design at the compression chamber. Rectangular block was added to the design for achieving a more uniform deflection.
(B) Side view of the microfluidic device when the control layer was uncompressed (top) and compressed (bottom). Fibronectin patterns were microcontact-printed underneath the block inside the compression chamber to control the positions where cells spread.

main microfluidic channel through a small microchannel. The microfluidic channel was designed so that the flow resistance of the main microfluidic channel is 20 times smaller than that of the small microchannel. This allows the majority of fluid to flow into the main microfluidic channel. A thin PDMS membrane separates the microfluidic channel and the control layers that serves two different functions and are independently controlled. Two pneumatically controlled valve sets located above the main microfluidic channel and above the compression chambers were used to direct flow to the compression chambers and to compress cells respectively.

To apply a uniform compressive force on cells, fibronectin was microncontact-printed underneath the block that was designed to be at the center of the compression chamber (**Figure 4-3A, B**). When cells were loaded into the device, the cells would be trapped inside the compression chambers, due to the pressure difference across the microchannel. After a cell spreads on the fibronectin pattern, it can then be compressed by increasing the pressure in the control layer that deflects the membrane (**Figure 4-3B**).

4.3 Materials and methods

4.3.1 Membrane deflection simulation

Membrane deflection in the compression chamber of the microfluidic device was simulated using COMSOL 4.4 (COMSOL Multiphysics). The membrane and the block in the compression chamber can be simplified and characterized by block width, compression chamber width, block thickness and membrane thickness. To determine the optimal design of the device, a simplified three-dimensional model of the membrane and block was constructed in COMSOL and was simulated using the solid mechanics module. The PDMS was modeled as a linear elastic material with elastic modulus of 0.3 MPa, a Poisson's ratio of 0.49 and a density of 970 kg/m^3. A uniform pressure of 10 psi was applied as boundary load on top of the membrane, while the four sides of the membrane were set as fixed.

For the demonstration that the membrane and the block will deflect as predicted, a three-dimensional model of the device was also constructed in Solidworks with the block width as 40 μm, the compression chamber width as 80 μm, the block thickness as 20 μm and the membrane thickness as 30 μm. The deflection of the membrane and the block was simulated using COMSOL 4.4 as well with the same simulation module, material properties and pressure applied.

4.3.2 Device fabrication

The microfluidic device was fabricated using multilayer soft lithography technique [149]. The microfluidic device is composed of a PDMS control layer, a PDMS flow layer and a fibronectin printed glass coverslip, of which were aligned and bonded permanently together. Schematic of the fabrication process flow of the microfluidic device is illustrated in **Figure 4-4**.

Three photomasks were produced by high resolution inkjet printing on transparency film (CAD/Art Services) for SU-8 patterning of four silicon molds by standard photolithography. The first silicon mold is composed of one layer of SU-8 pattern for PDMS casting of the control layer. The SU-8 pattern of the control layer defined two sets of integrated microfluidic control valves for closing of the main microfluidic channel (Control valve set 1) and deflection of the flow layer in the trapping chambers for planer compression of cells (Control valve set 2) respectively. These two sets of microfluidic control valves contained two independent inlets. The second silicon mold is composed of three layers of SU-8 patterns to be used for PDMS spin-coating of the flow layer. The first SU-8 patterning layer defined the side microfluidic pipette channel for trapping the cells. The second SU-8 patterning layer defined the compression block for flat planar compression of cells. The third SU-8 patterning layer defined the main microfluidic channel, the trapping chambers, the inlets and the outlet. The third silicon mold is composed of one layer of SU-8 pattern for PDMS casting of the bottom alignment layer. The SU-8 pattern of the bottom alignment layer has the same design as the third SU-8 patterning layer of the second silicon mold, so that the bottom alignment layer can be used for aligning the fibronectin and the PDMS control/flow substrate. The fourth silicon mold is

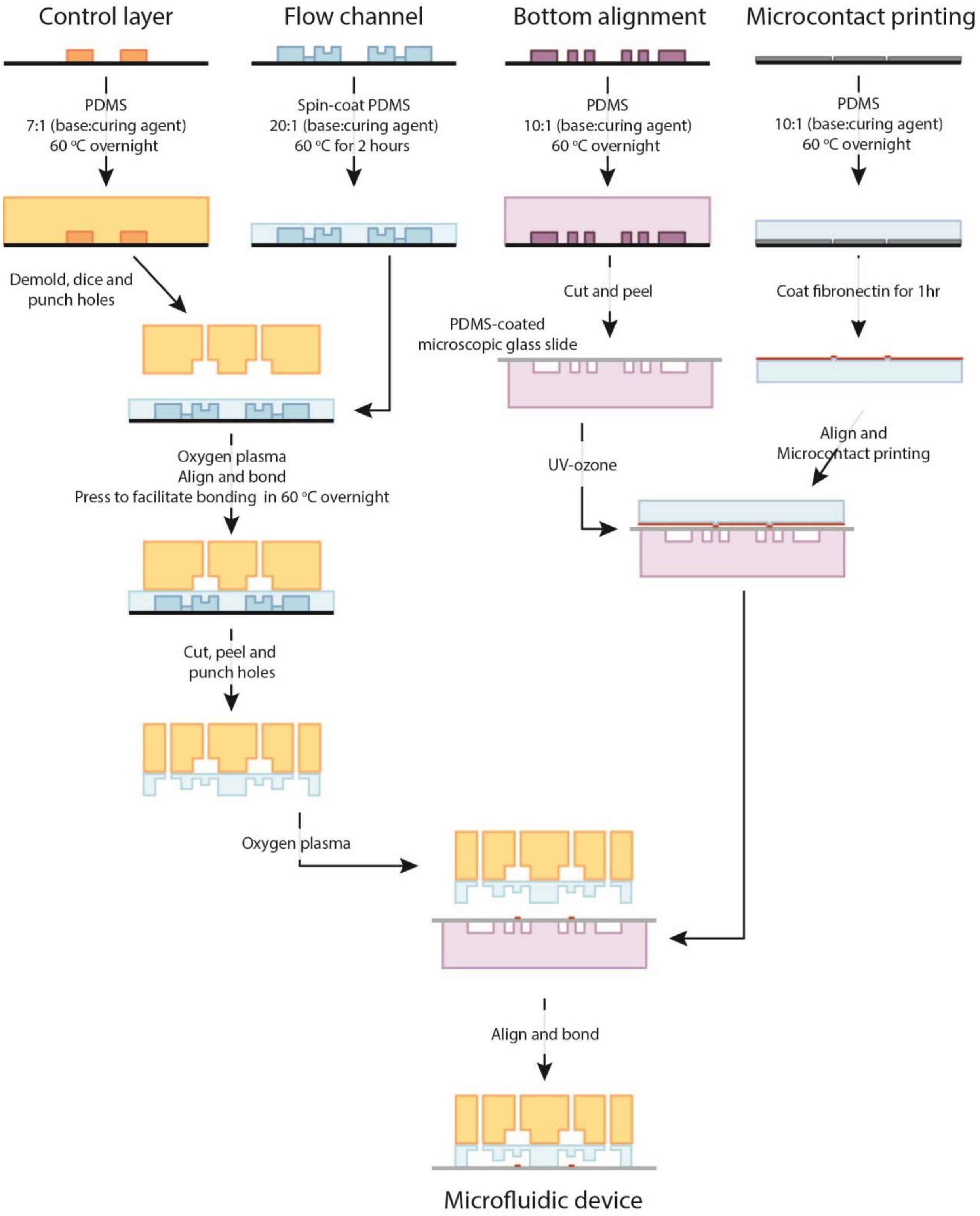

Figure 4-4: Fabrication process of microfluidic device
Four silicon molds for control layer, flow channel, bottom alignment layer and microcontact printing layer were casted with PDMS, demolded, cut, aligned, bonded, surface treated at different stages as shown in the figure.

composed of one layer of SU-8 pattern for PDMS casting of the microcontact printing layer. The microcontact printing layer has different shape and size for printing fibronectin right underneath the compression chambers.

The SU-8 patterning procedures of the four silicon molds followed the standard protocol developed by Microchem, Inc. for SU-8 2000 [150]. First, four silicon wafers were dehydrated on a hotplate at 200°C for 15 min to promote photoresist adhesion. In SU-8 patterning the silicon mold for the control layer, SU-8 2025 was spin-coated at 4000 rpm onto the wafer for 30 s, which gave a thickness of 20 μm. The photoresist was then exposed to UV light for 12 s under a contact aligner (Karl Suss, MJB45). In the first SU-8 patterning of the flow layer, SU-8 2005 was spin-coated at 2700 rpm onto the silicon wafer for 30 s, which gave a thickness of 5.4 μm. The photoresist was then exposed to UV light for 9 s with the first flow channel photomask, which defined the side pipette arrays. After development of first SU-8 layer, the silicon wafer was hard-baked at 200°C for 20-30 minutes to consolidate the developed SU-8 patterns before the application of the second SU-8 layer. Subsequently, for the second layer SU-8 patterning of the flow layer, SU-8 2025 was spin-coated at 3500 rpm onto the silicon wafer for 30 s, which gave a combined thickness of 24 μm. The photoresist was then aligned with the second flow channel photomask, which mainly defined the compression block, and exposed to UV light for 11.5 s. After development of SU-8, both silicon molds were hard-baked at 200°C for 20-30 minutes to consolidate the developed SU-8 patterns before the application of the third SU-8 layer. Subsequently, for the third layer SU-8 patterning of the flow layer, SU-8 2025 was spin-coated at 2100 rpm onto the silicon wafer for 30 s, which gave a combined thickness of 38 μm. The photoresist was then aligned with the third flow channel photomask, which mainly defined the main microfluidic channel, and exposed to UV light for 12.5 s. In SU-8 patterning the silicon mold for the bottom alignment layer, SU-8 2010 was spin-coated at 2000 rpm onto the wafer for 30 s, which gave a thickness of 13 μm. The photoresist was then exposed to UV light for 9 s under a contact aligner. In SU-8 patterning the silicon mold for the microcontact printing layer, SU-8 2025 was spin-coated at 4000 rpm onto the wafer for 30 s, which gave a thickness of 20 μm. The photoresist was then exposed to UV light for 12 s under a contact aligner. After development of SU-8, all four silicon molds were hard-baked at 200^{o}C for 20-30 minutes again to cure any surface cracks. The thicknesses of both the control layer and flow channel SU-8 pattern were measured using a stylus profilometer (Dektak 6M).

Before PDMS casting or spin-coating on the silicon molds, all four wafers were first silanized with trichloro(1H,1H,2H,2H-perfluorooctyl)silane (Sigma-Aldrich) in a desiccator for 1 hour. The silicon mold for the control layer was casted with PDMS (Sylgard-184) with a mixing ratio of 7:1 (base:curing agent), while both the silicon mold for the bottom alignment layer and the microcontact printing layer were casted with PDMS with a mixing ratio of 10:1. After degassing in a desiccator, the control layer, bottom alignment layer and microcontact printing layer PDMS substrate were then cured at 60^{o}C overnight before demolding from the wafer. The control layer PDMS substrate was then diced and holes were punched with 1 mm diameter at the inlets of the microfluidic control valves, while the bottom alignment layer and microcontact printing layer PDMS substrates were also diced. The flow channel membrane was generated by spin-coating PDMS with a mixing ratio of 20:1 (base:curing agent) on the flow layer silicon mold at rotational speeds 1200 rpm for 60 s. After this, the PDMS flow layer membrane was cured at 60^{o}C for 2 hours. Both the diced PDMS control substrate and the PDMS flow layer membrane on the silicon mold were placed in an oxygen plasma etcher (Femto, Covance) to render the PDMS surfaces hydrophilic for the preparation of bonding procedure described as follows. The flow layer silicon mold containing the PDMS membrane was mounted on a customized alignment platform on an optical microscope. The diced PDMS control layer substrate was then carefully aligned and bonded with the PDMS flow layer membrane. The permanent bonding between the control layer substrate and PDMS flow layer membrane was established by heating in the oven at 60^{o}C overnight with the aid of gentle pressing between two substrates.

The day after, the bonded control layer substrate with the flow layer membrane was then cut out and peeled off from the flow layer silicon wafer. Inlet and outlet holes (1 mm diameter) for the main microfluidic flow channel were punched through the layer PDMS control/flow substrate. The bottom alignment substrate which had the similar channel of flow layer was used to align the fibronectin with flow layer. First, PDMS microcontact printed substrate was aligned with the bottom alignment substrate to print the fibronectin on a PDMS-coated glass coverslip. Then the PDMS microcontact printed substrate was removed. Immediately, the PDMS control/flow substrate was placed in an oxygen plasma etcher to render PDMS surface hydrophilic before aligning with the bottom alignment substrate and permanently bonding to the fibronectin-printed glass coverslip. The device was then kept in 4^{o}C until use.

4.3.3 Microcontact printing

We incubated 40 μg/ml fibronectin on the PDMS stamp for 1 hour to coat fibronectin on its surface. A PDMS-coated coverslip was oxidized by UV-ozone. The bottom alignment substrate would be placed under a PDMS-coated coverslip and aligned with a fibronectin-coated PDMS stamp. The fibronectin is printed onto the PDMS-coated coverslip when the pattern comes into conformal contact with it. We used a mixture of fibrinogen conjugated with Alexa Fluor 647 (ThermoFisher Scientific, F35200) and fibronectin and checked the positions of fibronectin island using a spinning disk confocal microscope (Olympus IX73 with Yokogawa CSU-X1). The device was washed with 0.1% Pluronic F127 solution for 1 hour to passivate the remaining surface and then washed with PBS for 1 hour.

4.3.4 Visualization of flow streamlines.

1 μm Y (yellow)-G (green) fluorescent beads (Invitrogen; 1:1000 dilution in DI water) were introduced into the device at a flow rate of 1 μl/min and were imaged with a high exposure time to observe the flow streamlines. The PDMS microfluidic device was perfused with DI water first to eliminate any trapped air bubbles before use. Fluorescence images were captured using an epi-fluorescence microscope (Nikon, Ti Eclipse) with 500 ms exposure time to generate streamlines to show the trajectory of the traveling fluid.

4.3.5 Imaging membrane deflection and 3D image reconstruction.

Rhodamine succinimidyl dye was perfused into the device and we made sure there was no air bubble inside. A spinning disk confocal microscope (Olympus IX73 with

Yokogawa CSU-X1) was used for imaging the dye solution at 20X. The control layer inlets (Control valve set 2) of the microfluidic device was connected to a pressure regulator (Norgren R07-200-RGEA). The membranes above the chambers were deflected by changing the air pressure in the Control valve set 2 between 0 psi-30 psi. A z-series of fluorescence images, excited at 561 nm, was captured at a step size of 500 nm and was reconstructed in ImageJ to generate 3D and side view images.

4.3.6 Preparation of cell lines.

Non-tumorigenic epithelial cell MCF-10A cells were cultured in growth media DMEM premixed 1:1 with Ham's F12 nutrient mixture with 5% horse serum, 1% pen-strep, 2.5 μg/ml amphotericin B (fungizone), 5 μg/ml gentamycin, 10 μg/ml insulin, 0.5 μg/ml hydrocortisone, 0.02 μg/ml epidermal growth factor, and 0.1 μg/ml cholera toxin at 5% CO_2 and 37°C until about 70% confluency. 5 μg/ml Hoechst dye in PBS was used to label the nucleus. Stable cell lines expressing eGFP and Lifeact-RFP were generated via lentiviral transduction for labeling the cell volume and actin respectively. Cells were suspended at 10^6 cells/ml to minimize cell clumping and possible pressure fluctuation during the experiment.

4.3.7 Cell trapping, seeding and compression.

The PDMS microfluidic device was perfused with warm medium before MCF-10A cells with a concentration of 10^6 cells/ml were introduced into device for trapping single cells. To trap cells in the trapping chambers, Control valve set 1 was then pressurized at 20-30 psi to block the main microfluidic channel, which increased the flow resistance in the main microfluidic channel. After the cells were trapped, the device was placed in an incubator for 4 hours to allow cell attachment and spreading on the fibronectin-patterned surface. An electro-regulator (Proportion-Air, QBX) was set up, which was connected to a pressure regulator, and a computer program was used to control the pressure. Pressure from 0 psi to 15 psi was applied to the control layer that deflected the membrane for cell compression. Each pressure was maintained for 3 minutes and z-series of fluorescence images were acquired at excitations of 488 nm, 561 nm, and 405 nm with 500 ms exposure time, at a step size of 500 nm. For cyclic compression, the cells were compressed at 0.5 Hz for 6 minutes.

4.4 Results and discussion

4.4.1 Cell size and height

In order to design a device that is best suited for compressing MCF-10A cells, we first measured MCF-10A cell size and height in suspension and attached on a surface. Z-stack fluorescence confocal images were taken using a spinning disk confocal microscope (Olympus IX73 with Yokogawa CSU-X1) and were reconstructed in ImageJ to generate side view images (**Figure 4-5A, B**). MCF-10A cells in suspension have an average height of 18.8 μm, while attached MCF-10A cells have an average height of 14.1 μm (**Figure 4-5C**). By looking at the top view of the attached MCF-10A cells, they spread across a distance of 20-40 μm (data not shown). The size and height of free or attached MCF-10A cells provide a guidance for determining the geometric parameters of the device.

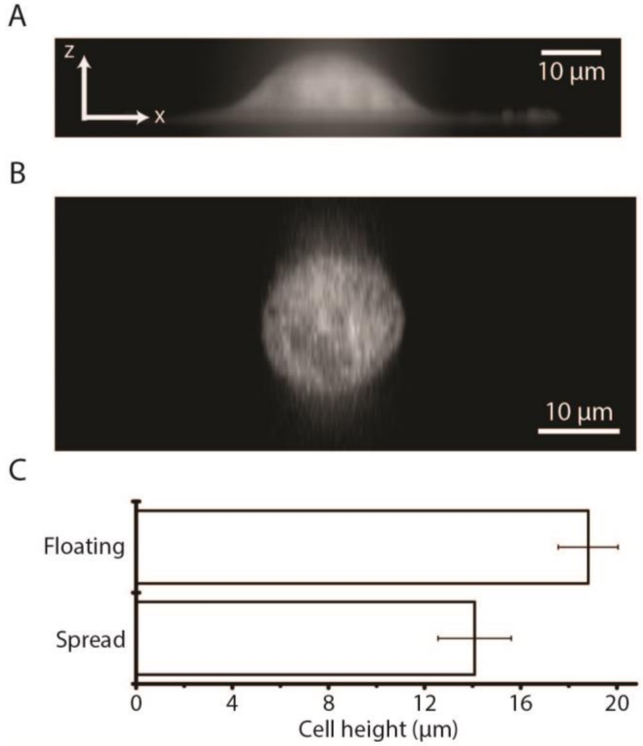

Figure 4-5: MCF-10A cell side view and height in suspension and attached on a surface
(A) Side view fluorescence image of MCF-10A cell attached on a surface. (B) Side view fluorescence image of MCF-10A cell in suspension. (C) The average height of MCF-10A cells when floating or spread on a surface.

4.4.2 Geometric parameters of the device for cell compression

Four different geometric parameters of the compression chamber need to be determined for designing the device to apply uniform compression on MCF-10A cells. The membrane and the block in the compression chamber can be simplified and characterized by block width, compression chamber width (w), block thickness (h_b) and membrane thickness (h_m) (**Figure 4-6A**). Since the MCF-10A cells have a spreading area of 20-40 µm, the block width was set as 40 µm to ensure that the cells are spread underneath the block even there is some misalignment during device fabrication. The separation between the block and the bottom cell attachment surface was set to be around 20-25 µm because of the MCF-10A cells when they are in suspension. While the height of the MCF-10A cells is around 14 μm when they spread, I chose the optimal membrane deflection to be around 10-15 μm when a pressure of 10 psi is applied.

To determine the other three parameters for optimal compression, I performed solid mechanics simulation of a simplified membrane and block model using COMSOL. The displacement of the block was determined for the 27 conditions where we permutated the values of the three variables (**Figure 4-6B**). Based on the simulation results, the compression chamber width and membrane thickness were set as 80 μm and 30 μm

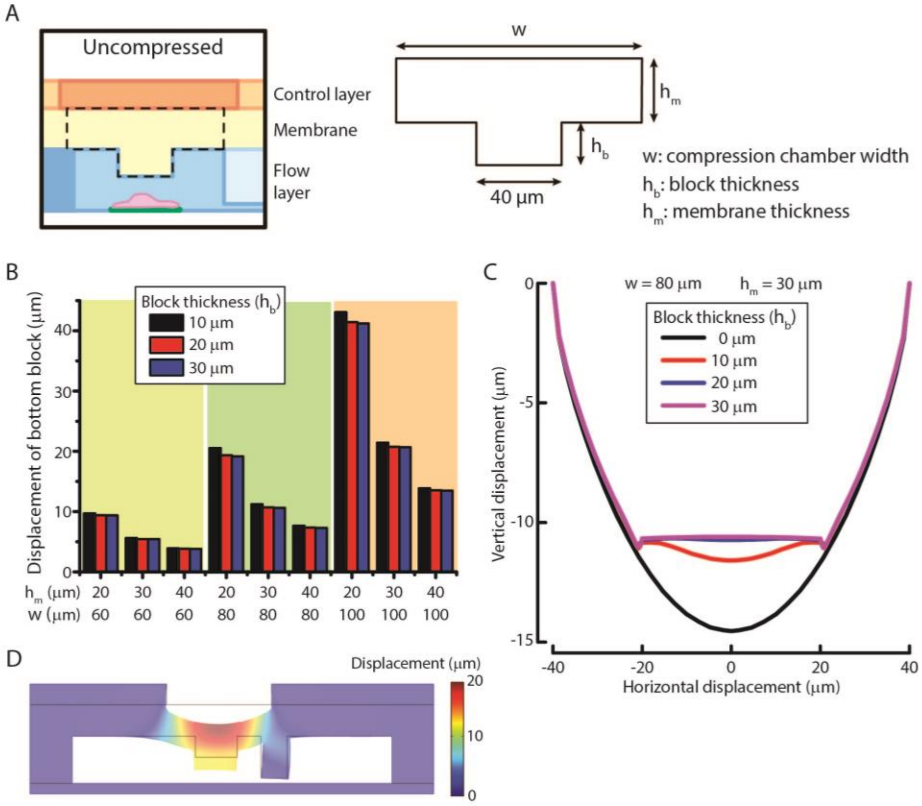

Figure 4-6: Simulation results for determining the geometric parameters of the device for cell compression

(A) Simplified membrane and block model for simulation. Three geometric parameters were defined as compression chamber width (w), block thickness (h_b) and membrane thickness (h_m). (B) Displacement of the simplified membrane and block model at different values of geometric parameters. (C) Vertical displacement of the membrane and block at different horizontal position across the compression chamber with different block thickness. (D) Displacement of the simulated result for the complete device model.

respectively. For the block thickness, we plot the displacement of the membrane and block with respect to the horizontal position across the compression chamber (**Figure 4-6C**). By changing the block thickness from 0 μm to 30 μm, we can readily see that the original concave deflection profile (black line, 0 μm) was minimized when the block thickness was increased to 20 μm (blue line) or higher. Therefore, the block thickness was set at 20 μm.

After the three parameters were set, I performed solid mechanics simulation of the complete device model with the parameters that were chosen using COMSOL. At a pressure of 10 psi, the membrane and block deflect around 10-15 psi as expected (**Figure 4-6D**), confirming that the results of the simplified membrane and block model were representative.

4.4.3 Flow streamlines and membrane deflections by pneumatic control

The microfluidic device has two sets of control valve for enhancing trapping and for the compression of cells respectively, similar to a previous design described in Chapter 3 [172]. Control valve set 1 features rectangular patterns across the main microfluidic channels. When Control valve set 1 is pressurized, the PDMS membrane above the main microfluidic channels deflects and the flow resistance in the main microfluidic channels is increased. This leads to a change in the flow profile to direct the flow to the compression chambers, thereby trapping cells. Control valve set 2 features rectangular patterns directly above each compression chamber. When Control valve set 2 is pressurized, the PDMS membrane above the compression chambers deflects and compresses the attached cells in the compression chambers.

From the simulation results in section 4.4.2, we obtained the following geometric parameters for the microfluidic device: block width of 40 μm, compression chamber width of 80 μm, block thickness of 20 μm, and membrane thickness of 30 μm. Therefore, we fabricated the microfluidic device according to the method described in section 4.3.2. To verify whether the simulation result is indeed the optimal design, we varied the compression chamber width and characterized the trapping efficiency and membrane deflection for compression.

To examine the trapping efficiency of the device when the Control valve set 1 was pressurized, we imaged the flow streamline inside the main microfluidic channel and the compression chamber. By flowing small fluorescent beads inside the microfluidic device, the beads will trace the streamlines of the fluid. When the beads are imaged at a high exposure time, the flow streamlines are captured. With increasing pressure applied the Control valve set 1, more fluid streamline entered the compression chamber (**Figure 4-7A**). This indicates an increase in trapping efficiency. Among the three different compression chamber widths of 60, 80, 100 μm, the device with 80 μm has the best trapping efficiency when the pressure in the Control valve set 1 was increased, and thus was used for the subsequent studies.

To examine the deflections of membrane with different compression chamber width as a function of different applied pressures, I labeled the microfluidic channel volume with rhodamine succinimidyl dye since the PDMS membrane cannot directly label easily. When Control valve set 2 was pressurized, the membrane deflected and displaced the fluid in the microfluidic channel so that I could indirectly visualize membrane deflection. The 3D and side view images of the compressed compression chamber were reconstructed and showed the increase in membrane deflection with increasing compression chamber widths (**Figure 4-7B, left**). Importantly, when the membrane deflected, the bottom of the block remained

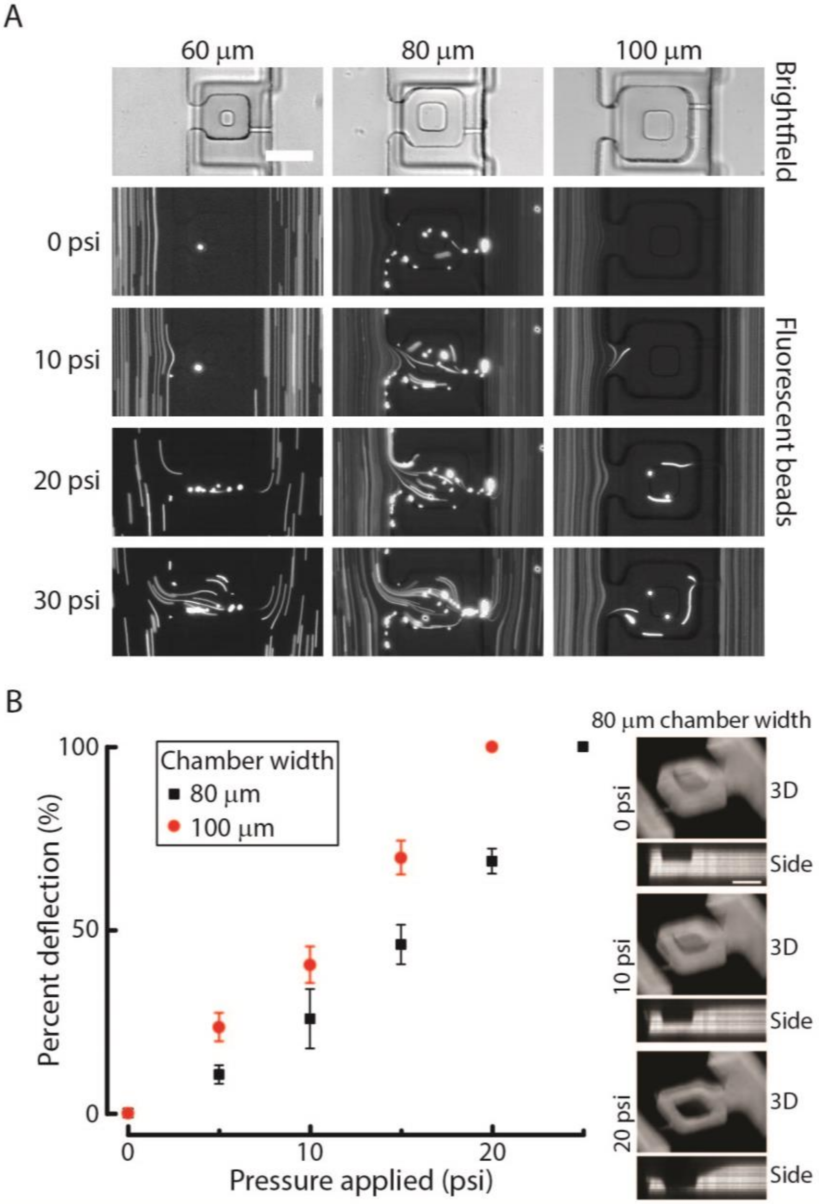

Figure 4-7: Flow streamlines and membrane deflection characterization in device with different compression chamber widths
(A) Brightfield images of the compression chamber and fluorescence images of the fluorescent beads of different widths were shown when the Control valve set 1 was pressurized (Scale bar = 60 μm). (B) (left) Membrane deflection of different compression chamber widths were characterized in different pressure applied. (Right) Reconstructed 3D and side view images of 80 μm chamber width at different Control valve set 2 pressures. Scale bar = 40 μm.

flat while the side membrane is concave (**Figure 4-7B, right**), demonstrating the block design was effective at providing a uniform compression.

4.4.4 Alignment of microcontact-printed fibronectin for the attachment and compression of cells

Microcontact printing of fibronectin inside the device controls the position and extent of cell spreading. The alignment of the microcontact printed fibronectin with the compression chamber is very important, as it will control the position of cell spreading underneath the block for uniform compression. Our customized alignment platform on an optical microscope does not support fluorescence imaging. Therefore, the microcontact printing of fibronectin was aligned with the compfression chamber of the device through a two-step alignment with a reference bottom alignment layer. The fabrication methods were described in section 4.3.2. After the alignment and the fabrication of the device, the fluorescent fibronectin was imaged and was verified to locate underneath the block inside the compression chamber, as desired (**Figure 4-8A**).

After the alignment of the microcontact printed fibronectin to the compression chamber, I verified if the fabrication steps and cell trapping methods did not affect the spreading of cell on the fibronectin island. The brightfield image of the compression chamber, fluorescence image of the fibronectin, fluorescence image of the nucleus and actin of the MCF-10A cell were imaged using a confocal microscope (**Figure 4-8B**). This demonstrated that the device still provides a desired environment for the spreading of the cells.

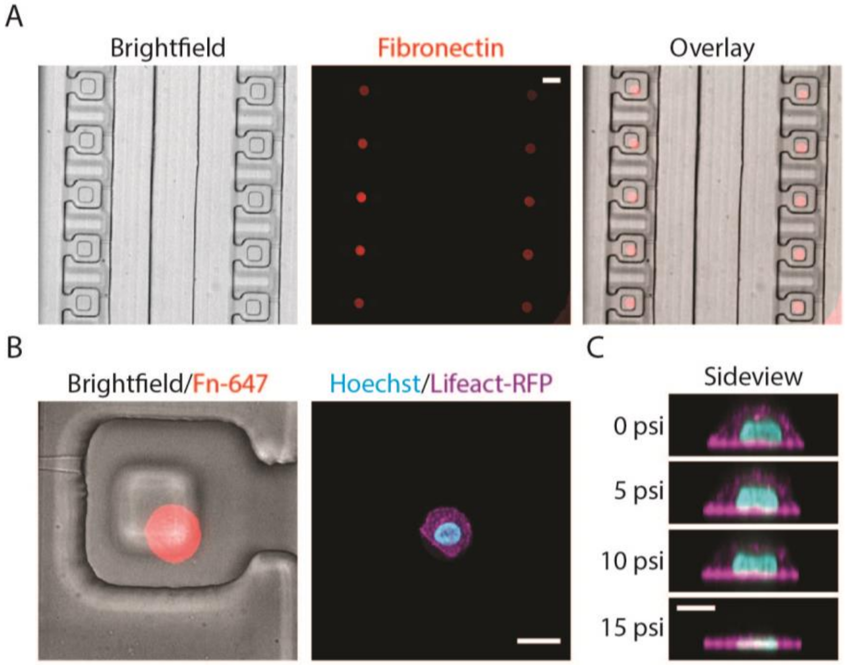

Figure 4-8: Alignment of microcontact-printed fibronectin for the attachment and compression of cells
(A) Brightfield and fluorescence images of the device and fibronectin respectively. Scale bar = 50 μm. (B) Zoom-in brightfield and fluorescence image of the device and fibronectin respectively (left). Fluorescence image of the MCF-10A cell, labeling the DNA (blue) and actin (red) (right). Scale bar = 20 μm. (C) Reconstructed side view image of the MCF-10A cell when the pressure of the Control valve set 2 was increased from 0 to 15 psi. Blue: DNA; Red: actin. Scale bar = 10 μm.

When the cells are spread on the fibronectin island, the cell can be compressed by the deflection of the PDMS membrane. As the pressure of the Control valve set 2 increases, the cell was compressed at 10 psi slightly and further compressed at 15 psi, as shown in the reconstructed side view images of the MCF-10A cell at different pressure applied (**Figure 4-8C**). This demonstrated the ability of the device to control different extent of compression on cells.

Apart from static compression, the new microfluidic device can apply cyclic compression to the cell by alternating the pressure between high and low values. The cell will experience repetitive compression and relaxation cycle. The pressure of the Control

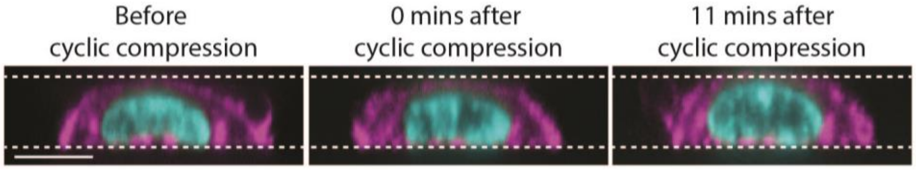

Figure 4-9: Images of cell before and after cyclic compression
Fluorescence side view images of the MCF-10A cell, labeling the DNA (blue) and actin (red), when the pressure of the Control valve set 2 was alternating between 10 and 15 psi at 0.5 Hz for 6 minutes. Scale bar = 10 μm.

valve set 2 was set to alternate between 10 and 15 psi at 0.5 Hz. After 6 minutes of cyclic compression, the cell was imaged and the reconstructed side view images show a slight reduction in height immediately after the compression and surprisingly a slight increase in height at 11 minutes after the cyclic compression compared to before cyclic compression (**Figure 4-9**), suggesting that the MCF-10A cell might respond to the cyclic compression and grow taller.

4.5 Conclusions

In this work, I have developed a new microfluidic device, which introduces a 20 μm thick PDMS block underneath the PDMS membrane to the microfluidic device described in Chapter 3 in order to apply uniform compression on cell. I also incorporated microcontact printed fibronectin islands that were aligned to be underneath the block in order to control the location of cell spreading. The design allowed the application of uniform compression on isolated single cells in a higher throughput manner. The device consists of a flow channel for trapping and spreading of cells and a control layer for trapping and compression. Another two PDMS substrates were used to print fibronectin on a PDMS-coated glass coverslip and facilitates the alignment of the device with the fibronectin patterns. By connecting a syringe pump to the flow channel and a computer controlled electro-regulator to the control layer, the device is able to apply static or cyclic compression on isolated, micropatterned single cells.

The development of the microfluidic device and the application of static or cyclic compressive loading to single cells have provided us the opportunity to study the mechanics of cells and cellular mechanotransduction pathways. Although the fabrication of the microfluidic device is still complicated, it has a potential to provide a higher throughput and an easier setup for compression of single cells. Collectively, the microfluidic device presented here enables research in mechanobiology of compression.

Chapter 5: Compression induces invadopodia-like actin protrusions

5.1 Introduction

5.1.1 Cancer invasion and metastasis

The activation of invasion and metastasis is one of the hallmarks in cancer [173]. It is characterized as the migration from the original tissue to invade adjacent tissues or distant organs. The behavior is mainly due to the aberrant regulation of cell migration in cancer cells, which is mainly driven by the protrusion of actin cytoskeleton [174]. One of the protrusive structures formed by cancer cells is invadopodia. Invadopodia is a dynamic ventral actin protrusion at the attachment and degradation sites on the extracellular matrix [175]. Different actin regulators, such as cortactin and N-WASP, and adaptor proteins, like Tks4 and Tks5, are the key proteins present in invadopodia. Invadopodia formation is regulated by Src signaling, which is negatively regulated by focal adhesion kinase (FAK) [176]. Invadopodia have been shown to degrade the extracellular matrix using a gelatin degradation assay [177]. Invadopodia are usually present in invasive cancer cells and play an important role in cancer invasion and metastasis. Thus, these dynamic and specialized actin cytoskeleton structures are one of the key features in invasive cancer cells.

5.1.2 Compression in tumor microenvironment

Uncontrolled cell proliferation is another hallmark in cancer [173]. Due to the uncontrolled division of cancer cells, solid pressure builds up in tumors and contributes to the increase in compressive forces on cancer cells [60] as well as to the cells in the surrounding normal tissue.

The effect of compressive forces on cancer cell behavior has been investigated before. Earlier work embedded cancer cells in agarose gels and established that microenvironmental mechanical stress inhibits tumor spheroid growth [178] and induces apoptosis via the mitochondrial pathway [166]. In another tumor spheroid study, it was found that the suppression of cell proliferation depends on the pressure-induced volume change and cell cycle regulation [179]. A recent study using a 2D cell monolayer strategy investigated the effect of compression on cancer cell invasion [168]. It was found that compression increases leader cell formation around the entire free-cell perimeter comparing to only in the corners of the square islands of a cell population. This work showed that mechanical compression can remodel the actin cytoskeleton and enhances cancer cell motility. The above *in vitro* studies concluded that despite the inhibition of proliferation and the induction of apoptosis, compression drives cancer cells toward an invasive phenotype. It is also supported by a recent study in an animal model where tumorigenic β-catenin pathway was induced at an applied 1200 Pa stress on normal and healthy colon tissue [180], supporting the idea that compressive stress potentially drives normal cells toward invasiveness.

5.1.3 Mechanosensing and mechanotransduction through actin cytoskeleton

Actin cytoskeleton plays an important role in mechanotransduction. Apart from providing mechanical strength for cells to withstand external forces such as compression and dynamically remodeling to provide different structures for cell motility, the actin cytoskeleton also plays a role in mechanosensing. A key feature of actin cytoskeleton network is that it is in a prestress state, as governed by the tensegrity model [181, 182]. This property of the actin cytoskeleton ensures quick, sensitive and coordinated mechanotransduction responses. The actin cytoskeleton is organized by actin-binding proteins and prestressed by the myosin motor proteins. The actin-binding proteins also serve as mechanosensors under forces. When actin filaments and actin network are under compressive forces, the force alters the conformation of the prestressed actin network and thus its affinity to the actin-binding proteins [183]. The actin network also transmits forces to other structures in the cell. These contribute to the transduction of mechanical signals into biochemical signals.

Actin cytoskeleton is very important in the mechanobiology of cells under compression. It is a sensitive mechanosensor that can sense the compressive force. Since it was shown that compression drives invasive phenotype, we hypothesized that compression also drives the formation of other protrusive structures in cells, such as invadopodia.

5.1.4 Compression on monolayer cell

Due to the tensegrity property of tissues, different cells experience different combinations of compressive, tensile and shear stresses when compression is applied to the tissue. To determine how compression is sensed and transduced inside the cells, we chose to apply compression to monolayer of cells in an uni-directional manner so that the effect of compression can be specifically studied.

The goal of this chapter is to further investigate the effect of compression on cells focusing on the remodeling of actin cytoskeleton. I applied compression to a monolayer of non-tumorigenic epithelial cells and mammary carcinoma cells and for the first time observed actin protrusions at the apical surface of the cells, in the direction of the compressive load. I further investigated whether these actin protrusions were invadopodia or not via immunofluorescence staining of actin regulator cortactin and adaptor protein Tks5, Western blot and drug inhibition of Src signaling and gelatin degradation assay. Overall, this study showed the formation of apical actin protrusions under high compression that are structurally but may not be functionally similar to invadopodia in normal cells.

5.2 Materials and methods

5.2.1 Preparation of cell lines

Two cell lines were used in this study, non-tumorigenic epithelial cell MCF-10A and mammary carcinoma cell MDA-MB-231. MCF-10A cells were cultured in growth media DMEM premixed 1:1 with Ham's F12 nutrient mixture with 5% horse serum, 1% pen-strep, 2.5 μg/ml amphotericin B(fungizone), 5 μg/ml gentamycin, 10 μg/ml insulin, 0.5 μg/ml hydrocortisone, 0.02 μg/ml epidermal growth factor, and 0.1 μg/ml cholera toxin. MDA-MB-231 cells were cultured in growth media RPMI1640 with 10% FBS, 1% pen-strep, 2.5

μg/ml amphotericin B (fungizone), and 5 μg/ml gentamycin. All cells were incubated at 37°C with 5% CO_2.

5 μg/ml Hoechst dye in media was used to label the nucleus. Stable cell lines expressing eGFP and Lifeact-RFP were generated via lentiviral transduction for labeling the cell volume and actin filaments respectively.

5.2.2 Preparation of agarose gel

1%, 2%, 4% and 8% agarose gels were made by dissolving different amounts of agarose powder (Invitrogen, UltraPure Agarose, 16500-100) in hot 1X PBS solution. The agarose gels were then autoclaved to sterilize the agarose solution. A sterilized PDMS mold with 24 mm holes was used for forming agarose gels with 24 mm diameter. 1 ml of hot agarose solution was added to the mold and allowed to cool down at room temperature. Once the agarose cooled down and hardened, the agarose gels were removed and immersed in corresponding culture media before use.

5.2.3 Compression of cells

The cells were compressed on a 27-mm glass bottom dish (Thermo Scientific, Nunc). First, 150,000 cells were seeded onto each glass bottom dish the day before compressing the cells. Then, a sterilized plastic cap with specified weight was used to apply a constant force to the agarose gel, which was placed on top of the cells. The entire compression setup was placed in the incubator for 30 minutes of compression. For control samples, the agarose gel was applied without the plastic cap. For most of the experiments, the weight was 27.7 g or 55.3 g, while the area of the agarose gel was 452 mm^2, which translates to a compressive stress of 600 Pa or 1200 Pa respectively.

5.2.4 Live-cell imaging

The glass bottom dish was mounted in a temperature-controlled stage on a spinning disk confocal microscope (Olympus IX73 with Yokogawa CSU-X1). The temperature was controlled so that the media was kept at 37^{o}C. The nucleus, cell volume and the actin structures were imaged before and 30 minutes after 600 Pa or 1200 Pa of compression. Z-stack images with 200 nm step size were captured and the side view images were reconstructed by using ImageJ.

5.2.5 Immunofluorescence

The cells were first compressed with 1200 Pa for 30 minutes. Before the removal of the weight, all the media was aspirated and 4% PFA in PBS was added for fixation. After 5 minutes of incubation, the weight was removed. The agarose gel was immediately incubated with fresh 4% PFA for another 5 minutes. The bottom surface of the agarose gel was washed, permeabilized, incubated with 3% BSA for 45 minutes, stained with primary antibodies and secondary antibodies, similar to a typical immunofluorescence labeling procedure. Primary antibodies used included anti-cortactin (Abcam, ab81208) and anti-Tks5 (Millipore, 09-403).

5.2.6 Gelatin assay

This protocol is adapted from Rachel et al 2015 [184]. The agarose gel was first coated with gelatin by placing 100 µl of gelatin solution on the 1% agarose gel for 10 minutes. The gelatin solution was a mixture of 0.1% fluorescein isothiocyante (FITC)-gelatin (Invitrogen) and 2% porcine gelatin in PBS in a volume ratio of 1:9. The agarose gel was then treated with 0.5% gluteraldehyde/PBS for 10 min, washed in PBS and incubated for 3 min in 5 mg/ml sodium borohydride ($NaBH_4$). Finally, the agarose gel was rinsed in PBS and incubated at 37° in 10% fetal bovine serum/DMEM/F12 for 30min before use. The cells were then compressed and imaged according to the immunofluorescence method above.

5.2.7 Preparation of cell lysate and Western blot

The cells were first compressed with 1200 Pa for 30 minutes. Before the removal of the weight, all the media was aspirated and CHAPS lysis buffer was added. CHAPS buffer has a composition of 40 mM HEPES at pH 7.5, 120 mM NaCl, 1 mM EDTA, 10 mM pyrophosphate, 10 mM glycerophospate, 50 mM NaF, 1.5 mM Na_3VO_4 and 0.3% CHAPS. After the removal of weight and incubation in CHAPS lysis buffer for 10 minutes on ice, the samples were then centrifuged at 16,100 g for 15 minutes at 4^oC to separate the supernatant and the pellet. The supernatant was mixed with 4x SDS sample buffer and was denatured for 5 minutes at 95^oC. Samples were run on SDS-PAGE and stained with SimplyBlue SafeStain (Thermo Fisher Scientific). Samples were transferred to a nitrocellulose membrane. The membrane was washed, blocked by 5% milk, and probed using anti-Src (Cell signaling, 2108S) and anti-p-Src (Cell signaling, 2101S) antibodies.

Three independent experiments were performed to confirm the obtained result. Intensity of gel bands was quantified using Image Studio Lite software.

5.3 Results and discussion

5.3.1 Apical actin protrusion in cells under normal compression

Under mechanical loading, the actin cytoskeleton deforms and remodels due to the binding and unbinding of different crosslinkers. Various signaling pathways may also become activated by the mechanical input, leading to the reinforcement of the actin cytoskeleton [71-73]. To study the remodeling of actin cytoskeleton under mechanical compression, I applied normal compression to a layer of cells seeded on a glass substrate with agarose gel and weight on top.

Surprisingly, after 30 minutes of compression at 1200 Pa, actin protrusions were observed at the apical surface of the MCF-10A cells (Figure 2-1**Figure 5-1**). The direction of actin protrusions is vertical, along the same direction of the compressive force and into the 1% agarose gel. This behavior is pressure dependent, as a lower compression pressure of 800 Pa did not result in the emergence of actin protrusions. The emergence of actin

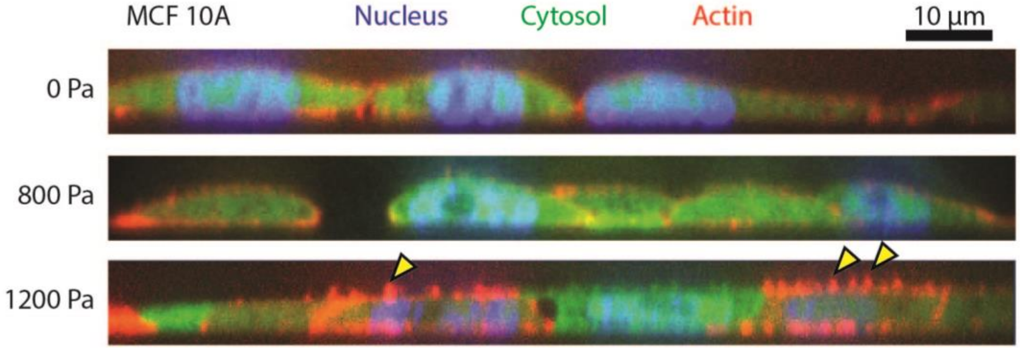

Figure 5-1: Emergence of actin protrusions on the apical surface of MCF-10A cells Side view fluorescence images of MCF-10A cell under 0, 800, 1200 Pa compressive stress; DNA (blue), cytosol (green) and actin (red). Scale bar = 10 μm.

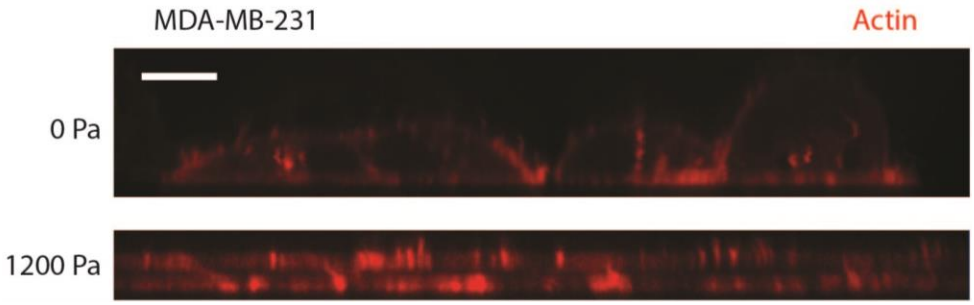

Figure 5-2: Actin protrusions appeared in apical surface of MDA-MB-231 cell
Side view fluorescence images of actin structure in MDA-MB-231 cell under 0 and 1200 Pa. Scale bar = 10 µm.

protrusions can also be found at the apical surface of mammary carcinoma cell, MDA-MB-231 (**Figure 5-2**). This is the first time that vertical actin protrusions were observed at the apical surface of cells under high normal compression.

5.3.2 Emergence of actin protrusions depends on agarose gel pore size

It was observed that the actin structures stayed inside the agarose gel when the weight and agarose gel were removed, suggesting that the actin protrusions entered into the agarose gel. To test whether the agarose gel pore size might influence the formation of actin protrusions at the cell-gel interface, we varied the concentration of the agarose in the gel effectively changing the pore size of the agarose gel. It was reported that the pore size of agarose gel reduces with concentration of agarose from 100-200 nm at 1% agarose to 50 nm at 3% agarose [185]. With the agarose concentration between 1% and 4%, actin protrusions were still observed at the apical surface of the MCF-10A cells (**Figure 5-3**). However, when the pore size of agarose further reduces (8% agarose), then actin protrusions were not observed.

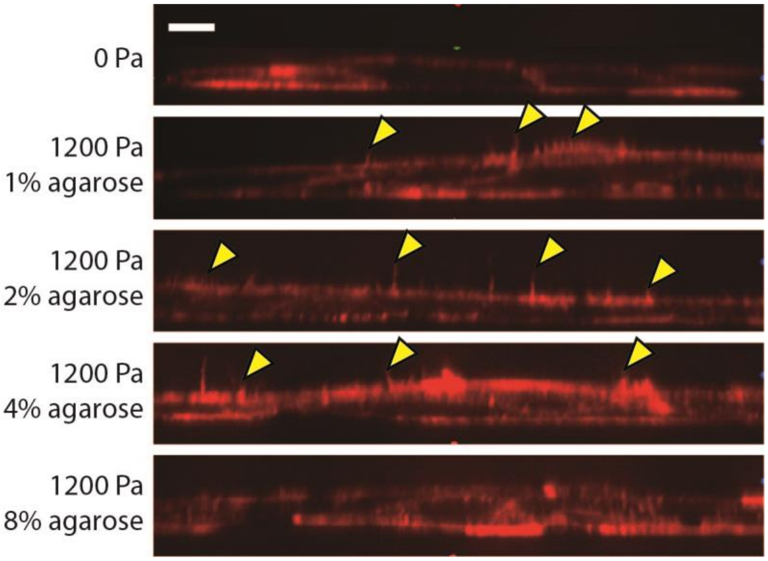

Figure 5-3: Actin protrusions at different agarose concentration
Side view fluorescence images of actin structure in MCF-10A cells with different concentrations of agarose (1% to 8%). Scale bar = 10 µm.

5.3.3 Molecular structure and functions

We suspected that the actin protrusions found at the apical surface of the cells have a similar structure as invadopodia [186] or mechanopodia [74]. Cortactin, an actin nucleation promoting factor, and Tks5, an invadopodia scaffold protein, are two common markers for invadopodia and are often found in invadopodia. To further examine the structure of the actin protrusions, we immunostained the agarose gel after the gel was peeled off and tested the presence of cortactin and Tks5 proteins at the actin structures trapped in the agarose gel.

We found that both cortactin and Tks5 colocalized with the actin structures inside the agarose gel when the cells were compressed for 30 minutes (**Figure 5-4A**). However, due to the short compression time (30 minutes), we did not find that the actin protrusions could degrade the extracellular matrix (**Figure 5-4B**). By comparision, invadopodia structures are found to degrade the extracellular matrix in 15 hours [177].

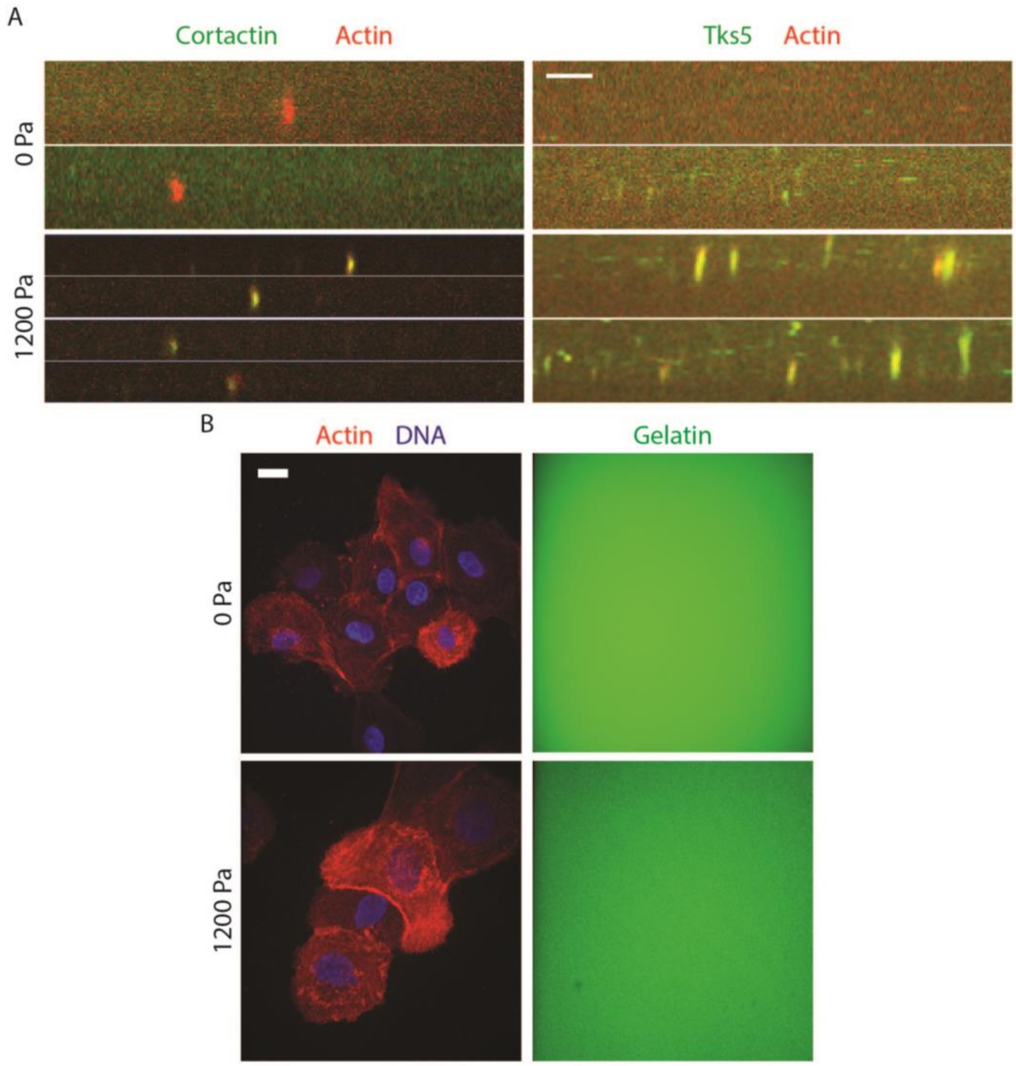

Figure 5-4: Molecular structure and functions of the actin protrusions
(A) Side view fluorescence images of the agarose gel, labeling cortactin and Tks5 (green) and actin (red). Scale bar = 10 μm. (B) Fluorescence images of the actin (red) and DNA (blue) of cell and gelatin (green) using a gelatin degradation assay. Scale bar = 10 μm.

5.3.4 Role of Src signaling in the formation of actin protrusions under compression

Src family kinases are critical in the formation of invadopodia. When Src kinase is activated by growth factors, they promote tyrosine phosphorylation of cortactin and Tks5, which are important steps during invadopodia formation [175, 187]. The phosphorylation of these proteins leads to the recruitment of N-WASP, along with Arp2/3 complex, activate actin polymerization and invadopodia elongation [188]. Since invadopodia formation depends on Src signaling, we tested if Src inhibition can abolish the formation of actin protrusions. We found that in the presence of 20 μM of PP2, a Src inhibitor, actin protrusion formation was abolished (**Figure 5-5A**). This means that Src signaling might be important for the emergence of actin protrusions under compression.

To further study whether mechanical compression leads to the activation of Src signaling, we performed Western blot analysis and directly looked at the protein level of

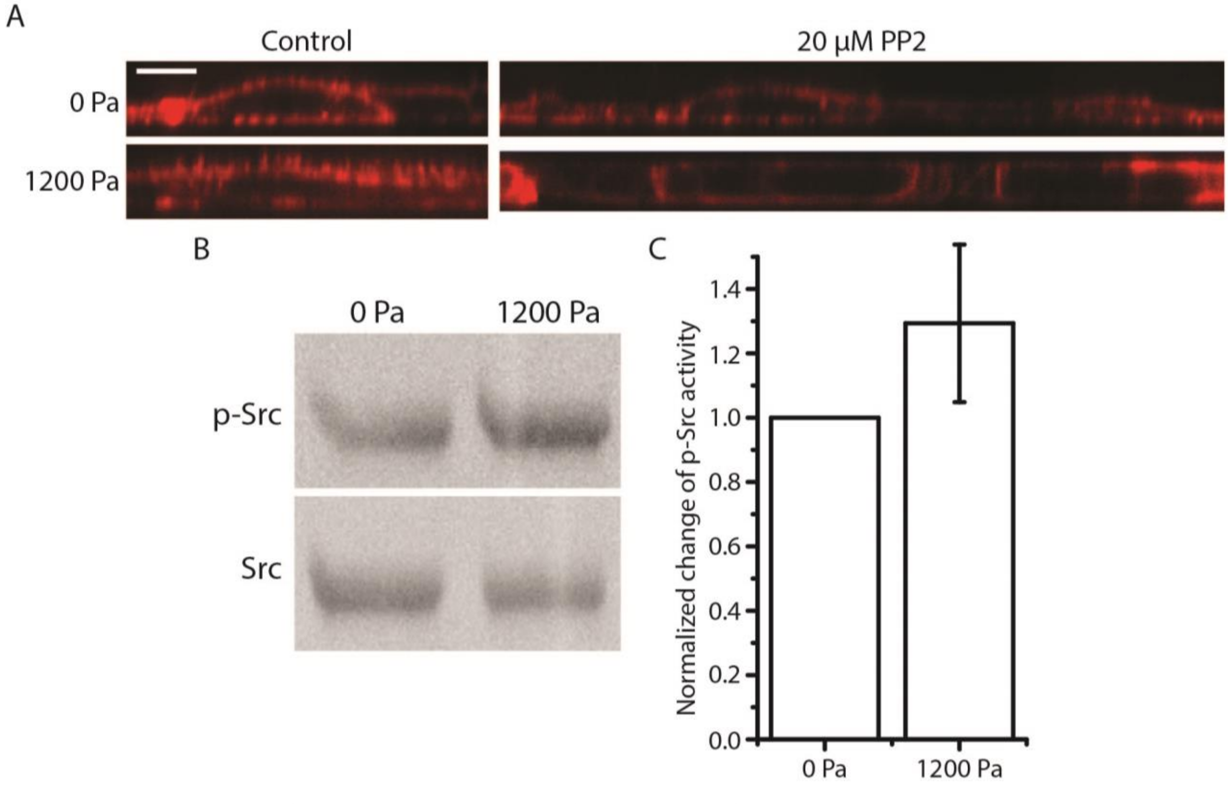

Figure 5-5: Role of Src signaling in the formation of actin protrusions under compression
(A) Side view fluorescence images of actin structure in MCF-10A cells, with and without PP2 an hour pre-treatment. Scale bar = 10 μm. (B) Western blot showing the phospho-Src and total Src for MCF-10A cells with and without compression. (C) Quantified and normalized change of phospho-Src activity for MCF-10A cells with and without compression. N = 3.

phosphorylated Src versus that of total Src. After applying compression for 30 minutes, the activity of phosphorylated Src showed a slight increase (**Figure 5-5B, C**). However, it was not a statistically significant change. Overall, from the drug inhibition and Western blot experiments, Src signaling may be one of the signaling pathways that is crucial for the formation of apical actin protrusions by compression. Further experiments are required to elucidate the molecular pathway by which compression induces apical actin protrusions.

5.4 Conclusions

In this work, I have discovered for the first time that actin protrusions form at the apical surface of epithelial cells following mechanical compression. The actin protrusions were found to form in mammary carcinoma cell as well and when 1% to 4% of agarose gel was used. The molecular structure of the actin protrusions was analyzed, and it was found that cortactin and Tks5 colocalized with the actin protrusions. By drug inhibition and Western blot analysis, Src signaling was shown to be important for the formation of actin protrusions and compression may lead to a local activation of Src.

Cells in our body experience compression, however the effect of compression on cells have not been well characterized. In this work, we applied compression to epithelial cells and studied in detail the remodeling of actin cytoskeleton. The emergence of actin protrusions at the apical surface of the cell is a new discovery and this study has provided more insight into the molecular pathway involved in the formation of actin protrusions by compression. Overall, this work opens up new directions in studying the mechanism of actin protrusion formation by compression.

Chapter 6: Conclusions and future work

6.1 Summary

Compression, tension and shear are three types of mechanical input that cells in our body experience. Modulation of compression and inability for cells to balance the compression can lead to various diseases, such as pressure ulcers, hypertension, embolism, acute angle-closure glaucoma, and cancer. However, the understanding of how cells sense and respond to compression is not fully understood.

To further advance our understanding of compression in mechanobiology, the development of new platforms and engineering tools play an important role in new scientific discoveries. In the development of mechanobiology, new scientific discovery often came with technological development that provides abilities to modulate mechanical inputs that cells experience and approaches to reduce the complex structures of living cells. In this dissertation, I endeavored to develop new experimental platform for studying mechanotransduction of compression in cells and further study the molecular responses of cells under compression using *in vitro* reconstitution and in single-cell and cell population systems. I first developed an *in vitro* reconstitution platform for constructing a simplified cell model that consists of bundled actin filaments or a cell-free expression system. I then developed a microfluidic device to mechanically trigger calcium influx in this simplified cell model. The microfluidic device was further optimized for applying compression force on single cells, so that the heterogeneous behaviors of cells can be studied. Finally, the mechanosensing and mechanotransduction of actin cytoskeleton were studied in a cell monolayer system to characterize the apical actin protrusions in cells that experience normal compression.

The cytoskeletal structures within the cell and between different cells are heterogeneous, making it very difficult to study the contribution of each cytoskeletal structure to the mechanical properties of cell. By developing a simplified but membrane-confined model of a cell using a bottom-up reconstitution approach, I constructed a simplified yet insightful cell-like structure. Using double emulsion templated lipid vesicle technique, biomolecules can be encapsulated inside lipid vesicles. This opens up opportunities of forming various cellular network inside lipid vesicle. For example, actin bundles network was formed inside lipid vesicles. By varying different actin-binding proteins, different networks can be formed that interact with the lipid membrane, creating a more cell-like mechanical structure for future cell mechanics study. To better model the cytosol of a living cell, a cell-free expression system was used. The cell-free expression system is a biomolecular *in vitro* transcription and translation system using translation machinery extracted from HeLa cells for producing proteins. The feasibility of encapsulating the mammalian cell-free expression system inside lipid vesicle was demonstrated. I found that the double emulsion stabilization surfactant PVA was precipitating actin structures inside the cell-free system, leading to a reduction of protein production and instability of lipid vesicles. Overall, I endeavored to develop a new platform for constructing simplified model of a cell that can be used for cell mechanics studies.

From working with bottom-up systems, I learned to appreciate the current challenges for constructing a simplified model of a cell using lipid bilayer vesicles. To reduce the complexity even more, I used an alternative model system, double emulsion droplets, to prototype a mechano-responsive simplified model of a cell. To mechanically activate the simplified model of a cell, I developed a microfluidic device for the application of mechanical inputs, such as aspiration and compression. The developed microfluidic device utilized microvalves and microfluidic feature for trapping, applying aspiration and compression separately to the double emulsion droplets through air pressure-controlled valves. The device was carefully characterized and trapping, aspiration and compression of double emulsion droplets were demonstrated. After the development of the microfluidic device, I successfully demonstrated the removal of the middle phase oil which led to transport of calcium ions into the double emulsion droplets during hypo-osmotic shock. This is the first time that one has demonstrated mechanical activation of cell-like double emulsion droplets. The newly developed microfluidic platform opens up opportunities of mechanically regulating gene expression in a more complex cell-free expression encapsulated artificial cell.

The newly developed microfluidic platform also allows mechanotransduction study in single cells to understand the heterogeneous responses of cells under compression. I modified the microfluidic device to provide a flat compressive surface by adding a rectangular block underneath the PDMS membrane. I also implemented microcontact-printed fibronectin island underneath the rectangular block in order to control the spreading location of cells inside each compression chamber. The improved microfluidic device was characterized experimentally and by using simulation. After the development of the microfluidic device, I successfully demonstrated the static and cyclic compression of single cells that were seeded on the fibronectin islands. Due to the ability to trap and compress multiple cells inside the microfluidic device, it opens up opportunity to study the heterogeneous mechanical properties and responses of single cells in a higher throughput manner. It also allows us to study different cellular responses under static and cyclic compression.

Apart from the development of membrane-confined bottom-up reconstitution platform for potential cell mechanics study and microfluidic platform for both static and cyclic compression, I have further investigated the molecular responses of actin cytoskeleton under compression to understand the roles of actin in sensing and responding to compressive loading. Actin protrusions were found to form at the apical surface of the cell under high compression. The actin protrusions extended vertically in the direction towards the compression force. Cortactin and Tks5 were present in the actin protrusions, while no extracellular matrix degradation was found during the timeframe of compression. Src signaling was identified to be crucial for the formation of actin protrusions by compression. The discovery of actin protrusions suggests a possible invadopodia-like response under high compression and opens up new directions for the study of compression in cells.

Overall, in this dissertation, I have developed two new emerging platforms for mechanobiology study and discovered actin cytoskeleton response under compression. The membrane-confined bottom-up reconstitution platform is a simplified yet insightful approach for constructing a simplified model of a cell that can be used for cell mechanics study. The microfluidic single-cell compression platform is a promising microtechnology for studying heterogeneous responses of single cells under static or cyclic compression and possibly other mechanotransduction studies. The newly discovered actin protrusion response of cells under compression opens up new directions to explore whether this has any relevance in high stress tissues found in several diseases such as cancer. Altogether, the techniques developed and findings reported in this dissertation help advance our understanding of mechanobiology of compressed cells.

6.2 Future work and perspectives

6.2.1 Cell mechanics study using membrane-confined bottom-up reconstitution

The membrane-confined bottom-up reconstitution platform allows the construction of different membrane-encapsulated cytoskeletal networks for cell mechanics study. In this dissertation, I did not apply mechanical forces to the constructed vesicle and measure its mechanical properties, such as elastic modulus, when different cytoskeletal networks were encapsulated. With the developed microfluidic device that allow the application of compression and aspiration of a cell-like model, we can measure the elasticity of the constructed vesicles. From this systematic investigation, we will be able to elucidate the role of confinement and network interaction with membrane on the elasticity of the cytoskeletal networks.

The combination of membrane-confined bottom-up reconstitution and microfluidic platforms opens up the opportunities to construct cell-like structures and measure the corresponding material properties. While this approach simplifies the complex structures inside a living cell, it retained the cell-like property of membrane confinement. Therefore, the mechanical properties measured for these constructed vesicles will recapitulate that of a living cell better.

6.2.2 Further purification of mammalian cell-free expression for aggregate-free encapsulation in lipid vesicle

In the dissertation, I investigated the possibility of encapsulating mammalian cell-free expression, an *in vitro* transcription and translation system as the cytosol of artificial cells, inside lipid vesicles using double emulsion templated method. It was found that actin structures inside the cell-free expression system were aggregated in the presence of surfactant PVA, leading to the reduction in protein production.

To resolve this issue, we can explore the possibility of further purifying the mammalian cell-free expression to remove actin. We can use antibody-coated beads that will bind to actin monomers as a way to pull down actin in the cell-free lysate. An actin-free mammalian cell-free expression system can potentially be compatible with the surfactant PVA and work as the cytosol for the artificial cell.

While we have shown that encapsulation of bacterial cell-free expression system did not have a precipitation issue compared to the mammalian cell-free expression system, mammalian cell-free expression system still poses an advantage to be the cytosol of the artificial cell. The mammalian system provides a versatile platform to express mammalian proteins, which may require post-translational modification. Artificial cells synthesized using mammalian cell-free expression system can be used to study the function of mechanosensitive mammalian membrane proteins, such as Piezo1. Overall, resolving the issue of precipitation of mammalian cell-free expression system with surfactant PVA will allow further studies and explorations of mechanosensitive artificial cells.

6.2.3 Mechanical activation of artificial cell by microfluidics

An alternative model system, double emulsion droplets, was used to prototype a mechano-responsive cell-like model in this dissertation, due to the challenges that we faced for constructing a membrane-confined artificial cell. After further development of the encapsulation of mammalian cell-free expression system inside lipid vesicles, we can construct artificial cells with mechanosensitive membrane proteins. The artificial cells can be programmed to sense mechanical stimulations and respond biochemically. For example, the artificial cell can sense compressive loading or an increase in membrane tension and translate this to a change in gene expression through the influx of secondary messengers into the artificial cell. To mechanically activate the artificial cell, a microfluidic device was developed in this dissertation to apply aspiration and compression to the artificial cells.

According to Feynman's idea of understanding: "That which I cannot create I do not understand" [189], the engineering of a mechanosensitive artificial cells becomes a testbed for us to further our understanding on the mechanosensing mechanism. With the help of the microfluidic device in applying mechanical loadings to the artificial cells, we will be able to test if we truly understand the mechanobiology of the simplified artificial cells that we engineered.

6.2.4 Study of cell viscoelasticity and plasticity after static and cyclic compression

The new microfluidic device was designed to apply compression on cells by increasing the air pressure applied to the Control valve set. This allows the cell to be compressed when the air pressure is high and relax when the air pressure is low. When the pressure alternates between high and low values, the cell will experience repetitive compression and relaxation cycles.

Most living cells show viscoelastic deformation under mechanical loading [190]. When the mechanical load was removed, the cell usually recovers partially to its original undeformed shape. The incomplete shape recovery is mainly due to the rupture of bond within the cytoskeleton, leading to the plasticity of cells [33, 191]. However, the cytoskeleton of the cell is anisotropic [192], organized by cytoskeletal filaments in different directions. Therefore, when a mechanical loading is applied, tensed regions will undergo plastic deformation, while compressed regions will not recover completely due to the inability to generate sufficient restoring forces after most of the elastic stresses have been evaded through buckling of the cytoskeletal fibers [33].

The way how cells withstand planar compression was not very clear. Different structures inside the cells may withstand the planar compressive deformation, such as actin cortex along the plasma membrane, vertical actin fibers connecting the apical and basal surfaces of the cells and the mechanical stiffness of the nucleus. While it is still unclear how living cells recover after mechanical compression was removed, the new microfluidic device developed in this dissertation can be used to apply uniform and well-controlled compression and study how epithelial cells recover after static and cyclic compressions.

6.2.5 Role of intercellular and traction forces in the activation of Src signaling under compression

In this dissertation, it was found that actin protrusions form on the apical surface when cells were compressed. The invadopodia-like molecular structure and Src signaling involved for the actin protrusions were studied. In analyzing the presence of actin protrusions in a cluster of cells, my preliminary data shows that actin protrusions appeared more often in the middle of a cluster comparing to the outside. Previous work showed that the intercellular and traction forces exerted by the cells depend on the number of cell-cell contacts that each cell experiences [26]. Therefore, a future direction could be to study the roles of intercellular and traction forces in the activation of Src signaling under compression. We can measure the intercellular and traction forces using traction force microscopy [25, 26, 193]. A Src biosensor can be used to visualize the spatial differences in Src activity within a cluster of cell [194], and determine if the spatial variation correlates with that of the actin protrusions and the intercellular or traction forces.

The intercellular and traction forces of the cell depend highly on the microenvironment. In this dissertation, we carried out the experiment on a 2D glass substrate. A future direction could be to characterize if actin protrusions form in 3D culturing context, that better recapitulates the microenvironment of a tumor. The investigation in this area will opens up questions of whether solid stress developed in tumor microenvironment is playing a role in the invasiveness of cancer cells as well as the tumorigenic transition of normal cells.

Overall, it is envisioned that the techniques developed and findings reported in this dissertation will lead to the advancement in mechanobiology and bring opportunities for future studies.

Bibliography

1. Hooke, R., *Micrographia: Or Some Physiological Descriptions of Minute Bodies Made by Magnifying Glasses, with Observations and Inquiries Thereupon*1665, Great Britain: Royal Society.

2. Sharp, L.W., *An Introduction To Cytology*1921: McGraw Hill Book Company Inc.

3. Newton, I., Sir, *Newton's Principia : the mathematical principles of natural philosophy*1846, New York: Daniel Adee.

4. Thompson, D.A.W., *On Growth and Form*1917: Cambridge University Press.

5. Orr, A.W., et al., *Mechanisms of Mechanotransduction.* Developmental Cell, 2006. **10**(1): p. 11-20.

6. Jaalouk, D.E. and J. Lammerding, *Mechanotransduction gone awry.* Nature Reviews Molecular Cell Biology, 2009. **10**: p. 63.

7. Engler, A.J., et al., *Matrix Elasticity Directs Stem Cell Lineage Specification.* Cell, 2006. **126**(4): p. 677-689.

8. Lu, P., V.M. Weaver, and Z. Werb, *The extracellular matrix: A dynamic niche in cancer progression.* J Cell Biol, 2012. **196**(4): p. 395-406.

9. Levental, K.R., et al., *Matrix Crosslinking Forces Tumor Progression by Enhancing Integrin Signaling.* Cell, 2009. **139**(5): p. 891-906.

10. Ingber, D.E., *Cellular mechanotransduction: putting all the pieces together again.* The FASEB Journal, 2006. **20**(7): p. 811-827.

11. Davies, P.F., *Hemodynamic shear stress and the endothelium in cardiovascular pathophysiology.* Nature Clinical Practice Cardiovascular Medicine, 2008. **6**: p. 16.

12. Rozario, T. and D.W. DeSimone, *The extracellular matrix in development and morphogenesis: A dynamic view.* Developmental Biology, 2010. **341**(1): p. 126-140.

13. Campàs, O., et al., *Quantifying cell-generated mechanical forces within living embryonic tissues.* Nature Methods, 2013. **11**: p. 183.

14. Ricca, B.L., G. Venugopalan, and D.A. Fletcher, *To pull or be pulled: parsing the multiple modes of mechanotransduction.* Current Opinion in Cell Biology, 2013. **25**(5): p. 558-564.

15. Heidemann, S.R. and D. Wirtz, *Towards a regional approach to cell mechanics.* Trends in Cell Biology, 2004. **14**(4): p. 160-166.

16. Liu, A.P. and D.A. Fletcher, *Biology under construction: in vitro reconstitution of cellular function.* Nature Reviews Molecular Cell Biology, 2009. **10**(9): p. 644-650.

17. Janmey, P.A. and C.A. McCulloch, *Cell Mechanics: Integrating Cell Responses to Mechanical Stimuli.* Annual Review of Biomedical Engineering, 2007. **9**(1): p. 1-34.

18. Pampaloni, F., E.G. Reynaud, and E.H.K. Stelzer, *The third dimension bridges the gap between cell culture and live tissue.* Nature Reviews Molecular Cell Biology, 2007. **8**: p. 839.

19. Van Vliet, K.J., G. Bao, and S. Suresh, *The biomechanics toolbox: experimental approaches for living cells and biomolecules.* Acta Materialia, 2003. **51**(19): p. 5881-5905.

20. Huxley, A.F. and R. Niedergerke, *Structural Changes in Muscle During Contraction: Interference Microscopy of Living Muscle Fibres.* Nature, 1954. **173**: p. 971.

21. Huxley, H. and J. Hanson, *Changes in the Cross-Striations of Muscle during Contraction and Stretch and their Structural Interpretation.* Nature, 1954. **173**: p. 973.

22. Curtis, A.S.G., *THE MECHANISM OF ADHESION OF CELLS TO GLASS.* A Study by Interference Reflection Microscopy, 1964. **20**(2): p. 199-215.

23. Huxley, H.E., *The Mechanism of Muscular Contraction.* Science, 1969. **164**(3886): p. 1356-1366.

24. Harris, A., P. Wild, and D. Stopak, *Silicone rubber substrata: a new wrinkle in the study of cell locomotion.* Science, 1980. **208**(4440): p. 177-179.

25. Oliver, T., K. Jacobson, and M. Dembo, *Traction forces in locomoting cells.* Cell Motility and the Cytoskeleton, 1995. **31**(3): p. 225-240.

26. Maruthamuthu, V., et al., *Cell-ECM traction force modulates endogenous tension at cell–cell contacts.* Proceedings of the National Academy of Sciences, 2011. **108**(12): p. 4708-4713.

27. Pelham, R.J. and Y.-l. Wang, *Cell locomotion and focal adhesions are regulated by substrate flexibility.* Proceedings of the National Academy of Sciences, 1997. **94**(25): p. 13661-13665.

28. Singhvi, R., et al., *Engineering cell shape and function.* Science, 1994. **264**(5159): p. 696-698.

29. Chen, C.S., et al., *Geometric Control of Cell Life and Death.* Science, 1997. **276**(5317): p. 1425-1428.

30. Tan, J.L., et al., *Cells lying on a bed of microneedles: An approach to isolate mechanical force.* Proceedings of the National Academy of Sciences, 2003. **100**(4): p. 1484-1489.

31. Fu, J., et al., *Mechanical regulation of cell function with geometrically modulated elastomeric substrates.* Nature Methods, 2010. **7**: p. 733.

32. Bausch, A.R., et al., *Local Measurements of Viscoelastic Parameters of Adherent Cell Surfaces by Magnetic Bead Microrheometry.* Biophysical Journal, 1998. **75**(4): p. 2038-2049.

33. Bonakdar, N., et al., *Mechanical plasticity of cells.* Nature Materials, 2016. **15**: p. 1090.

34. Binnig, G., C.F. Quate, and C. Gerber, *Atomic Force Microscope.* Phys Rev Lett, 1986. **56**(9): p. 930-933.

35. Hoh, J.H. and P.K. Hansma, *Atomic force microscopy for high-resolution imaging in cell biology.* Trends in Cell Biology, 1992. **2**(7): p. 208-213.

36. Rief, M., et al., *Reversible Unfolding of Individual Titin Immunoglobulin Domains by AFM.* Science, 1997. **276**(5315): p. 1109-1112.

37. Smith, M.L., et al., *Force-Induced Unfolding of Fibronectin in the Extracellular Matrix of Living Cells.* Plos Biology, 2007. **5**(10): p. e268.

38. Müller, D.J. and Y.F. Dufrêne, *Atomic force microscopy as a multifunctional molecular toolbox in nanobiotechnology.* Nature Nanotechnology, 2008. **3**: p. 261.

39. Novotny, L., R.X. Bian, and X.S. Xie, *Theory of Nanometric Optical Tweezers.* Phys Rev Lett, 1997. **79**(4): p. 645-648.

40. Moffitt, J.R., et al., *Recent Advances in Optical Tweezers.* Annual Review of Biochemistry, 2008. **77**(1): p. 205-228.

41. Choquet, D., D.P. Felsenfeld, and M.P. Sheetz, *Extracellular Matrix Rigidity Causes Strengthening of Integrin–Cytoskeleton Linkages.* Cell, 1997. **88**(1): p. 39-48.

42. Sackmann, E.K., A.L. Fulton, and D.J. Beebe, *The present and future role of microfluidics in biomedical research.* Nature, 2014. **507**: p. 181.

43. Polacheck, W.J., et al., *Microfluidic platforms for mechanobiology.* Lab on a Chip, 2013. **13**(12): p. 2252-2267.

44. Chau, L., M. Doran, and J. Cooper-White, *A novel multishear microdevice for studying cell mechanics.* Lab on a Chip, 2009. **9**(13): p. 1897-1902.

45. Moraes, C., et al., *Microfabricated arrays for high-throughput screening of cellular response to cyclic substrate deformation.* Lab on a Chip, 2010. **10**(2): p. 227-234.

46. Lee, L.M. and A.P. Liu, *A microfluidic pipette array for mechanophenotyping of cancer cells and mechanical gating of mechanosensitive channels.* Lab on a Chip, 2015. **15**(1): p. 264-273.

47. Liu, Allen P., *Biophysical Tools for Cellular and Subcellular Mechanical Actuation of Cell Signaling.* Biophysical Journal, 2016. **111**(6): p. 1112-1118.

48. Liu, A.P., O. Chaudhuri, and S.H. Parekh, *New advances in probing cell-extracellular matrix interactions.* Integrative Biology, 2017. **9**(5): p. 383-405.

49. Grodzinsky, A.J., et al., *Cartilage Tissue Remodeling in Response to Mechanical Forces.* Annual Review of Biomedical Engineering, 2000. **2**(1): p. 691-713.

50. Shyy, J.Y.-J. and S. Chien, *Role of Integrins in Endothelial Mechanosensing of Shear Stress.* Circulation Research, 2002. **91**(9): p. 769-775.

51. Gupta, V. and K.J. Grande-Allen, *Effects of static and cyclic loading in regulating extracellular matrix synthesis by cardiovascular cells.* Cardiovascular Research, 2006. **72**(3): p. 375-383.

52. Mammoto, T. and D.E. Ingber, *Mechanical control of tissue and organ development.* Development, 2010. **137**(9): p. 1407-1420.

53. Jain, R.K., J.D. Martin, and T. Stylianopoulos, *The Role of Mechanical Forces in Tumor Growth and Therapy.* Annual Review of Biomedical Engineering, 2014. **16**(1): p. 321-346.

54. Ehrlich, P.J. and L.E. Lanyon, *Mechanical Strain and Bone Cell Function: A Review.* Osteoporosis International, 2002. **13**(9): p. 688-700.

55. Gurkan, U.A. and O. Akkus, *The Mechanical Environment of Bone Marrow: A Review.* Annals of Biomedical Engineering, 2008. **36**(12): p. 1978-1991.

56. Daniel Rk Fau - Priest, D.L., D.C. Priest Dl Fau - Wheatley, and D.C. Wheatley, *Etiologic factors in pressure sores: an experimental model.* Arch. Phys. Med. Rehabil., 1981. **62**(10): p. 492-498.

57. Gawlitta, D., et al., *The Relative Contributions of Compression and Hypoxia to Development of Muscle Tissue Damage: An In Vitro Study.* Annals of Biomedical Engineering, 2007. **35**(2): p. 273-284.

58. Pengo , V., et al., *Incidence of Chronic Thromboembolic Pulmonary Hypertension after Pulmonary Embolism.* New England Journal of Medicine, 2004. **350**(22): p. 2257-2264.

59. Weinreb, R.N., T. Aung, and F.A. Medeiros, *The pathophysiology and treatment of glaucoma: A review.* JAMA, 2014. **311**(18): p. 1901-1911.

60. Stylianopoulos, T., et al., *Causes, consequences, and remedies for growth-induced solid stress in murine and human tumors.* Proceedings of the National Academy of Sciences, 2012. **109**(38): p. 15101-15108.

61. Stricker, J., T. Falzone, and M.L. Gardel, *Mechanics of the F-actin cytoskeleton.* Journal of Biomechanics, 2010. **43**(1): p. 9-14.

62. Lieleg, O. and A.R. Bausch, *Cross-Linker Unbinding and Self-Similarity in Bundled Cytoskeletal Networks.* Phys Rev Lett, 2007. **99**(15): p. 158105.

63. Lieleg, O., et al., *Transient Binding and Dissipation in Cross-Linked Actin Networks.* Phys Rev Lett, 2008. **101**(10): p. 108101.

64. Ward, S.M.V., et al., *Dynamic Viscoelasticity of Actin Cross-Linked with Wild-Type and Disease-Causing Mutant α-Actinin-4.* Biophysical Journal, 2008. **95**(10): p. 4915-4923.

65. Gardel, M.L., et al., *Elastic Behavior of Cross-Linked and Bundled Actin Networks.* Science, 2004. **304**(5675): p. 1301-1305.

66. Head, D.A., A.J. Levine, and F.C. MacKintosh, *Distinct regimes of elastic response and deformation modes of cross-linked cytoskeletal and semiflexible polymer networks.* Physical Review E, 2003. **68**(6): p. 061907.

67. Wilhelm, J. and E. Frey, *Elasticity of Stiff Polymer Networks.* Phys Rev Lett, 2003. **91**(10): p. 108103.

68. Fletcher, D.A. and P.L. Geissler, *Active Biological Materials.* Annual Review of Physical Chemistry, 2009. **60**(1): p. 469-486.

69. Wang, N., et al., *Cell prestress. I. Stiffness and prestress are closely associated in adherent contractile cells.* American Journal of Physiology-Cell Physiology, 2002. **282**(3): p. C606-C616.

70. Koenderink, G.H., et al., *An active biopolymer network controlled by molecular motors.* Proceedings of the National Academy of Sciences, 2009. **106**(36): p. 15192-15197.

71. Krishnan, R., et al., *Reinforcement versus Fluidization in Cytoskeletal Mechanoresponsiveness.* PLoS ONE, 2009. **4**(5): p. e5486.

72. Hoffman, L., et al., *Mechanical signals activate p38 MAPK pathway-dependent reinforcement of actin via mechanosensitive HspB1.* Molecular Biology of the Cell, 2017. **28**(20): p. 2661-2675.

73. Malek, A.M. and S. Izumo, *Mechanism of endothelial cell shape change and cytoskeletal remodeling in response to fluid shear stress.* Journal of Cell Science, 1996. **109**(4): p. 713-726.

74. Ho, F.C., et al., *Mechanoresponsive, omni-directional and local matrix-degrading actin protrusions in human mesenchymal stem cells microencapsulated in a 3D collagen matrix.* Biomaterials, 2015. **53**: p. 392-405.

75. Parekh, S.H., et al., *Loading history determines the velocity of actin-network growth.* Nature Cell Biology, 2005. **7**: p. 1219.

76. Bieling, P., et al., *Force Feedback Controls Motor Activity and Mechanical Properties of Self-Assembling Branched Actin Networks.* Cell, 2016. **164**(1): p. 115-127.

77. Wang, N., J. Butler, and D. Ingber, *Mechanotransduction across the cell surface and through the cytoskeleton.* Science, 1993. **260**(5111): p. 1124-1127.

78. Lulevich, V., et al., *Cell Mechanics Using Atomic Force Microscopy-Based Single-Cell Compression.* Langmuir, 2006. **22**(19): p. 8151-8155.

79. Weafer, P.P., et al., *Experimental and Computational Investigation of the Role of Stress Fiber Contractility in the Resistance of Osteoblasts to Compression.* Bulletin of Mathematical Biology, 2013. **75**(8): p. 1284-1303.

80. Whitesides, G.M., *The origins and the future of microfluidics.* Nature, 2006. **442**: p. 368.

81. Unger, M.A., et al., *Monolithic Microfabricated Valves and Pumps by Multilayer Soft Lithography.* Science, 2000. **288**(5463): p. 113-116.

82. Kim, Y.C., et al., *Microfluidic biomechanical device for compressive cell stimulation and lysis.* Sensors and Actuators B: Chemical, 2007. **128**(1): p. 108-116.

83. Hosmane, S., et al., *Valve-based microfluidic compression platform: single axon injury and regrowth.* Lab on a Chip, 2011. **11**(22): p. 3888-3895.

84. Si, F., et al., *Bacterial growth and form under mechanical compression.* Scientific Reports, 2015. **5**: p. 11367.

85. Bausch, A.R. and K. Kroy, *A bottom-up approach to cell mechanics.* Nature Physics, 2006. **2**: p. 231.

86. Fletcher, D.A. and R.D. Mullins, *Cell mechanics and the cytoskeleton.* Nature, 2010. **463**: p. 485.

87. Jensen, M.H., E.J. Morris, and D.A. Weitz, *Mechanics and dynamics of reconstituted cytoskeletal systems.* Biochimica et Biophysica Acta (BBA) - Molecular Cell Research, 2015. **1853**(11, Part B): p. 3038-3042.

88. MacKintosh, F.C., J. Käs, and P.A. Janmey, *Elasticity of Semiflexible Biopolymer Networks.* Phys Rev Lett, 1995. **75**(24): p. 4425-4428.

89. Storm, C., et al., *Nonlinear elasticity in biological gels.* Nature, 2005. **435**: p. 191.

90. Chaudhuri, O., S.H. Parekh, and D.A. Fletcher, *Reversible stress softening of actin networks.* Nature, 2007. **445**(7125): p. 295-298.

91. Carlson, E.D., et al., *Cell-free protein synthesis: applications come of age.* Biotechnol Adv, 2012. **30**(5): p. 1185-94.

92. Tawfik, D.S. and A.D. Griffiths, *Man-made cell-like compartments for molecular evolution.* Nat Biotechnol, 1998. **16**(7): p. 652-6.

93. Yu, W., et al., *Synthesis of functional protein in liposome.* Journal of Bioscience and Bioengineering, 2001. **92**(6): p. 590-593.

94. Caschera, F., et al., *Cell-free compartmentalized protein synthesis inside double emulsion templated liposomes with in vitro synthesized and assembled ribosomes.* Chemical Communications, 2016. **52**(31): p. 5467-5469.

95. Majumder, S., et al., *Cell-sized mechanosensitive and biosensing compartment programmed with DNA.* Chemical Communications, 2017. **53**(53): p. 7349-7352.

96. Mikami, S., et al., *A human cell-derived in vitro coupled transcription/translation system optimized for production of recombinant proteins.* Protein Expr Purif, 2008. **62**(2): p. 190-8.

97. Mikami, S., et al., *An efficient mammalian cell-free translation system supplemented with translation factors.* Protein Expr Purif, 2006. **46**(2): p. 348-57.

98. Utada, A.S., et al., *Monodisperse Double Emulsions Generated from a Microcapillary Device.* Science, 2005. **308**(5721): p. 537-541.

99. Kim, S.-H., et al., *Double-emulsion drops with ultra-thin shells for capsule templates.* Lab on a Chip, 2011. **11**(18): p. 3162-3166.

100. Ho, K.K., V.L. Murray, and A.P. Liu, *Engineering artificial cells by combining HeLa-based cell-free expression and ultrathin double emulsion template.* Methods Cell Biol, 2015. **128**: p. 303-18.

101. Utada, A.S., et al., *Dripping, Jetting, Drops, and Wetting: The Magic of Microfluidics.* MRS Bulletin, 2007. **32**(09): p. 702-708.

102. Utada, A.S., et al., *Dripping to Jetting Transitions in Coflowing Liquid Streams.* Physical Review Letters, 2007. **99**(9): p. 094502.

103. Arriaga, L.R., et al., *Ultrathin Shell Double Emulsion Templated Giant Unilamellar Lipid Vesicles with Controlled Microdomain Formation.* Small, 2014. **10**(5): p. 950-956.

104. Byfield, F.J., et al., *Cholesterol Depletion Increases Membrane Stiffness of Aortic Endothelial Cells.* Biophysical Journal, 2004. **87**(5): p. 3336-3343.

105. Jansen, S., et al., *Mechanism of Actin Filament Bundling by Fascin.* Journal of Biological Chemistry, 2011. **286**(34): p. 30087-30096.

106. Stachowiak, J.C., et al., *Inkjet formation of unilamellar lipid vesicles for cell-like encapsulation.* Lab on a Chip, 2009. **9**(14): p. 2003-2009.

107. Pontani, L.-L., et al., *Reconstitution of an Actin Cortex Inside a Liposome.* Biophysical Journal, 2009. **96**(1): p. 192-198.

108. Tsai, F.-C., B. Stuhrmann, and G.H. Koenderink, *Encapsulation of Active Cytoskeletal Protein Networks in Cell-Sized Liposomes.* Langmuir, 2011. **27**(16): p. 10061-10071.

109. Carvalho, K., et al., *Cell-sized liposomes reveal how actomyosin cortical tension drives shape change.* Proceedings of the National Academy of Sciences, 2013. **110**(41): p. 16456-16461.

110. Weiss, M., et al., *Sequential bottom-up assembly of mechanically stabilized synthetic cells by microfluidics.* Nature Materials, 2017. **17**: p. 89.

111. Ritz, S., et al., *Cell-free expression of a mammalian olfactory receptor and unidirectional insertion into small unilamellar vesicles (SUVs).* Biochimie, 2013. **95**(10): p. 1909-16.

112. Sachse, R., et al., *Membrane protein synthesis in cell-free systems: from bio-mimetic systems to bio-membranes.* FEBS Lett, 2014. **588**(17): p. 2774-81.

113. Abla, M., et al., *Micellar and biochemical properties of a propyl-ended fluorinated surfactant designed for membrane-protein study.* J Colloid Interface Sci, 2015. **445**: p. 127-36.

114. Durand, G., et al., *New amphiphiles to handle membrane proteins: "menage a trois" between chemistry, physical-chemistry and biochemistry*. Membrane Proteins Production for Structural Analysis, ed. I. Mus-Vetau. Vol. Chapter 8. 2014: Springer.

115. Park, K.H., et al., *Fluorinated and hemifluorinated surfactants as alternatives to detergents for membrane protein cell-free synthesis.* Biochem J, 2007. **403**(1): p. 183-7.

116. Rodnin, M.V., et al., *Interactions of Fluorinated Surfactants with Diphtheria Toxin T-Domain: Testing New Media for Studies of Membrane Proteins.* Biophysical Journal, 2008. **94**(11): p. 4348-4357.

117. Hayward, R.C., et al., *Dewetting instability during the formation of polymersomes from block-copolymer-stabilized double emulsions.* Langmuir, 2006. **22**(10): p. 4457-61.

118. Shum, H.C., et al., *Dewetting-induced membrane formation by adhesion of amphiphile-laden interfaces.* J Am Chem Soc, 2011. **133**(12): p. 4420-6.

119. Hutchison, C.A., et al., *Design and synthesis of a minimal bacterial genome.* Science, 2016. **351**(6280): p. 1414-U73.

120. Liu, A.P., et al., *Membrane-induced bundling of actin filaments.* Nature Physics, 2008. **4**(10): p. 789-793.

121. Zhang, Y., W.C. Ruder, and P.R. LeDuc, *Artificial cells: building bioinspired systems using small-scale biology.* Trends Biotechnol, 2008. **26**(1): p. 14-20.

122. Kurihara, K., et al., *A recursive vesicle-based model protocell with a primitive model cell cycle.* Nature Communications, 2015. **6**.

123. Lentini, R., et al., *Integrating artificial with natural cells to translate chemical messages that direct E-coli behaviour.* Nature Communications, 2014. **5**.

124. Matosevic, S. and B.M. Paegel, *Stepwise Synthesis of Giant Unilamellar Vesicles on a Microfluidic Assembly Line.* Journal of the American Chemical Society, 2011. **133**(9): p. 2798-2800.

125. Matosevic, S. and B.M. Paegel, *Layer-by-layer cell membrane assembly.* Nat Chem, 2013. **5**(11): p. 958-963.

126. Stachowiak, J.C., et al., *Unilamellar vesicle formation and encapsulation by microfluidic jetting.* Proceedings of the National Academy of Sciences of the United States of America, 2008. **105**(12): p. 4697-4702.

127. Coyne, C.W., et al., *Lipid Bilayer Vesicle Generation Using Microfluidic Jetting.* Jove-Journal of Visualized Experiments, 2014(84).

128. Teh, S.Y., et al., *Stable, biocompatible lipid vesicle generation by solvent extraction-based droplet microfluidics.* Biomicrofluidics, 2011. **5**(4).

129. Ho, K.K.Y., et al., *Protein aggregation with poly(vinyl) alcohol surfactant reduces double emulsion-encapsulated mammalian cell-free expression.* PLoS ONE, 2017. **12**(3): p. e0174689.

130. Abu Shah, E. and K. Keren, *Symmetry breaking in reconstituted actin cortices.* Elife, 2014. **3**.

131. Karzbrun, E., et al., *Programmable on-chip DNA compartments as artificial cells.* Science, 2014. **345**(6198): p. 829-832.

132. Nourian, Z., W. Roelofsen, and C. Danelon, *Triggered Gene Expression in Fed-Vesicle Microreactors with a Multifunctional Membrane.* Angewandte Chemie-International Edition, 2012. **51**(13): p. 3114-3118.

133. Hamada, S., et al., *Giant vesicles functionally expressing membrane receptors for an insect pheromone.* Chemical Communications, 2014. **50**(22): p. 2958-2961.

134. Kung, C., *A possible unifying principle for mechanosensation.* Nature, 2005. **436**(7051): p. 647-654.

135. Linshiz, G., et al., *PR-PR: cross-platform laboratory automation system.* Acs Synthetic Biology, 2014. **3**(8): p. 515-24.

136. Shih, S.C., et al., *A Versatile Microfluidic Device for Automating Synthetic Biology.* Acs Synthetic Biology, 2015. **4**(10): p. 1151-64.

137. Gach, P.C., et al., *A Droplet Microfluidic Platform for Automating Genetic Engineering.* Acs Synthetic Biology, 2016.

138. Luke, C.S., et al., *A Microfluidic Platform for Long-Term Monitoring of Algae in a Dynamic Environment.* Acs Synthetic Biology, 2016. **5**(1): p. 8-14.

139. Bennett, M.R., et al., *Metabolic gene regulation in a dynamically changing environment.* Nature, 2008. **454**(7208): p. 1119-1122.

140. Stricker, J., et al., *A fast, robust and tunable synthetic gene oscillator.* Nature, 2008. **456**(7221): p. 516-U39.

141. Prindle, A., et al., *A sensing array of radically coupled genetic 'biopixels'.* Nature, 2012. **481**(7379): p. 39-44.

142. Mondragon-Palomino, O., et al., *Entrainment of a Population of Synthetic Genetic Oscillators.* Science, 2011. **333**(6047): p. 1315-1319.

143. Tayar, A.M., et al., *Propagating gene expression fronts in a one-dimensional coupled system of artificial cells.* Nature Physics, 2015. **11**(12): p. 1037-+.

144. Sukharev, S., et al., *The gating mechanism of the large mechanosensitive channel MscL.* Nature, 2001. **409**(6821): p. 720-724.

145. Lewis, A.H. and J. Grandl, *Mechanical sensitivity of Piezo1 ion channels can be tuned by cellular membrane tension.* Elife, 2015. **4**.

146. Magdassi, S. and N. Garti, *Release of electrolytes in multiple emulsions: coalescence and breakdown or diffusion through oil phase?* Colloids and Surfaces, 1984. **12**: p. 367-373.

147. Kita, Y., S. Matsumoto, and D. Yonezawa, *Permeation of Water through the Oil Layer in W/O/W-Type Multiple-Phase Emulsions.* NIPPON KAGAKU KAISHI, 1978. **1978**(1): p. 11-14.

148. Holtze, C., et al., *Biocompatible surfactants for water-in-fluorocarbon emulsions.* Lab on a Chip, 2008. **8**(10): p. 1632-1639.

149. Xia, Y. and G.M. Whitesides, *SOFT LITHOGRAPHY.* Annual Review of Materials Science, 1998. **28**(1): p. 153-184.

150. *SU-8 2000 Permanent Epoxy Resists :: MicroChem*. Available from: http://www.microchem.com/Prod-SU82000.htm.

151. Nakano, M., *Places of emulsions in drug delivery.* Advanced Drug Delivery Reviews, 2000. **45**(1): p. 1-4.

152. Colombo, A., et al., *A method to develop mock arteries suitable for cell seeding and in-vitro cell culture experiments.* Journal of the Mechanical Behavior of Biomedical Materials, 2010. **3**(6): p. 470-477.

153. Sajeesh, P., et al., *A microfluidic device with focusing and spacing control for resistance-based sorting of droplets and cells.* Lab on a Chip, 2015. **15**(18): p. 3738-3748.

154. Ma, S., W.T.S. Huck, and S. Balabani, *Deformation of double emulsions under conditions of flow cytometry hydrodynamic focusing.* Lab on a Chip, 2015. **15**(22): p. 4291-4301.

155. Chen, Y., X. Liu, and Y. Zhao, *Deformation dynamics of double emulsion droplet under shear.* Applied Physics Letters, 2015. **106**(14): p. 141601.

156. Cheng, J., et al., *Transport of ions through the oil phase of W1/O/W2 double emulsions.* Journal of Colloid and Interface Science, 2007. **305**(1): p. 175-182.

157. Wen, L. and K.D. Papadopoulos, *Visualization of water transport in W1/O/W2 emulsions.* Colloids and Surfaces A: Physicochemical and Engineering Aspects, 2000. **174**(1–2): p. 159-167.

158. Wen, L. and K.D. Papadopoulos, *Effects of Osmotic Pressure on Water Transport in W1/O/W2 Emulsions.* Journal of Colloid and Interface Science, 2001. **235**(2): p. 398-404.

159. Zhang, Y., et al., *A programmable microenvironment for cellular studies via microfluidics-generated double emulsions.* Biomaterials, 2013. **34**(19): p. 4564-4572.

160. Chan, H.F., et al., *Rapid formation of multicellular spheroids in double-emulsion droplets with controllable microenvironment.* Scientific Reports, 2013. **3**: p. 3462.

161. Bustamante, C., et al., *Mechanical processes in biochemistry.* Annual Review of Biochemistry, 2004. **73**: p. 705-748.

162. Kurth, F., et al., *A new mechanobiological era: microfluidic pathways to apply and sense forces at the cellular level.* Current Opinion in Chemical Biology, 2012. **16**(3–4): p. 400-408.

163. Gray, B.L., et al., *Microchannel Platform for the Study of Endothelial Cell Shape and Function.* Biomedical Microdevices, 2002. **4**(1): p. 9-16.

164. Song, J.W., et al., *Computer-Controlled Microcirculatory Support System for Endothelial Cell Culture and Shearing.* Analytical Chemistry, 2005. **77**(13): p. 3993-3999.

165. Svennersten, K., et al., *Mechanical stimulation of epithelial cells using polypyrrole microactuators.* Lab on a Chip, 2011. **11**(19): p. 3287-3293.

166. Cheng, G., et al., *Micro-Environmental Mechanical Stress Controls Tumor Spheroid Size and Morphology by Suppressing Proliferation and Inducing Apoptosis in Cancer Cells.* PLoS ONE, 2009. **4**(2): p. e4632.

167. Dumont, S. and T.J. Mitchison, *Compression Regulates Mitotic Spindle Length by a Mechanochemical Switch at the Poles.* Current Biology, 2009. **19**(13): p. 1086-1095.

168. Tse, J.M., et al., *Mechanical compression drives cancer cells toward invasive phenotype.* Proceedings of the National Academy of Sciences, 2012. **109**(3): p. 911-916.

169. Lulevich, V., et al., *Single-cell mechanics provides a sensitive and quantitative means for probing amyloid-β peptide and neuronal cell interactions.* Proceedings of the National Academy of Sciences, 2010. **107**(31): p. 13872-13877.

170. Lulevich, V., et al., *Single cell mechanics of keratinocyte cells.* Ultramicroscopy, 2010. **110**(12): p. 1435-1442.

171. Thorsen, T., S.J. Maerkl, and S.R. Quake, *Microfluidic Large-Scale Integration.* Science, 2002. **298**(5593): p. 580-584.

172. Ho, K.K.Y., L.M. Lee, and A.P. Liu, *Mechanically activated artificial cell by using microfluidics.* Scientific Reports, 2016. **6**: p. 32912.

173. Hanahan, D. and Robert A. Weinberg, *Hallmarks of Cancer: The Next Generation.* Cell. **144**(5): p. 646-674.

174. Yamaguchi, H. and J. Condeelis, *Regulation of the actin cytoskeleton in cancer cell migration and invasion.* Biochimica et Biophysica Acta (BBA) - Molecular Cell Research, 2007. **1773**(5): p. 642-652.

175. Murphy, D.A. and S.A. Courtneidge, *The 'ins' and 'outs' of podosomes and invadopodia: characteristics, formation and function.* Nature Reviews Molecular Cell Biology, 2011. **12**: p. 413.

176. Chan, K.T., C.L. Cortesio, and A. Huttenlocher, *FAK alters invadopodia and focal adhesion composition and dynamics to regulate breast cancer invasion.* J Cell Biol, 2009. **185**(2): p. 357-370.

177. Baldassarre, M., et al., *Dynamin Participates in Focal Extracellular Matrix Degradation by Invasive Cells.* Molecular Biology of the Cell, 2003. **14**(3): p. 1074-1084.

178. Helmlinger, G., et al., *Solid stress inhibits the growth of multicellular tumor spheroids.* Nature Biotechnology, 1997. **15**: p. 778.

179. Delarue, M., et al., *Compressive Stress Inhibits Proliferation in Tumor Spheroids through a Volume Limitation.* Biophysical Journal, 2014. **107**(8): p. 1821-1828.

180. Fernandez-Sanchez, M.E., et al., *Mechanical induction of the tumorigenic [bgr]-catenin pathway by tumour growth pressure.* Nature, 2015. **523**(7558): p. 92-95.

181. Ingber, D.E., *Tensegrity-based mechanosensing from macro to micro.* Progress in Biophysics and Molecular Biology, 2008. **97**(2): p. 163-179.

182. Donald, E.I., W. Ning, and S. Dimitrije, *Tensegrity, cellular biophysics, and the mechanics of living systems.* Reports on Progress in Physics, 2014. **77**(4): p. 046603.

183. Romet-Lemonne, G. and A. Jégou, *Mechanotransduction down to individual actin filaments.* European Journal of Cell Biology, 2013. **92**(10): p. 333-338.

184. Jerrell, R.J. and A. Parekh, *Polyacrylamide Gels for Invadopodia and Traction Force Assays on Cancer Cells.* 2015(95): p. e52343.

185. Janaky, N., X. Jun-Ying, and L. Xiang-Yang, *Determination of agarose gel pore size: Absorbance measurements vis a vis other techniques.* Journal of Physics: Conference Series, 2006. **28**(1): p. 83.

186. Oser, M., et al., *Cortactin regulates cofilin and N-WASp activities to control the stages of invadopodium assembly and maturation.* J Cell Biol, 2009. **186**(4): p. 571-587.

187. Burger, K.L., et al., *Src-dependent Tks5 phosphorylation regulates invadopodia-associated invasion in prostate cancer cells.* The Prostate, 2014. **74**(2): p. 134-148.

188. Jacob, A. and R. Prekeris, *The regulation of MMP targeting to invadopodia during cancer metastasis.* Frontiers in Cell and Developmental Biology, 2015. **3**(4).

189. Hawking, S.W., *The Universe in a Nutshell.* 2001, New York: Bantam.

190. Fabry, B., et al., *Scaling the Microrheology of Living Cells.* Phys Rev Lett, 2001. **87**(14): p. 148102.

191. Bausch, A.R., et al., *Rapid Stiffening of Integrin Receptor-Actin Linkages in Endothelial Cells Stimulated with Thrombin: A Magnetic Bead Microrheology Study.* Biophysical Journal, 2001. **80**(6): p. 2649-2657.

192. Hu, S., et al., *Intracellular stress tomography reveals stress focusing and structural anisotropy in cytoskeleton of living cells.* American Journal of Physiology-Cell Physiology, 2003. **285**(5): p. C1082-C1090.

193. Sancho, A., et al., *A new strategy to measure intercellular adhesion forces in mature cell-cell contacts.* Scientific Reports, 2017. **7**: p. 46152.

194. Ouyang, M., et al., *Determination of hierarchical relationship of Src and Rac at subcellular locations with FRET biosensors.* Proceedings of the National Academy of Sciences, 2008. **105**(38): p. 14353-14358.